2019

New Generation Inorganic Nanoparticles for Sunscreen UV Filtration

Marcela L. Chaki Borrás
University of Wollongong

UNIVERSITY
OF WOLLONGONG
AUSTRALIA

New Generation Inorganic Nanoparticles for Sunscreen UV Filtration

Marcela L. Chaki Borrás

Supervisors: Dr. Konstantin Konstantinov,
& Dr. Vitor Sencadas

Co-supervisor: Dr. Shahnaz Bakand

This thesis is presented as part of the requirements for the conferral of the degree:

Master of Research
(Advanced Materials)

University of Wollongong
School of Chemistry

November 2019

Certification

I, *Marcela Laura Chaki Borrás*, declare that this thesis submitted in fulfilment of the requirements for the conferral of the degree Master of Research, from the University of Wollongong, is wholly my own wok unless otherwise referenced or acknowledged. This document has not been submitted for qualifications at any other academic institution.

_____

Marcela Laura Chaki Borrás

8th November 2019

Abstract

Australia has one of the highest melanoma rates worldwide owing to extremely high ultraviolet (UV) levels due to ozone depletion. Thus, effective protection against UV radiation is a necessity. Sunscreens contain titanium dioxide (TiO_2) and zinc oxide (ZnO) nanoparticles as inorganic UV filters to protect the skin from damaging UV light by means of scattering, absorption and reflection. However, these nanomaterials have the potential to penetrate the skin and impart cytotoxicity on viable cells caused by free radicals generated as a result of their photocatalytic activity. As such, health concerns have been raised regarding their use in cosmetic products. Toxicological reviews of these particles have reported inconclusive results due to the differences in test protocols and lack of real-life conditions, including the absence of UV irradiation. Regardless of these discrepancies, the photocatalytic activity of these materials is a key property that should be reduced to avoid potential detrimental effects, not only to humans but also to the environment. Hence, the aim of this research was to develop a new generation nanoparticle system for sunscreen application by reducing the photocatalytic activity of currently available commercial TiO_2 nanoparticles for UV filtration in sunscreen products. Thus, enhancing its biocompatibility whist also maintaining its UV absorption properties. A reported free radical scavenger, yttrium oxide (Y_2O_3), was deposited onto TiO_2 through a hydrothermal method forming a coating layer. The characterisation of the synthesised nanomaterial comprised several standard analytical techniques, such as UV-visible spectroscopy, X-ray diffraction, scanning and transmission electron microscopy, electron dispersive spectroscopy and Brunauer-Emmett-Teller analysis to assess properties such as UV absorption, photocatalytic activity, morphology, composition, particle size and surface area. Furthermore, *in vitro* biocompatibility assays were performed on the human skin HaCaT cell line in the absence and presence of simulated solar radiation. Synthesised Y_2O_3 coated TiO_2 nanoparticles showed an increase in UVB and short UVA absorption, in addition to reduced photocatalytic activity, compared to pristine TiO_2 nanoparticles. Additionally, higher cell viability was observed after exposure to the synthesised particles, compared to the commercial TiO_2 both in the

absence and presence of simulated solar radiation. Thus, highlighting the potential of these coated particles for UV filtration applications.

Keywords: Sunscreen products, UV radiation, photocatalytic activity, TiO_2, ZnO, Y_2O_3, antioxidant, HaCaT cells, biocompatibility, reactive oxygen species (ROS).

Acknowledgements

First and foremost, I would like to acknowledge my primary supervisors, Dr. Konstantin Konstantinov and Dr. Vitor Sencadas, without your support I would have not had the chance to do this research nor work with this magnificent research group. Furthermore, your supervision and guidance over the course of this research has been of no measure. You have taught me to stand for what I think with more conviction, this has been an experience I will never forget, thank you. Next, I would like to express my deepest gratitude to Dr. Shahnaz Bakand, I could not have had a better co-supervisor. You have always provided prompt and valuable feedback. You have helped me carry out this project with your guidance and support, thank you. I would also like to thank Dr. Ronald Sluyter for providing his expertise whenever needed and encouraging me to contact him to express my doubts. I would too like to thank Alex Morlando for providing his help whenever I needed it. It has been great working beside someone as kind, knowledgeable and thorough as you.

Thank you to the staff at the Illawarra Health and Medical Research Institute (IHMRI) and Australian Institute for Innovative Materials (AIIM) for training me on the required equipment, without which I would not have been able to do this research. I would also like to thank Tony Romero, Dr. David Mitchell and Dr. Gilberto Casillas García from the Electron Microscopy Centre at AIIM for their assistance obtaining the electron microscope images. I would like to acknowledge Peter Sara from the workshop at the UOW campus whom without this project would not have moved to a next stage.

Lastly, I would like to thank the people closest to my heart, my family and partner. Thank you for believing in me even when I didn't myself. Thank you for dealing with my insecurities and frustrations. Thank you for the emotional and moral support, and love. I can't thank you enough, words can't express what you mean to me, I would certainly not be the person I am today without you. David, thank you for your continuous support and patience, I know sometimes I can be difficult to deal with, but you have always been there for me. I love you.

Table of Contents

List of Tables

List of Figures

List of Abbreviations

AIIM	Australian Institute for Innovative Materials	**EDS**	Energy dispersive X-ray spectroscopy
ANOVA	Analysis of variance	**EDTA**	Ethylenediaminetetraacetic acid
AVOB	Avobenzone	***Eg***	Optical band gap energy
BCC	Basal cell carcinoma	**ESR**	Electron spin resonance
BET	Brunauer-Emmet-Teller	**FBS**	Fetal bovine serum
BMDBM	Butyl methoxydibenzoylmethane	**HaCaT**	Aneuploid immortal human skin keratinocyte cell line
CB	Conduction band	**HOMO**	Highest occupied molecular orbital
CV	Crystal violet	**IC**	Inhibitory concentration
DI	De-ionized	**IHMRI**	Illawarra Health and Medical Research Institute
DLS	Dynamic light scattering	**LUMO**	Lowest unoccupied molecular orbital
DMEM/F12	Dulbecco's Modified Eagle Medium: Ham's F-12 nutrient mixture	**MED**	Minimal erythema dose
DNA	Deoxyribonucleic acid	**MTS**	3-(4,5-dimethylthiazol-2-yl)-5-(3-carboxymethoxyphenyl)-2-(4-sulfophenyl)-2H-tetrazolium salt
DPBS	Dulbecco's phosphate buffered saline	**NADH**	Nicotinamide adenine dinucleotide
DSSCs	Dye-sensitised solar cells	**NADPH**	Nicotinamide adenine dinucleotide phosphate

NOAEC	No observed adverse effect concentration
NP(s)	Nanoparticle(s)
OMC	Ethylhexyl *p*-methoxycinnamate
PABA	Para-aminobenzoic acid
PMAA	Poly methyl acrylic acid
ROS	Reactive oxygen species
SCC	Squamous cell carcinoma
SCCS	Scientific committee for consumer safety
SEM	Scanning electron microscope
STEM	Scanning transmission electron microscope
TBARS	Thiobarbituric acid reactive substances
TEM	Transmission electron microscope
TLC	Total lethal concentration
UV	Ultraviolet
UVA	Ultraviolet A
UVB	Ultraviolet B
UVC	Ultraviolet C
UV-vis	Ultraviolet-visible
VB	Valence band
XRD	X-ray diffraction

Chapter 1

Introduction

1.1 General background and motivation

1.1.1 Nanotechnology within the cosmetic industry

Nanotechnology is a multidisciplinary science defined as the manipulation of matter with at least one dimension between 1 and 100 nm [1]. At the nanoscale, materials possess enhanced and unique physiochemical properties, including magnetic, optical, thermal and catalytic properties ascribed to their size reduction [2, 3]. This is thought to be impart due to the significantly increased surface area and greater percentage of surface atoms, which make them attractive for a vast array of applications, from medicine to electronics and from the food to the cosmetic industry [2, 3]. The enhanced optical properties of nanomaterials are of extreme value for the cosmetic industry as these offer improved transparency, reflectivity and colour in the final products [3]. Hence, as of 2009 the number of registered cosmetic products containing nanoparticles within their formulation had almost increased 1900% in four years, from 54 to 1015 between 2005 and 2009, respectively [3]. The most frequently found nanomaterials in cosmetic products include silver, carbon, gold, silicon, titanium and zinc based materials [3].

1.1.2 Ultraviolet radiation, skin cancer and Australia

Ultraviolet radiation comprises a small region of the electromagnetic spectrum, from which its most energetic components (UVC and UVB) are fully and partially absorbed by the stratospheric ozone layer, respectively [4]. Excessive UV doses are harmful, resulting in sunburn and photoaging [4, 5]. Furthermore, UV radiation is considered a carcinogen, and thus, excessive UV exposure also results in skin cancer [4, 5]. Nevertheless, small doses of UV radiation are required to initiate the production of vitamin D in the human body [4]. Hence, UV exposure should not be avoided but instead limited in order to maintain adequate levels of vitamin D within the body, while reducing the likelihood of tumour development and further promotion. The three most common types of skin cancers are the basal and squamous cell carcinomas and melanoma. Melanoma is considered the deadliest form of skin cancer as it metastasises, and thus, it cannot be simply removed by surgery like basal and squamous cell carcinoma [5]. Over the past decade, skin cancer incidence rates have dramatically increased and has been speculated to be due to sociocultural and environmental changes, such as clothing, higher perceived value of tanned skin as well as depletion of the ozone layer [6, 7]. Ozone depletion in the months of spring and early summer is a significant factor in the increased levels of UV radiation in Australia, comparatively to worldwide levels, in addition to is relatively proximity to the equator and less industrial activity, resulting in less air pollution to scatter UV radiation [8]. These factors contribute to the substantially higher skin cancer rates within the Australian population, compared to the rest of the world [9]. Thus, research and development of new, improved, safer and more efficient UV filters is a necessity for protection against excessive UV exposure, and hence, the reduction of skin cancer rates in Australia and the rest of the world.

1.1.3 Nanoparticles for sunscreen UV filtration

Titanium dioxide (TiO_2) and zinc oxide (ZnO) nanoparticles have been approved by multiple governmental entities for their incorporation as active ingredients in sunscreen formulations for enhanced UV protection [10]. Sunscreens are emulsions composed of preservatives, additives and active ingredients that act as UV filters by absorbing, reflecting and/or scattering UV light [11]. Thus, they protect the human skin against potential detrimental health consequences of excessive UV exposure. These active

ingredients have historically been subcategorized as either organic or inorganic based upon their chemical composition and mechanism of UV protection. Organic UV filters are typically conjugated organic systems containing one or multiple aromatic rings within their structure [12]. These molecules dissipate absorbed UV light through chemical reactions [13]. These reactions often result in the decomposition of the molecule into toxic or allergenic by-products [13]. Hence, inorganic filters were introduced to overcome the shortcomings of unstable organic filters. As mentioned above, currently used inorganic UV filters comprise TiO_2 and ZnO semiconductor nanoparticles. These materials absorb UV radiation with higher or equal energy to their optical band gap through the promotion of an electron from the valence band to the conduction band, generating an electron-hole (e^-/h^+) pair [13]. Titanium dioxide has a variable band gap between 3.0 and 3.2 eV and zinc oxide has a band gaps of 3.3 eV [11]. Hence, in this size range, these materials absorb UVA and UVB rays, and therefore, they offer broad spectrum protection and transparency as they do not absorb visible light, resulting in more aesthetically pleasant sunscreen products [11]. Furthermore, these nanoparticles are stable over long periods of time and do not cause allergic reactions when applied onto the skin [11]. Nonetheless, concerns have been raised regarding their safety and use in cosmetic products due to the biological and environmental threat these nanoparticles may impose as a result of their intrinsically high surface reactivity and uncertain toxicological potential [11]. Additionally, concerns also arise from the photocatalytic nature of these particles and their ability to generate reactive oxygen species (ROS) once excited upon UV exposure through photochemical reactions of the formed e^-/h^+ pair with surface adsorbed water molecules [14]. These species can further react with the organic components of a sunscreen, leading to their decomposition and reduced Sun Protection Factor (SPF) [15]. Moreover, excess ROS can lead to oxidative stress, which in turn, leads to cell death and several diseases including cancer [16-18]. Multiple papers have reported the use of highly active TiO_2 nanoparticles in commercial sunscreen products; thus, safer materials are needed [19, 20]. Nevertheless, toxicological assessments of these particles have reported inconclusive results due to the differences in protocol and lack of real conditions, including the absence of UV irradiation or UV doses equivalent to those in the Northern Hemisphere [20-22].

1.2 Thesis structure

This Master thesis is comprised of five chapters which are outlined below:

Chapter 1 provides background information of the role of nanoparticles in cosmetic products, specifically in sunscreen formulations, as well as Australia's situation regarding skin cancer; which is the motivation for the research undertaken in this thesis. This chapter also outlines the structure of this thesis.

Chapter 2 provides a review of the current literature on the information outlined in Chapter 1. Firstly, the definition of UV radiation and its harmful effects in the human skin will be covered, followed by the special situation of Australia regarding skin cancer. Next, the issues surrounding UV filters in sunscreen products, current and potential solutions to reduce the photocatalytic activity of titania nanoparticles and its possible detrimental effects will be discussed. Lastly, the research objectives of this Master thesis will be outlined in the form of questions to answer with this research.

Chapter 3 specifies the materials used over the course of this research as well as the synthesis method employed to obtain coated titanium dioxide nanoparticles and the techniques used to characterise the composition, morphology, optical properties and photocatalytic activity of the synthesised materials. Described in this chapter is also the *in vitro* assay protocol employed to determine the cyto- and photo-toxicity of the as prepared nanoparticles in the absence and presence of simulated solar radiation.

Chapter 4 describes and extensively discusses the results obtained throughout this research on titanium dioxide nanoparticles covered with a thin yttrium oxide layer. This nanosystem is proposed to have improved UV absorption and free radical scavenging properties for enhanced UV filtration properties and biocompatibility of titania.

Chapter 5 concludes this thesis with a summary of the findings of this research in addition to suggested future research.

Chapter 2

Literature Review

2.1 Ultraviolet (UV) radiation

The radiation emitted by the sun covers the full electromagnetic spectrum, from cosmic rays to radio waves. Ultraviolet (UV) radiation comprises a very small part of this spectrum, from 100 nm to 400 nm. According to environmental and dermatological photo biologists, the UV region is subdivided into three bands associated with the biological effects of these different wavelengths: UVC (100-280 nm), UVB (280-320 nm) and UVA (320-400 nm) [4, 20, 23]. The ultraviolet type A can also be further subdivided into: short UVA (320-340 nm) and long UVA (340-400 nm) [24, 25]. However, the ozone layer behaves as a filter by absorbing radiation with wavelengths shorter than 315 nm; thus, stratospheric ozone prevents UVC radiation from reaching the Earth's surface, whilst also greatly reducing the amounts of incident UVB. As such, the ultraviolet radiation bands of concern to human health comprise the UVA and part of the UVB wavelength regions [4, 8, 23, 26].

2.1.1 UV radiation, oxidative stress and human health

Ultraviolet radiation is a prominent cause of oxidative stress brought about by excessive production of reactive oxygen species (ROS) within the body. Ultraviolet radiation can inhibit enzymatic and/or antioxidative processes needed to counter ROS, thus leading to an imbalance and oxidative stress [16-18]. The reactive species of most concern are

hydrogen peroxide (H_2O_2), free radicals such as the superoxide ion ($^{\bullet}O_2^-$) and hydroxyl radical ($^{\bullet}OH$) [27, 28]. The mitochondrial respiratory chain is the main biological source of free radicals. They are produced as a by-product due to a fault in the electrochemical reduction of O_2 to water by the electron transport chain, resulting in H_2O_2 and $^{\bullet}O_2^-$ [27, 28]. However, UV light can also generate $^{\bullet}O_2^-$ by electron transfer from an excited state molecule, such as phenolic moieties in effluent organic matter, to molecular oxygen [28]. States of oxidative stress are detrimental to human health since they can lead to apoptosis and have been implicated in multiple diseases, including Alzheimer's, Parkinson's, amyotrophic lateral sclerosis, diabetes, blindness, and cardiovascular diseases (Figure 2.1) [16-18].

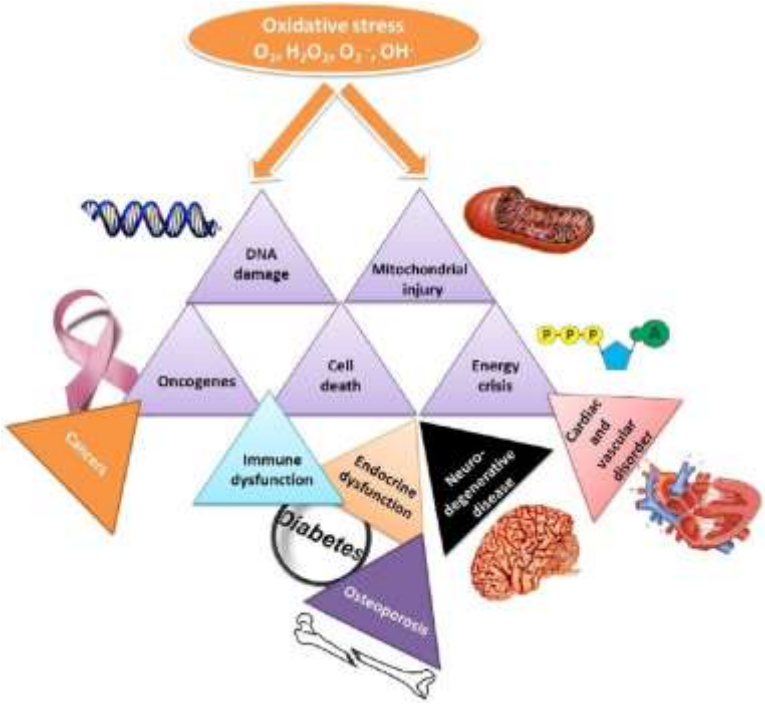

Figure 2.1: Biological effects of oxidative stress and the potential diseases associated with the excessive ROS. Figure reproduced from Saeidnia et al. (2013) [17].

2.1.2 The human skin

The skin is the largest organ of the body [4, 29]. It acts as a physical barrier, protecting the human body against external factors both chemical and physical, such as microbial pathogens. Furthermore, it prevents water loss and covers functions like sensation and thermoregulation. It is also involved in the synthesis of vitamin D upon short term

exposure to UV light. However, long term exposure to UV light can cause detrimental effects to the skin, as will be discussed [1, 4, 29-31]. The human skin is composed of three main layers [32]: the epidermis, the dermis and hypodermis (Figure 2.2) [4]. The outermost layer is the epidermis, a self-renewing tissue through cell division in the stratum basale (germinative compartment). The epidermis is composed of stratified squamous epithelium consisting mainly of keratinocytes (up to 90%) and comprises many layers, which represent the different stages of cell division and their migration outward to form the stratum corneum from basal keratinocytes. Beneath the epidermis lies the dermis, these two layers are separated by a basement membrane [4]. It is composed largely of fibroblasts, collagen and elastin, providing the skin with structural, supportive and elastic properties along with nutrients to the epidermis. Hair follicles, sweat glands, small blood vessels, sensory nerves and eccrine glands are found in the dermis [4]. Under the dermis lies the hypodermis, which accommodates blood vessels and adipocytes whose accumulation of fat provides energy to the metabolism and has a cushioning action [1, 4].

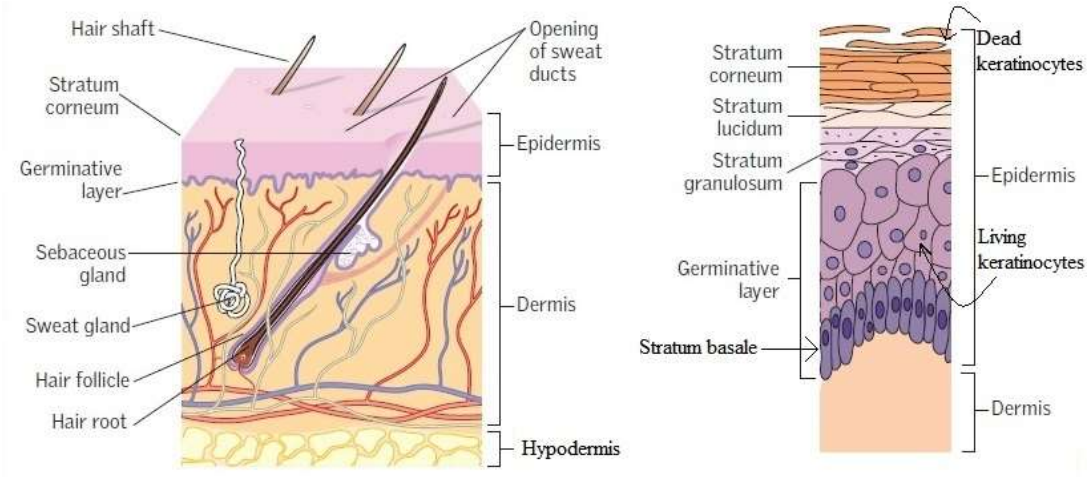

Figure 2.2: Scheme of the human skin layers. Figure adapted from McLafferty *et al.* (2012) [29].

2.1.3 Effects of UV radiation on the human skin

The interaction of UV radiation on the human skin can cause both beneficial and adverse health effects. The dose of UV radiation obtained is an important factor that is the determinant between the two effects. The most commonly known adverse health effect of excessive UV exposure is skin cancer. Other adverse health consequences important to consider include skin sunburn or erythema and photoaging. However, in small doses

UV radiation has beneficial impacts for the human health since it helps to bring about the synthesis of vitamin D.

2.1.3.1 Synthesis of vitamin D

As mentioned before, in small doses UV radiation is crucial for the synthesis of vitamin D in the skin [4]. Upon exposure to UVB, stored cutaneous 7-dehydrocholesterol is converted to pre-vitamin D_3 over the epidermis and dermis, which then undergoes, through a temperature dependent isomerisation, conversion to vitamin D [33-35]. The synthesised vitamin D is then released into the circulatory system by vitamin D-binding proteins for 3 days [33, 35]. Vitamin D is an essential hormone for developing a healthy musculoskeletal system since it allows and controls the absorption of calcium from the small intestine. As such, its deficiency has been linked to rickets and osteomalacia in children and adults, respectively; in addition to multiple sclerosis, cardiovascular diseases and multiple cancers [7, 31, 36, 37].

2.1.3.2 Sunburn

Sunburn, or erythema, is the most commonly known acute effect of excessive solar UV exposure, characterised by an inflammatory response of the skin [4]. This reaction is mainly caused by UVB rays which penetrate the upper epidermal layers of the skin [4]. The minimum dose of UVR that produces erythema 8 or 24 hours after UV exposure is termed the Minimal Erythema Dose (MED) [4, 38]. Erythema tends to fade away within one to two days after appearance; however, continuous UV exposure shortens its reappearance time while increasing its intensity and extending its persistence. Ultimately, high UV doses cause oedema, aching, blistering and peeling [38].

2.1.3.3 Photoaging

Photoaging, or early skin aging, is the result of DNA damage in skin stem cells found in the inner and outer layer of the dermis and epidermis, respectively, upon chronic excessive UV exposure [4, 39]. This damage is due to the structural reordering of nucleotides produced by the absorption of UVB photons, which cause irregularities in the DNA strand structure. Additionally, absorption of UVA photons results in the formation of ROS, and consequently oxidative stress, by charge transfer from cellular photosensitisers to oxygen molecules [39, 40]. Photoaging is characterised by dryness,

wrinkles, skin atrophy and uneven pigmentation and it is known to decrease the levels of antioxidants within the skin [4, 38-40].

2.1.3.4 Skin cancer

Skin cancer is the most common human cancer and is related to excessive chronic UV exposure. On one hand, UVB rays can interact with certain cellular membranes [4, 26] and be absorbed by DNA strands, causing subsequent DNA mutations [8, 41, 42]. Furthermore, the tumour suppressor gene p53 is often found mutated in skin cancers, resulting in the loss of its tumour suppression functions, including regulation of the cell cycle, DNA repair and apoptosis [43]. On the other hand, UVA rays can reach the dermis, where they are absorbed by skin chromophores bringing about the production of ROS in dermal fibroblasts and extracellular structures [4, 41, 42]. This leads to oxidative stress, resulting in oxidative damage, mutations in gene expression and DNA lesions. If cell division takes place while the damage has not been repaired, the photolesions may result in mutations being integrated into daughter DNA causing genetic instability, a key factor in the initiation of the carcinogenic process in skin [8].

Types and incidence

The three main types of skin cancers associated with UV exposure are basal cell carcinoma (BCC), squamous cell carcinoma (SCC) and melanoma [8, 44]. The head, neck, arms and hands are the areas of the body where BCC and SCC are most frequently formed since these areas are regularly exposed to UV radiation. Basal and squamous cell carcinoma are often removed by surgery; however, melanoma tends to metastasise and is accountable for most skin cancer associated mortalities [4, 38].

The incidence of skin cancer is increasing due to the change in human behaviour, such as clothing, perceived higher value of tanned skin over pale skin, desire for sun-seeking holidays and the use of sun beds [7]. Annually, in the United States alone, 3.5 million people are expected to be affected by some type of skin cancer, which imposes an economic and emotional burden to the patients and their closest friends and family [45, 46].

2.1.4 Solar UV radiation in Australia

The amount of solar UV radiation incident on the Earth's surface is highly dependent on the latitude; hence, the latitudes closest to the equator receive higher UV doses than either of the poles. Furthermore, clearer skies due to less industrial activity leads to lower levels of particulates and aerosols to absorb, reflect or scatter solar radiation [8]. As such, the Southern Hemisphere receives increased levels of solar radiation as represented in Figure 2.3 by a higher UV index value, an indicator of the intensity of UV radiation incident on the earth's surface. In the Southern Hemisphere, Australia is particularly exposed to extremely high UV levels due to stratospheric ozone depletion [8, 23]. Because of the increased level of incident UV, Australia has one of the highest rates of melanoma worldwide, two to three times the rates in Canada, the USA and the UK. As such, effective protection against UV radiation is a necessity [9].

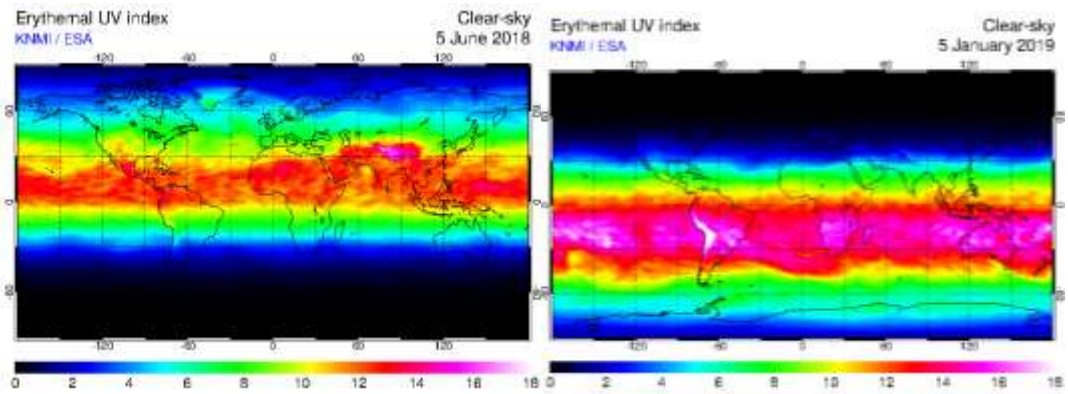

(a) (b)

Figure 2.3: Global erythemal UV index in the last Australian (a) winter and (b) summer. Figure reproduced from TEMIS (2019) [47].

2.2 Sunscreen products and Sun Protection Factor (SPF)

Protective measures, such as the use of clothing, hats, sunglasses, and sunscreens, are encouraged by governmental entities in order to minimise sunlight exposure and its detrimental effects [44]. However, the most common method used to limit and protect the skin from UV radiation is the application of sunscreen on skin prior to outdoor activities. Sunscreens are emulsions composed of preservatives, additives and active ingredients that act as UV filters, i.e. chemicals that transform, disperse, absorb or reflect UV light,

protecting the skin against UVA, UVB rays or both (broad spectrum filters) [11, 48, 49]. The protection efficiency of these filters is known as the Sun Protection Factor (SPF) rating, defined as the minimal erythema dose of UVB radiation required to produce sunburn on protected skin compared to non-protected skin (Equation 2.1) [50, 51]. Thus, sunscreens that are labelled with the same SPF value might display similar UVB absorbance levels but diverse UVA absorbance [52]. The multiple SPF ratings of sunscreens arise from the difference in active ingredients constituting the sunscreen formulation and their loading amount, resulting in SPF ratings from 4 to 100+. Nevertheless, many countries, Australia included, only allow a maximum SPF value of 50+ on sunscreen labels [53]. The higher the SPF rating, the higher the provided protection against erythema; however, the amount of sunscreen applied by users is lower than that recommended (2 $mg \cdot cm^{-2}$), unknowingly exposing them to high UV doses. Theoretical models and *in vivo* experiments have shown that the applied amount of sunscreen and its SPF rating are exponentially related [54].

$$SPF = \frac{\text{minimum erythema dose on sunscreen-protected skin}}{\text{minimum erythema dose on non-sunscreen-protected skin}} \quad (2.1)$$

The aforementioned active ingredients in sunscreen products are classified as ‘organic’ and ‘inorganic’ UV filters. The former comprises organic molecules that absorb specific UV wavelengths and the latter are semiconductor nanoparticles that absorb, reflect and scatter the incident UV radiation [49, 55].

2.2.1 Organic UV filters

Organic UV filters are conjugated organic systems containing one or multiple aromatic rings within their structure, as shown in Figure 2.4 [12]. These molecules absorb UV photons, resulting in the promotion of an electron in the highest occupied molecular orbital (HOMO) to the lowest unoccupied molecular orbital (LUMO), forming a singlet state (Figure 2.5 (a)) [13]. Such singlet state electrons can dissipate the excess energy absorbed via emission of another photon through fluorescence or undergoing photochemical reactions [13]. Nevertheless, in certain instances, the singlet state may undergo intersystem crossing, resulting in a triple excited state [13]. De-excitation in this triplet state can happen through photon emission, also known as phosphorescence, photochemical reactions or energy transfer to other molecules (Figure 2.5 (b)) [13].

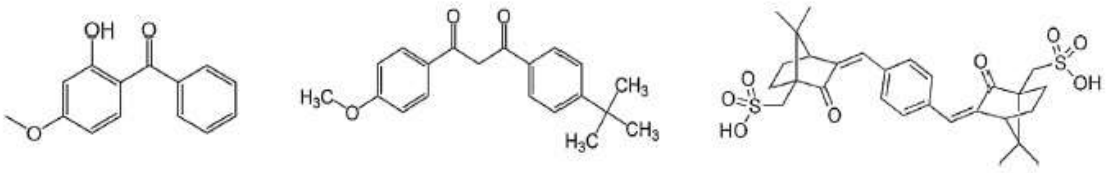

Figure 2.4: Chemical structure of three commonly used organic UV filters in sunscreen products. From left to right: oxybenzone, avobenzone and ecamsule. Figure reproduced from Abid *et al.*(2017) [56].

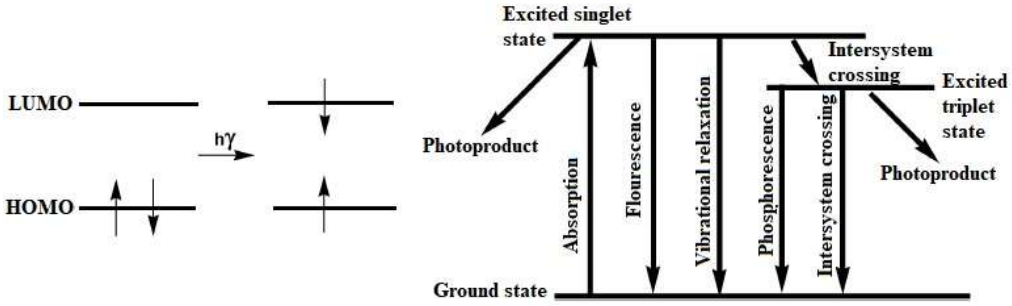

(a) (b)

Figure 2.5: (a) Absorption of a photon with enough energy to generate a singlet state through a HOMO-LUMO electron transition and (b) multiple de-excitation pathways of an absorbed photon. Figure adapted from Shaath (2010) [13].

As such, these molecules exhibit strong and narrow UV absorption bands of specific wavelengths; thus, they are usually classified as UVA or UVB filters [13]. Therefore, multiple organic filters are often used synergistically to provide broad spectrum protection.

2.2.1.1 Risks of organic UV filters

The use of organic filters in sunscreen products has raised safety concerns as many of these compounds are chemically unstable when exposed to UV light, resulting in their photodegradation and subsequent loss of UV filtering behaviour [57]. Consequently, users are unknowingly exposed to higher levels of UV radiation. Furthermore, if absorbed and photodegraded, the generated reactive species could cause allergic reactions and, moreover, interact with lipids, proteins and even the DNA [58]. In addition, recently, it has been found that these filters impose a threat to the environment [59, 60].

Lack of Photostability

As mentioned before, upon UV absorption many organic filters can undergo photochemical reactions, which change their physical properties and reconfigure their chemical structure, resulting in the formation of unstable or reactive by-products, including free radicals (examples shown in Figure 2.6) [13]. These, in turn, can interact with the skin, causing photoallergy and/or photocytotoxicity as well as react with other UV filters or ingredients present in the sunscreen formulation decreasing the product's SPF rating [52, 57].

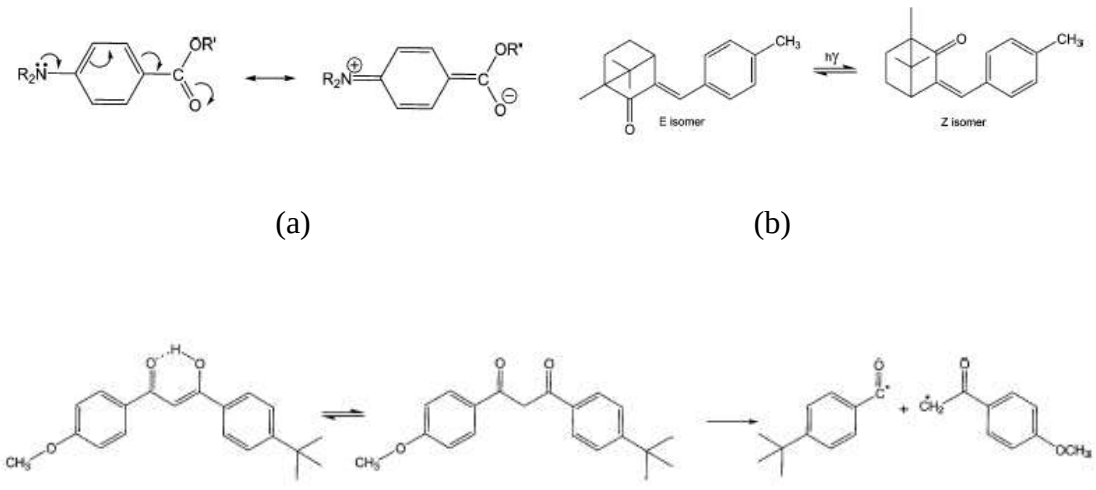

(a) (b)

(c)

Figure 2.6: (a) Electron delocalisation of para-aminobenzoic acid (PABA) upon UV absorption, (b) photoisomerization of a camphor derivative and (c) keto-enol tautomerization of avobenzone followed by the fragmentation of the keto form upon UV irradiation. Figure adapted from Shaath (2010) [13].

The changes in the chemical structure of these filters lead to a loss in absorbance. Such an effect has been widely studied and is highlighted in Figure 2.7 (a), where the UV absorption spectra of common UVB (ethylhexyl *p*-methoxycinnamate, OMC) and UVA (butylmethoxydibenzoylmethane, BMDBM, and avobenzone, AVOB) filters changes after UVA exposure because of photo-induced isomerization. The observed reduction in absorbance of OMC is due to the *cis-trans* isomerization whereas, in the case of BMDBM and AVOB, the decrease in absorbance is attributed to a keto-enol isomerization [52]. As shown in Figure 2.7 (a), in its enol form, AVOB absorbs UVA at 357 nm [57]. However,

in its keto form, it absorbs in the UVC region, rendering avobenzone ineffective as a UVA filter [57]. Additionally, upon further UV exposure, BMDBM and AVOB undergo cleavage and fragmentation, respectively, resulting in the generation of reactive radical species [52, 57]. *In vitro* studies have shown that such species accelerate the degradation of other filters and can cause DNA and protein damage [58].

In order to achieve broad spectrum protection, prevent loss of photoprotection and reduce the amount of formed reactive species, multiple UV filters, stabilisers and antioxidants are used synergistically in sunscreen formulations [57]. Figure 2.7 (b) shows the effect of UVA radiation in the absorbance and lipid peroxidation, as a result of free radical generation, of three commercial sunscreens [52]. A reduction in UV absorption and increase in thiobarbituric acid reactive substances (TBARS), a marker/control of lipid peroxidation, can be seen in all the sunscreens after UVA exposure. Sunscreen A contained multiple BMDBM stabilisers whereas sunscreen B and C contained one and none, respectively; translating in a smaller TBARS increase in sunscreen A, followed by B and C. Additionally, sunscreen A had less BMDBM and more antioxidants than B and C, also contributing to the lower TBARS concentration. These results highlight the importance of the sunscreen composition when it comes to photostability and human safety. Thus, even though sunscreen C had a higher amount of UV filters, resulting in a higher SPF value, the lack of stabilisers caused a noticeable loss of UVA absorption. Furthermore, this sunscreen also contained photocatalytically active TiO_2, which accelerated the degradation of the organic components in the sunscreen formulation when irradiated (this characteristic will be further examined in Section 2.2.2.2) [52].

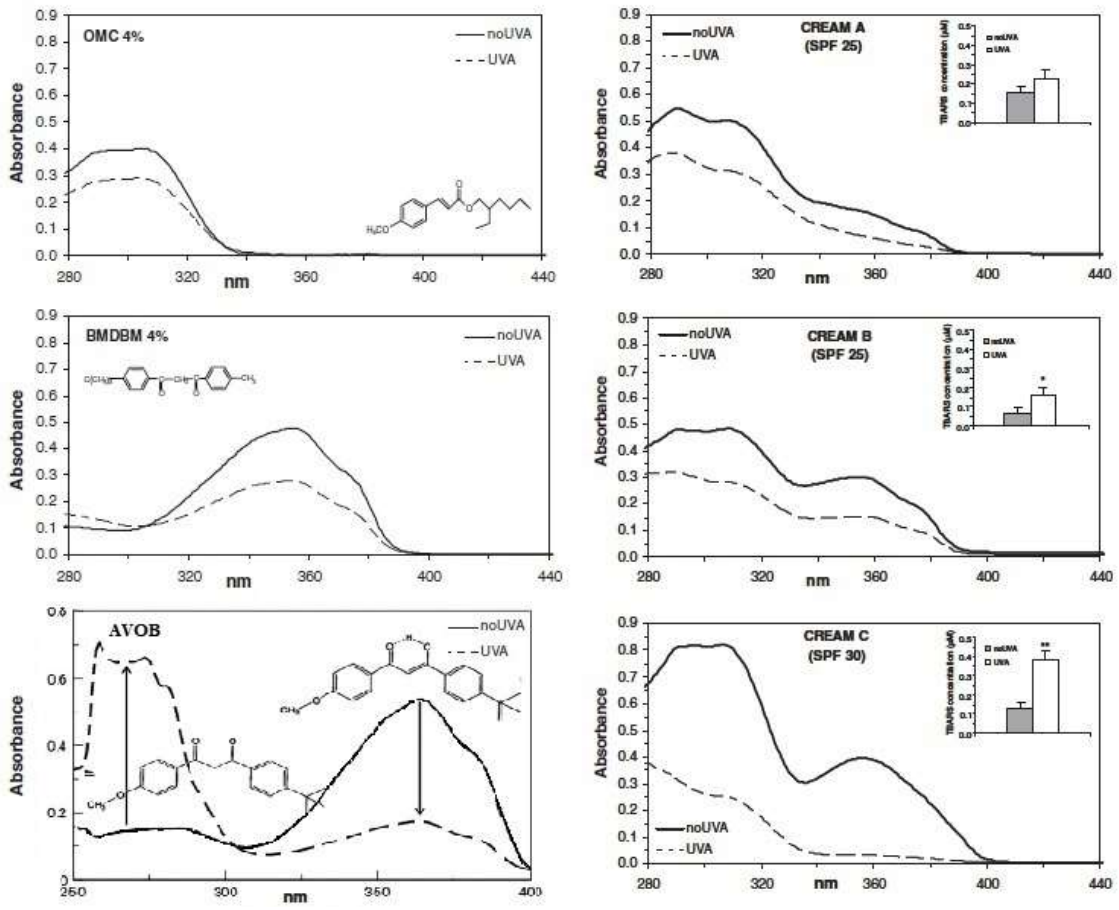

(a) (b)

Figure 2.7: Change in the absorption spectra of (a) OMC, BMDBM and AVOB and (b) three commercial sunscreens and concentration of TBARS after UVA exposure (dashed line and white column). Figure adapted from Damiani *et al*. (2010) and Afonso *et al*. (2014) [52, 57].

Allergic and photoallergic contact dermatitis

Organic filters and their photodegradation by-products can cause allergic and photoallergic contact dermatitis, respectively [61]. The frequency of such reactions due to sunscreen products is not clear; however, it has been estimated to be up to 40%, and increasing in users with photosensitivity history [61]. In the late 90s, multiple commonly used organic filters, such as oxybenzone, PABA and its derivatives, were found to cause allergic and photoallergic reactions, leading to their reduction or replacement within sunscreen products [61]. Cinnamate and salicylate based UVB filters were used to replace PABA due to their higher stability, solubility and lower photo-/allergenic reactions [61]. Octocrylene and the photoproducts of avobenzone have also been found to be strong

sensitisers [61, 62]. These allergic reactions are one of the incentives behind the incorporation of inorganic filters in sunscreen formulations, as these are unlikely to cause allergic responses even at high concentrations.

Ecotoxicity

Organic filters are released to the environment through recreational water activities and wastewater treatment plants, where they can bioaccumulate and impart toxicity to biota [59, 60]. An important ecosystem under threat by these UV filters are coral reefs. Upon exposure to cosmetic products containing organic filters, corals release mucous composed of coral tissue and symbiotic algae, inducing coral bleaching [60]. Thus, the use of sunscreen products containing organic filters has been banned in multiple tourist destinations, such as marine ecoparks in Mexico, the island nation of Palau, Hawaii and Key West, Florida. [59, 60, 63]. More recent news has revealed the potential danger such filters may pose to the Great Barrier Reef in Queensland, Australia.

Organic filters impose a threat to humans and the environment due to the reasons described above; hence, they have been banned in some regions. To overcome the drawbacks associated with these filters, inorganic nanoparticles are used in sunscreen products as UV filters.

2.2.2 Inorganic UV filters

Multiple organic compounds are certified as UV filters; however, as regulated per the Therapeutic Goods Administration (TGA), TiO_2 and ZnO nanoparticles are the only two inorganic materials approved for use in sunscreen products; the former being the most commonly used [10]. For instance, in Australia it is estimated that TiO_2 nanoparticles are present in 70% of sunscreen products whereas 30% contain ZnO nanoparticles [6]. These particles are semiconductors that, as shown in Figure 2.8 (a), reflect and scatter UV radiation [13]. Furthermore, they also absorb incident UV photons with energy greater than their band gap through the promotion of an electron from the valence band (VB) to the conduction band (CB) (Figure 2.8 (b)) [13].

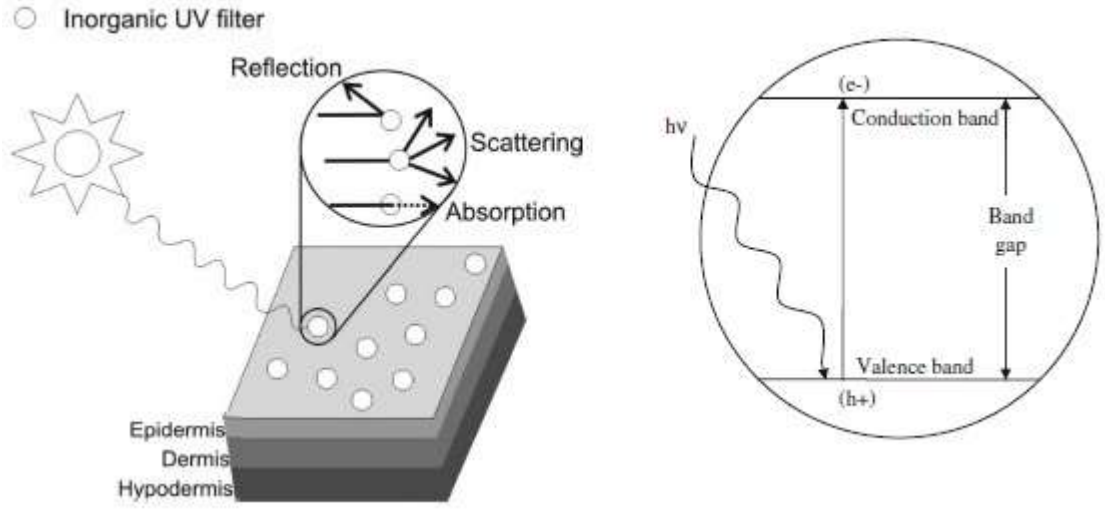

(a) (b)

Figure 2.8: (a) Protection and (b) absorption mechanisms of inorganic UV filters. Figures reproduced from Manaia *et al*. (2013) and Hanaor *et al*. (2011), respectively [11, 64].

In the nanometre regime, these metal oxides show improved spectroscopic and cosmetic properties compared to their micron scale counterparts as they appear transparent. Furthermore, they offer high photostability, non-irritability and broad UV spectrum protection (Figure 2.9) compared to organic filters [11, 48, 49, 55]. Nevertheless, the use of TiO_2 and ZnO nanoparticles in cosmetics and sunscreen formulations is of great concern due to the uncertainties regarding their ability to be absorbed through the skin, reach viable cells and cause photocytotoxicity [1], leading to photocarcinogenesis [65]. Simple toxicity tests in the past either use an inappropriate grade of titanium dioxide or do not include UV light in the evaluation [21].

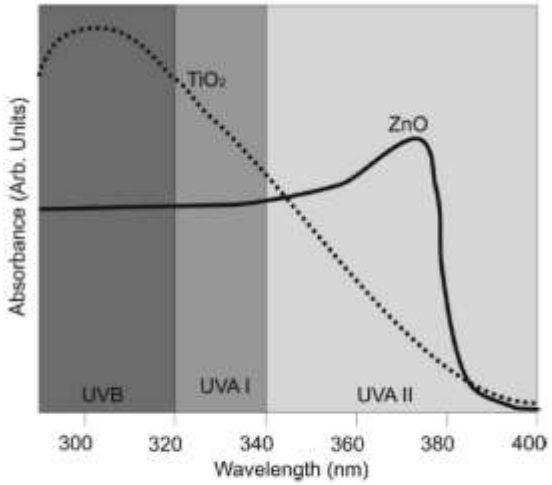

Figure 2.9: UV-vis absorbance of TiO_2 and ZnO nanoparticles. Figure reproduced from Manaia *et al.* (2013) [11].

2.2.2.1 Zinc oxide

Zinc oxide (ZnO) is a white, odourless and insoluble powder widely used in optoelectronic devices, as a photocatalyst in the degradation of organic environmental contaminants, as an antimicrobial agent and as a UV filter in cosmetic products due to its low cost [66-68]. As highlighted in Figure 2.9, zinc oxide nanoparticles exhibit broad band absorption across the UVB and UVA spectrum.

Crystal phases

Zinc oxide is found in three crystallographic forms which are wurtzite, zinc blend (cubic) and rock salt (Figure 2.10). The most stable at ambient conditions, and therefore, the most common, is wurtzite with an energy band gap of 3.4 eV [66]. The band gaps of zinc blend and rock salt crystal structures are 3.25 and 4.05 eV, respectively [66].

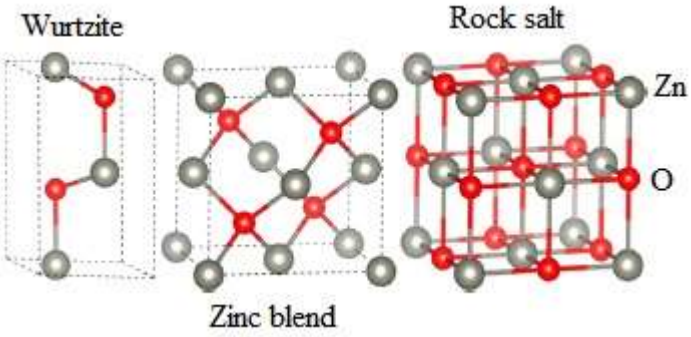

Figure 2.10: Ball and stick model of the unit cell of wurtzite, zinc blend and rock salt ZnO crystal phases where O and Zn atoms are represented by red and grey balls, respectively. Figure adapted from Ma *et al.* (2013) [66].

Solubility and photocorrosion of ZnO

The dissolution and photocorrosion of ZnO raises concerns over its use in cosmetic products, such as sunscreens. It is known that this metal oxide solubilises into Zn^{2+} (Equation 2.2) at a wide range of pH, which could potentially result in toxicity to humans and the environment [69, 70]. Furthermore, due to the higher surface area and reactivity of nanoparticles, the solubility of nano-ZnO is enhanced [70]. Moreover, zinc oxide is not photostable and it decomposes in aqueous solutions under UV exposure to once again give Zn^{2+} and oxygen through the reaction of ZnO with the holes formed in the valence band (h^{+}_{VB}) (Equation 2.3) [68].

$$ZnO + H_2O \leftrightarrow Zn^{2+} + 2OH^- \quad (2.2)$$

$$ZnO + 2\ h^{+}_{VB} \rightarrow Zn^{2+} + \tfrac{1}{2}\ O_2 \quad (2.3)$$

2.2.2.2 Titanium dioxide

Titanium dioxide (TiO_2), also known as titania, is present in paints as a pigment, and in toothpastes and cosmetics, among other products [71-73]. Titania is also used in medicine for drug delivery as a TiO_2-DNA oligonucleotides complex [74]. As a photocatalyst, titania is used in the treatment of contaminated air and waterways through the decomposition of organic and gaseous pollutants and, in dye-sensitised solar cells (DSSCs), it is used for the conversion of UV light into energy [75]. Titanium dioxide is also extensively used as a UV filter in sunscreens [76]. Nevertheless, these applications

are dependent on the physical properties of TiO_2, which in turn, depend primarily on the particle size, morphology and crystal phase of the material.

Crystal phases

Titanium dioxide is commonly found in three crystallographic forms which are rutile, anatase and brookite (Figure 2.11). Only the rutile phase or mixtures of anatase and rutile are found in sunscreens [11, 77]. In some formulations, the anatase to rutile ratio has been found to be up to (85-75):(15-25), which is similar to a commercially sold photocatalyst powder known as P25 or Degussa P25 [11, 77]. Both phases, rutile and anatase, have tetragonal crystal structures; however, the rutile form is more thermodynamically stable than the anatase phase [11, 64, 77, 78]. Thus, upon heat treatment, the anatase phase transitions irreversibly to rutile at temperatures between 500 and 700 °C, depending on the purity of the initial phase, grain size, morphology and the thermal treatment method employed [64, 79]. For example, Wetchakun *et al*. (2012) reported this phase change on anatase TiO_2 nanoparticles synthesised through a sol-gel-method, where the transition temperature to rutile was found to be between 500 and 600 °C. At 600 °C or above, the anatase nanoparticles were transformed completely to the rutile phase [80]. Also, the average particle size of the nanoparticles annealed for 3 hours between 400 and 600 °C in air was between 10 and 50 nm. Above 600 °C, particle size growth, agglomeration and, therefore, lower surface area were favoured [80]. Such an outcome is not desirable for UV filtering since it would result in a decrease in UV absorptivity and increase scattering within the visible light region.

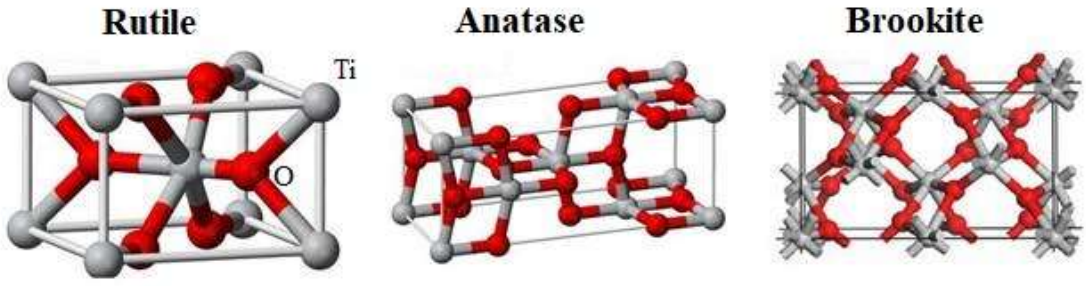

Figure 2.11: Ball and stick model of the unit cell of rutile, anatase and brookite TiO_2 crystal phases where O and Ti atoms are represented by red and grey balls, respectively. Figure reproduced from PaveMaintenance [81].

Furthermore, both crystal phases, anatase and rutile, are photocatalytically active. However, due to the greater surface area of the anatase form, its photocatalytic activity and adhesion to the skin is higher than that of the rutile phase [11, 20, 65, 77]. Such photocatalytic activity results in the formation of reactive oxygen species (ROS).

Photocatalytic activity of TiO_2: free radical generator

As mentioned in Section 2.2.2, titanium dioxide is a semiconductor, therefore it consists of an energy band gap (*Eg*) small enough for electrons in the valence band (VB) to be excited and promoted to the conduction band (CB) through irradiation with stronger energy than its *Eg*. The band gap energy of TiO_2 is crystal phase dependent [80]. Thus, the *Eg* of the anatase and rutile phases are 3.20 eV and 3.02 eV [80], respectively, which corresponds to wavelengths across the UV region. Under UV radiation of sufficient energy, an electron from the VB is promoted to the CB, generating an electron-hole (e^-/h^+) pair on the TiO_2 surface, as highlighted in Figure 2.12 and Equation 2.4 [82-84]. This principle forms the basis for the mechanism of photocatalysis.

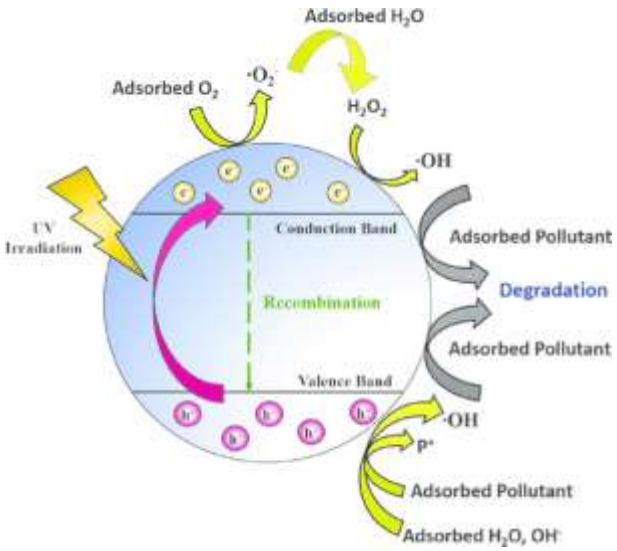

Figure 2.12: Schematic diagram of the photocatalytic mechanism of TiO_2 particles. Figure reproduced from Leong *et al.* (2016) [14].

In an aqueous medium, the photogenerated e^-/h^+ pair on the surface of TiO_2 undergoes redox reactions with H_2O, OH^- and O_2 (in aerated solutions), resulting in the production of ROS, as highlighted in Equations 2.4-2.7 [15, 82-84]. The generated h^+ in the valence

band is extremely oxidizing and, as such, it oxidises adsorbed H_2O and OH^- molecules resulting in $^{\bullet}OH$ (Equations 2.5 and 2.6); these reactions have also been reported in ambient air [28]. The generated $^{\bullet}OH$ can further react with organic compounds present in solution or in sunscreen formulations for instance, resulting in decomposition of other active ingredients [83]. In a similar fashion, the produced $^{\bullet}O_2^-$ (Equation 2.7) also decomposes organic compounds [15]. Thus, as mentioned in Section 2.2.1.1, generation of these free radicals can compromise the protection against UV radiation provided by sunscreen products.

$$TiO_2 + h\nu \rightarrow e^- + h^+ \quad (2.4)$$

$$H_2O + h^+ \rightarrow {}^{\bullet}OH + H^+ \quad (2.5)$$

$$h^+ + OH^- \rightarrow {}^{\bullet}OH \quad (2.6)$$

$$O_2 + e^- \rightarrow {}^{\bullet}O_2^- \quad (2.7)$$

As previously mentioned, the photocatalytic activity of TiO_2 is of interest for environmental protection. For example, in water/air purification and renewable energy production through DSSCs [64]. However, in a biological context, the generated free radicals could potentially result in states of oxidative stress and subsequent apoptosis. As a result, on one hand, studies have reported that TiO_2 is phototoxic due to the generation of free radicals and, as such, concerns have been raised regarding its use in sunscreens as a UV filter. Yet, on the other hand, a lack of toxicity of TiO_2 in the absence of UV light has also been reported.

2.3 Reported inconclusive toxicity of inorganic UV filters

The effectiveness of the inorganic filters used in sunscreens, TiO_2 and ZnO, depends mainly on their particle size. This in turn, also affects the potential to induce phototoxicity and the capacity for these particles to enter the human body; for example, through inhalation (respiratory tract), ingestion (gastrointestinal tract) and dermal penetration [1, 11]. As mentioned above, multiple studies have investigated the toxicity of inorganic filters without reaching a consensus, as such, concerns have been raised regarding their use in sunscreen products. A reason for this lack of conclusiveness could be due to the

fact that there are no guidelines for skin toxicity as there are for skin sensitisation and corrosion [85-88]. Combined with unrealistic conditions and the difference in methods/protocols and materials tested

2.3.1 Reported lack of toxicity

A number of *in vivo* and *in vitro* studies [22, 89-93] have reported that neither TiO_2 nor ZnO nanoparticles in sunscreen products are toxic to the human body. For example, an *in vivo* study by Popov *et al.* (2009) involved the application of a sunscreen containing rutile TiO_2 (100 nm) onto the flexor forearm skin 5 times per day over a period of 4 days [94]. It was shown that the production of free radicals generated by the skin upon UV light exposure surpassed that of the particles [94]. The same results were obtained when an *in vitro* test was performed on porcine skin, supporting the previous finding [94]. In the presence and absence of UVA and UVB light ZnO particles (< 200 nm) did not display signs of DNA damage in HaCaT cells in a concentration range between 1.95 and 32.5 $\mu g \cdot mL^{-1}$ [95]. Also, ZnO nanoparticles were identified as nontoxic by Kim *et al.* (2017) in animal models; additionally, the potential use of these particles in cancer treatment was highlighted as they are more cytotoxic against cancer cells than normal cells [22]. In a review based on the safety of TiO_2 and ZnO nanoparticles in sunscreens by the Therapeutic Goods Administration (TGA) (2016) it was concluded that there is no sufficient evidence of toxicity caused by these inorganic filters used in sunscreen products [77].

2.3.2 Reported toxicity

The toxicity of ZnO and TiO_2 nanoparticles (50 - 70 nm and < 150 nm, respectively) in human skin fibroblasts in the absence of UV light was assessed by Dechsakulthorn *et al.* (2008). A reduction in cell viability was observed in cells exposed for 24 hours to both nanomaterials. Titania showed similar cell viability reduction following a 4 and 24 hour post-exposure time period. Nevertheless, cell viability reduction due to 4 hour ZnO exposure was negligible. However, a substantial reduction in cell viability was obtained after exposure to ZnO for 24 hours, as highlighted in Figure 2.13 (a) [21]. From these curves, the inhibitory concentration (IC_{50}) (24 hours) values for ZnO and TiO_2 were determined to be (50 ± 13) and (2.70 ± 0.67)×10^3 $mg \cdot L^{-1}$, respectively [21].

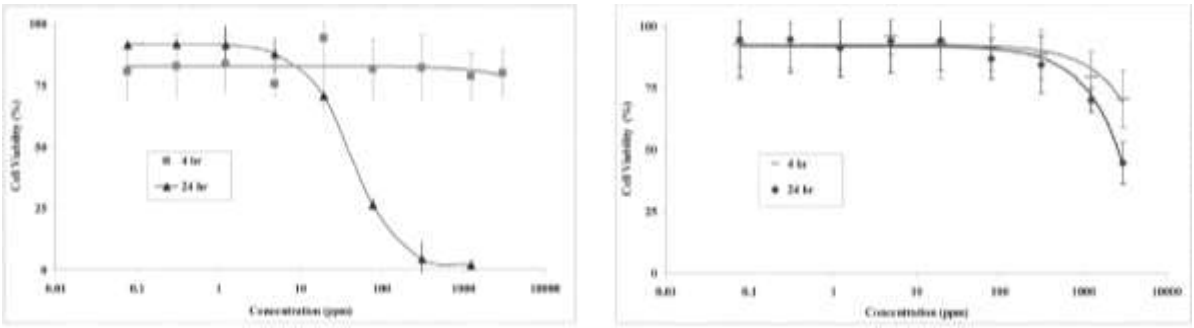

(a) (b)

Figure 2.13: Dose-response curves obtained after 4 and 24 hours exposure to (a) ZnO and (b) TiO_2 in human skin fibroblast. Figure adapted from Dechsakulthorn *et al.* (2008) [21].

The mechanism by which ZnO nanoparticles induce toxicity has been widely studied and the main causes of toxicity are the release of Zn^{2+} ions and production of ROS, resulting in oxidative stress, which happens to be similar mechanisms to that of its bulk counterpart [1, 49]. In order to reduce the cytotoxicity of ZnO, Yin *et al.* (2010) coated ZnO nanoparticles with silica (SiO_2) and poly (methyl-acrylic) acid (PMAA). It was established that neither of the coatings altered the filtering property of the core nanoparticles; however, ZnO and ZnO@SiO_2 exhibited similar cytotoxicity to human lymphoblastic cells, while ZnO@PMAA nanoparticles only had an adverse effect at high concentrations [96].

Several studies have compared the cytotoxicity and capacity to form ROS of the anatase and rutile crystalline forms [11, 19, 77, 82]. For example, Yin *et al.* (2012) assessed the *in vitro* toxicity in HaCaT cells under UVA (340 nm) irradiation of four TiO_2 samples: two anatase samples that were 25 and 325 nm in size (A25 and A325), one rutile phase of 100 nm in size (R100) and one P25 (86:14 anatase:rutile ratio) sample 35 nm in size (P25) [82]. No toxicity was found towards HaCaT cells exposed to TiO_2 or UVA alone, in disagreement with Dechsakulthorn *et al.* (2008). However, a dose- and concentration-dependant toxicity was caused by A25, A325 and P25 samples under UVA irradiation. Only a small reduction in cell viability was produced by R100 at high concentrations (100 $\mu g \cdot mL^{-1}$) (Figure 2.14 (a)). It was determined by electron spin resonance (ESR) that this toxicity was due to the generation of free radicals in the presence of UVA

(Figure 2.14 (b)). Furthermore, larger particles produced less ROS, and thus decreased phototoxicity [82].

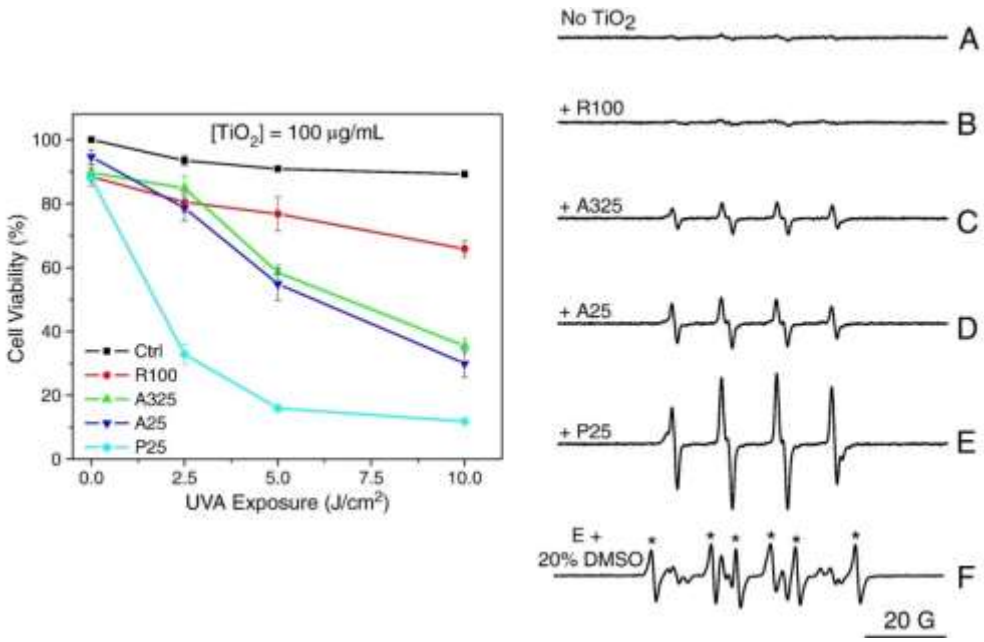

(a) (b)

Figure 2.14: Effect of the four TiO_2 samples exposed to UVA in (a) HaCaT cell viability at different UVA irradiation dosages and (b) the generation of hydroxyl radical (ESR spectra). Figure adapted from Yin *et al.* (2012) [82].

Another study by Xue *et al.* (2015) reported results in concordance with those obtained by Yin *et al.* (2012) regarding the photoinduced ROS generation. It was found that HaCaT cells exposed to 200 $\mu g \cdot mL^{-1}$ of P25 (21 nm, 75:25 anatase:rutile ratio) for 24 hours and irradiated with UVA (365 nm) increased the accumulation of intracellular ROS level by 1.8-fold, compared to the control group, and reduced the mitochondrial membrane potential [97, 98]. Similarly, in a recent study, where HaCaT cells were treated with ZnO and TiO_2 nanoparticles for 24 and 48 hours at concentrations between 0.5 and 40 $\mu g \cdot mL^{-1}$ and irradiated with UVB, it was found that ZnO and TiO_2 increased intracellular ROS levels by 2.1 and 1.8-fold, respectively. Moreover, these nanoparticles induced free radical generation in cells upon UVB irradiation. It was also found that at a nanoparticle concentration of 40 $\mu g \cdot mL^{-1}$, cell viability was reduced to 45% [46].

In general, the phototoxicity studies of TiO_2 nanoparticles show that rutile particles produce less cytotoxicity than anatase particles of similar sizes. Therefore, in order to

diminish the detrimental effects caused by the anatase phase, the scientific committee on consumer safety (SCCS, European Union) has declared that TiO_2 in sunscreens should be mainly composed of the rutile form with up to 5% anatase and coated with silica, methicone or aluminium hydroxide, in such way that the final formulation is stable [99].

The inconsistency in the reported toxic effects of TiO_2 and ZnO nanoparticles arise mainly from the use of different protocols, presence or absence of UV light, cell type and unrealistic dose or concentration exposures. Thus, a protocol which simulates realistic conditions and reports consistent results should be developed. Nevertheless, whether these materials are toxic or not, their photocatalytic activity leads to the degradation of other organic filters present in the sunscreen formulation. This results in the formation of toxic intermediates and a reduction of the SPF rating, unknowingly exposing users to higher UV levels. Thus, the photocatalytic activity of the inorganic filters should be reduced whilst conserving their UV filtering properties. Consequently, in recent years alternative metal oxides with similar UV filtering features but lower photocatalytic activity have been investigated.

2.4 Strategies to reduce the photocatalytic activity and ROS generation of TiO_2

To diminish the potential detrimental effects of TiO_2, the reduction of its photocatalytic activity is the most effective strategy since its use in sunscreen products has already been approved. Therefore, multiple strategies have been researched and some even put in place, such as the use of less reactive crystal phases or coating of these particles. Additionally, novel nanomaterials with UV filtering properties have been and are being investigated.

2.4.1 Crystal phase

The efficiency of the photocatalytic process of TiO_2 is determined by the recombination rate of the excited e^-/h^+ pair, and thus, its lifetime to undergo charge transfer to adsorbed species on the surface of TiO_2 particles. Degussa P25 has been reported to display greater photocatalytic activity compared to single-phase TiO_2 due to improved charge carrier separation. This has been proposed to occur through the trapping of electrons in the rutile phase, and the subsequent e^-/h^+ recombination inhibition results in an increased lifetime of the e^-/h^+ pair [64]. Moreover, the specific surface area of TiO_2 nanoparticles also plays

an important role in the efficiency of the photocatalytic process. Hence, anatase TiO_2 particles exhibit higher photocatalytic activity than rutile TiO_2 particles due to, generally, having higher surface area [64]. The rutile crystal phase is obtained upon heat treatment of the anatase phase [80]. This, in turn, results in particle and crystal growth, and agglomeration, resulting in reduced surface area [80]. In a recent study by Hayyan *et al.* (2016), it was found that the free radicals produced are dependent on the TiO_2 crystal phase present when O_2 is used as the e^- acceptor [28]. Particles in the rutile crystal form mainly yielded $^{\bullet}O_2^-$ for instance, whilst when the anatase phase was used, H_2O_2 was the primary product obtained. Such an outcome is the result of the higher photocatalytic activity of the anatase phase, compared to that of the rutile phase [28]. This coincides with a previous study where, a potential explanation to why the anatase phase is more active than the rutile phase, was due to the e^- in the former phase being more oxidative, enabling e^- transfer from the particles to adsorbed molecules [100]. Such oxidative nature was ascribed to a raise to higher energy levels, relative to redox potentials of adsorbed molecules, of the valence band maximum in the anatase phase [100]. As a result, TiO_2 nanoparticles with only up to 5% anatase phase are allowed to be used in commercial sunscreen products, as stated by the Scientific Committee on Consumer Safety (SCCS, European Union) [99].

2.4.2 Coating

As discussed in Section 2.2.2.2, the charge transfer by the e^-/h^+ pair takes place on the surface of TiO_2 nanoparticles; therefore, by coating the surface of these particles their photocatalytic activity can be disrupted. The coating acts as a protective layer by isolating TiO_2 from its surrounding medium, and consequently, avoiding the formation of free radicals. An appropriate coating should be stable in the final formulation and during the usage of the sunscreen product [99]. Furthermore, the coating should not interfere with the UV filtering properties of TiO_2 [99]. Coating materials, such as silica (SiO_2), aluminium oxide (alumina, Al_2O_3) and different polymers, have been studied and applied on TiO_2 [11, 48]. Another investigated coating material is aluminium hydroxide ($Al(OH)_3$). The coated particles displayed a reduction in ROS generation compared to

untreated TiO_2. Nevertheless, ions present in swimming pool water, such as Ca^{2+} and OCl^-, have been shown to interact with the coating layer and disrupt its integrity. This allows the core TiO_2 to once again form free radicals and, thus, highlights the importance of the coating stability [77].

2.5 Nanoparticles for ROS scavenging and UV filtration

Novel and safer oxides have been investigated as potential replacements of TiO_2 and ZnO nanoparticles in sunscreen formulations. Also, efforts have been made to reduce their photocatalytic activity and free radical production. Recently, the free radical scavenging behaviour of nanoparticles has been the focus of research, suggesting a novel approach to diminish oxidative stress damage. Metal oxides, such as cerium oxide (CeO_2) and yttrium oxide (Y_2O_3), have shown to be ROS scavengers and biocompatible [101, 102]. Thus, the use of these materials in conjunction with titanium dioxide could mitigate the potential adverse effects of TiO_2.

2.5.1 Cerium oxide (CeO_2)

Many studies have investigated CeO_2 nanoparticles for use in sunscreen formulations as UV blockers since this metal oxide displays similar UV filtering properties to those of TiO_2 and ZnO [103]. Cerium oxide is a semiconductor with an optical *Eg* close to that of TiO_2 (3.19 eV) [103]. Thus, it also absorbs wavelengths corresponding to the UV region [103]. Boutard *et al.* (2013) determined a noticeable increase in the *in vitro* SPF value of two emulsions containing a mixture of organic UV filters, TiO_2 and either ZnO or CeO_2 (SPF (43.4 ± 2.6) compared to SPF (48.5 ± 2.3)) by only replacing ZnO with CeO_2 at a loading of 3 wt% [55]. In a similar fashion, a higher SPF rating was obtained from sunscreen formulations containing a mixture of TiO_2 and calcium doped CeO_2 nanoparticles than those containing a mixture of TiO_2 and ZnO [104]. Hence, these studies highlight the advantages of the use of novel CeO_2 nanomaterials over TiO_2 and ZnO in UV filtering applications.

Furthermore, CeO_2 nanoparticles have shown to be excellent free radical scavengers through redox cycling of their Ce^{3+} and Ce^{4+} oxidation states, where a high Ce^{3+}/Ce^{4+} ratio favours such scavenging behaviour due to the presence of oxygen vacancies at the surface of the particle [105]. Oxygen vacancy formation increases with a decrease in

particle size; thus, the antioxidant behaviour of CeO_2 is accentuated in particles smaller than 15 nm in diameter [105, 106]. These vacancies favour the reduction of Ce^{4+} to Ce^{3+} states on the particle surface, which act as active sites and react with free radicals, which in turn, results in the aforementioned redox cycle between the 3+ and 4+ states [107, 108]. As shown by numerous *in vivo* and *in vitro* studies, this scavenging activity confers CeO_2 nanoparticles an anti-apoptotic activity due to free radical scavenging in instances of oxidative stress, and thus, aids in increasing cell viability [102].

2.5.2 Yttrium oxide (Y_2O_3)

Another metal oxide that has recently gained attention is yttrium oxide (yttria, Y_2O_3). This material has been shown to have high thermal and chemical stability, as such, it has been used to stabilise zirconia, increase the corrosion resistance of magnesium alloys and as a host for rare earth-doped lasers [109, 110]. Yttrium oxide exhibits UVC absorption properties due to its wide optical band gap of 5.8 eV which, as mentioned in Section 1.4, is a UV wavelength band absorbed by the ozone layer and does not reach the Earth's surface [75]. Additionally, Y_2O_3 nanoparticles have been studied for biomedical applications, such as photodynamic therapy and biological imaging [111]. Furthermore, as for CeO_2, this metal oxide exhibits good antioxidant behaviour due to high oxygen affinity and nonstoichiometric oxygen [112]. Thus, recent research on this material has focused on its scavenging activity to mitigate oxidative stress, and therefore, increase cell viability [101, 102].

Schubert *et al.* (2006) assessed the toxicity of CeO_2 and Y_2O_3 nanoparticles in HT22 nerve cells after 20 hours exposure [101]. Dichlorofluorescein-di-acetate, a nonfluorescent reagent, was employed to determined intracellular levels of ROS. This chemical undergoes de-acetylation and accumulates within the cells [101]. The formed product then reacts with ROS to form fluorescent dichlorofluorescein, which can then be quantified through fluorescence microscopy [101]. It was found that Y_2O_3 nanoparticles (12 nm) increased cell viability in a concentration dependent manner, from $2 - 20\ \mu g \cdot mL^{-1}$, due to direct antioxidant activity since a ~50% reduction in ROS occurred after 10, 30 and 60 minutes exposure to Y_2O_3 (Figure 2.15 (a)). In addition, cells were exposed to a source of ROS for 8 hours to cause an accumulation of free radicals and induce oxidative stress. After adding Y_2O_3 nanoparticles to the cells 15 minutes prior to the measurement of ROS, a decrease in free radicals was detected (Figure 2.15 (b)),

corroborating the previous results, suggesting that these nanoparticles act as direct antioxidants [101].

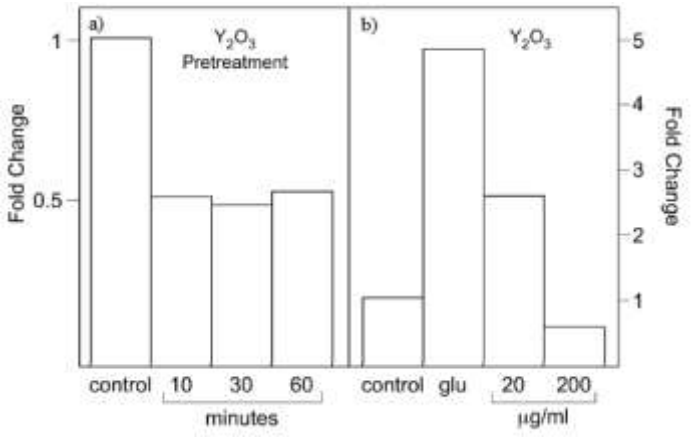

Figure 2.15: Change in ROS levels when cells were exposed to (a) 20 $\mu g \cdot mL^{-1}$ of Y_2O_3 over a period of 60 minutes and (b) glutamate for 8 hours following the addition of 20 or 200 $\mu g \cdot mL^{-1}$ of Y_2O_3. Figure adapted from Schubert *et al.* (2006) [101].

Very recently, Khaksar *et al.* [102] showed that the administration of CeO_2 and Y_2O_3 nanoparticles, on their own or in conjunction, produce an antioxidant and cell protective effect against oxidative stress and apoptosis from diazinon exposure in pancreatic rat cells. Additionally, an increase in mean body weight and reduction in blood glucose levels were observed in rats post-exposure to CeO_2 or Y_2O_3 nanoparticles and a combination of these two, compared to controls which were only exposed to diazinon [102].The ROS levels were determined from serum and pancreatic tissue; rats exposed only to diazinon showed increased free radical levels in both serum and pancreatic tissue; however, after treatment with CeO_2, Y_2O_3 nanoparticles and their combination, a noticeable decrease in ROS was seen (Figure 2.16 (a)) [102]. As previously mentioned, CeO_2 and Y_2O_3 nanoparticles can impact the cell defence processes including apoptosis, and can instead, protect cells from apoptosis. Such an effect can be appreciated in Figure 2.16 (b), where the rat control group exposed to diazinon (D) exhibited the lowest viable cell percentage (61.7%), relative to the control group (Con). However, cell viability increased to 74.8%, 82.3% and 89.3% after exposure to CeO_2, Y_2O_3 and their combination, respectively, and the percentage of early and late apoptotic cells decreased. Moreover, the nanoparticles control group, consisting of a combination of both particles, caused no apoptotic effects as all the cells remained alive. Overall, this proves that both nanomaterials act as free

radical scavengers and reduce toxicity, as evidenced by the lack of apoptotic cells [102].

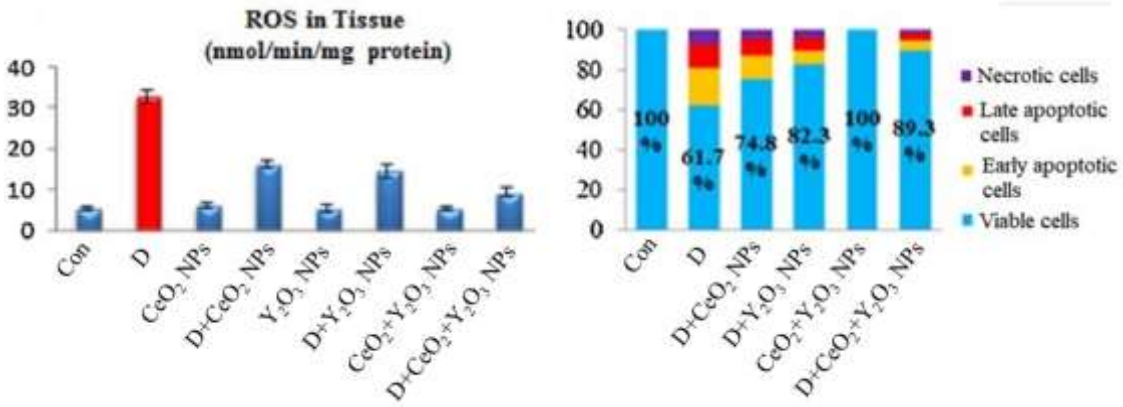

(a) (b)

Figure 2.16: (a) Protective effect of CeO_2 and Y_2O_3 nanoparticles against ROS in pancreatic tissue from diazinon exposure and (b) percentage of viable cells, apoptotic and necrotic cells upon diazinon exposure and treatment with CeO_2 and Y_2O_3 nanoparticles. Figure adapted from Khaksar *et al.* (2017) [102].

Hence, Y_2O_3 nanoparticles have been shown to scavenge free radical species and protect cells from apoptosis. Therefore, the scavenging properties of Y_2O_3 will be studied in this research thesis as part of a core-shell material (TiO_2@Y_2O_3) for reduction of ROS generated by the photocatalytic activity of P25 TiO_2. Consequently, such a reduction in free radicals is expected to reduce potential toxic effects of pristine TiO_2, whilst maintaining the UV absorption properties of P25 TiO_2.

2.6 Research objectives

Cosmetic products, such as sunscreens, contain TiO_2 and/or ZnO nanoparticles due to their good UV blocking properties. However, in recent years, concerns have been raised regarding their safety due to the generation of reactive species upon UV exposure, owing to their photocatalytic activity, and the subsequent potential toxic effect of these species. As such, the key objective of this research will be to synthesise a TiO_2 based nanoparticle system for sunscreen application with reduced photocatalytic activity but also maintaining of its UV blocking properties. Furthermore, the cytotoxicity of these particles on a human cell line pertinent to their use in sunscreen products will be assessed using *in*

vitro test methods. The outlined research objectives will be accomplished by answering the following questions:

- What methods can be used to reduce the photocatalytic activity of TiO_2, and thus, subsequent radical species produced?
- Will the designed nanoparticle system reduce the generated free radicals or scavenge them?
- Will this system interfere with the UV filtering behaviour of TiO_2?
- Will the synthesised system display higher *in vitro* biocompatibility, compared to pristine TiO_2, on a pertinent human cell line in the absence and/or presence of simulated solar radiation?

Chapter 3

Materials and Methods

3.1 Materials, chemicals and reagents

This section lists the materials, chemicals and reagents, specifications along with their suppliers, used throughout the characterisation of the nanomaterials investigated in this research.

Table 3.1: List of materials and chemicals/reagents used in this research.

Material/ Chemical/ Reagent	Specifications	Supplier
96-well plate	Flat bottom	CellStar, Greiner Bio-One, Germany
3-(4,5-dimethylthiazol-2-yl)-5-(3-carboxymethoxyphenyl)-2-(4-sulfophenyl)-2H-tetrazolium salt (MTS)	CellTiter96 ® AQ_{UEOUS} Non-Radioactive Cell Proliferation Assay	Promega Corporation
Crystal violet (tris(4-(dimethylamino)phenyl)methylium chloride, $[C(C_6H_4N(CH_3)_2)_3]Cl$)	>90%	Sigma Aldrich
Dulbecco's Modified Eagle Medium: Ham's F-12 nutrient mixture (DMEM/F12)	Phenol red	IHMRI
Dulbecco's phosphate buffered saline (DPBS - -)	Without Ca^{2+}/Mg^{2+}	GIBCO, Life Technologies, UK
Ethanol (CH_3CH_2OH)	Absolute	Chem-Supply
Fetal Bovine Serum (FBS)	-	GIBCO, Life Technologies, USA
GlutaMAX™-l (100x)	-	GIBCO, Life Technologies
HaCaT cell line	-	Borrowed from the University of Sydney
Penicillin/Streptomycin	10000 $U \cdot mL^{-1}$	GIBCO, Life Technologies
Sodium hydroxide (NaOH)	>98%	Sigma Aldrich
Ultra-Vitalux sunlamp	300 W	OSRAM
T75 cm^2 sterile tissue culture flasks	Vented	CellStar, Greiner Bio-One, Germany
Teflon liner	40 mL capacity	-
Titanium dioxide (P25 TiO_2)	Evonik AEROXIDE, Fumed Metal Oxide	Evonik Industries AG
Trypan blue	0.4%	Sigma Aldrich
Trypsin/EDTA	0.25%	GIBCO, Life Technologies
Yttrium (III) nitrate hexahydrate ($Y(NO_3)_3 \cdot 6H_2O$)	99.8%	Sigma Aldrich
Zinc oxide (ZnO)	Nanopowder, particle size < 100 nm	Sigma Aldrich

3.2 Synthesis of $TiO_2@Y_2O_3$ nanoparticles

The desired $TiO_2@Y_2O_3$ nanoparticles were synthesised by a modification of the method outlined by [113], whereby, a hydrothermal technique was employed to synthesise Y_2O_3 modified CeO_2 nanoparticles without the need of a calcination step. As such, this technique is favourable over commonly used techniques to form Y_2O_3, such as precipitation, sol-gel and combustion methods, since these processes involve the generation of impurities or a calcination step of over 800 °C [114, 115]. Such high temperatures, as mentioned in Section 2.2.2.2, will result in a change in crystal phase of anatase to rutile of TiO_2, such an outcome is undesirable and out of the line with the aims of this research [114, 116, 117]. The hydrothermal method involves the precipitation of a precursor material in an aqueous solution and further heat treatment in a pressurised vessel. The obtained product was a metal hydroxide which required further heat treatment to form the desired metal oxide, as opposed to that suggested in [113].

Figure 3.1: Schematic diagram of the procedure of the hydrothermal synthesis of $TiO_2@Y_2O_3$ nanoparticles.

Firstly, pristine Y_2O_3 nanoparticles were prepared so as to establish the conditions at which the core-shell particles should be synthesised. This synthesis involved the preparation of a 0.1 M yttrium (III) nitrate hexahydrate ($Y(NO_3)_3 \cdot 6H_2O$) solution in 10 mL DI water under continuous stirring. Next, 0.5 M sodium hydroxide (NaOH) solution was dropwise added until the pH changed to ~10. Following this, the mixture was transferred to a 40 mL Teflon-lined autoclave and kept at 150 °C in the oven for 10 hours and left to cool to room temperature. The resultant precipitate was transferred to a 50 mL centrifuge tube and washed to remove impurities, firstly, with absolute ethanol. The supernatant was discarded and the solid pellet was resuspended with DI water and centrifuged again at 7000 rpm for 30 min in a TG16-WS centrifuge (ProSciTech, Thuringowa, Australia). The remaining solid was subsequently dried at 100 °C over a

period of 10 hours in an oven. The obtained precursor was heat treated in air at 500 °C for 4 hours with a heating rate of 5 °C·min^{-1} in a tube furnace (Figure 3.1). The XRD pattern of the precursor and annealed samples (Figure 4.1 (b)) showed $Y(OH)_3$ and Y_2O_3 crystal phase, respectively. Thus, these conditions were used when synthesising the coated P25 TiO_2 (hereafter TiO_2) nanoparticles. However, instead of preparing a 0.1 M $Y(NO_3)_3 \cdot 6H_2O$ solution, 0.2 g TiO_2 were suspended in 10 mL DI water in a glass beaker under continuous stir with a magnetic bar along with a weighed amount of $Y(NO_3)_3 \cdot 6H_2O$ for a final weighting Y/Ti ratio or Y wt% of 5, 10 and 25 %. Shown in Figure 3.2 are the obtained powders of the precursor and annealed samples, visually identical.

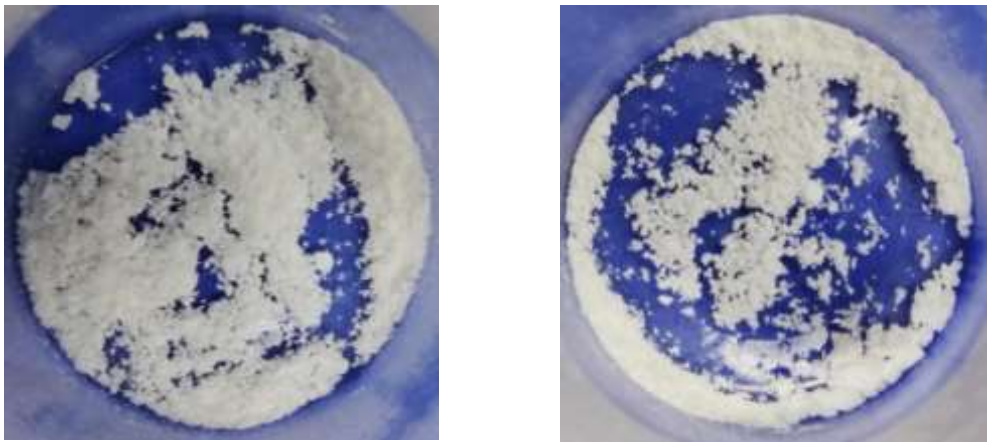

(a) (b)

Figure 3.2: Obtained (a) TiO_2@$Y(OH)_3$ and (b) TiO_2@Y_2O_3 nanopowders.

3.3 Materials characterisation

The following section focuses on the multiple characterisation techniques employed to asses and evaluate the suitability of the synthesised materials for UV filtration. The investigated properties include particle composition, morphology, size, surface area, UV absorption and photocatalytic activity.

3.3.1 X-ray Diffraction (XRD)

In order to evaluate the crystal phase and crystallinity of the materials used in this research, X-ray diffraction was employed. Crystalline structures act as diffraction gratings for monochromatic X-rays whose wavelength is similar to that of the lattice plane distance (Figure 3.3) [118].

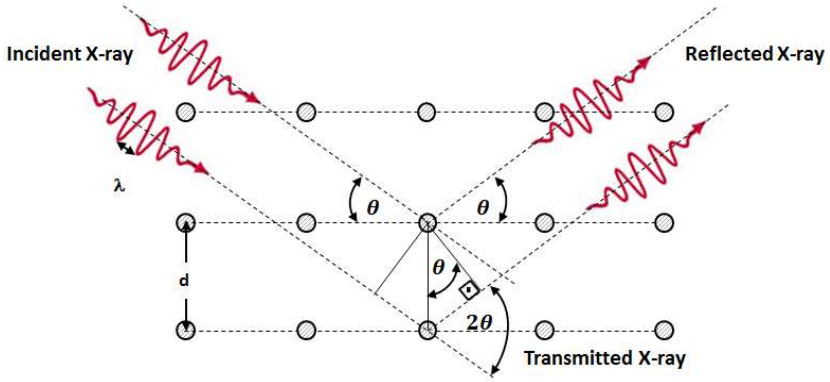

Figure 3.3: Diagram of a crystalline structure with d lattice plane spacing irradiated with X-rays. Figure reproduced from Kot (2014) [119].

The intensity of the reflected X-rays produced by constructive interference, which occurs when the Bragg law (Equation 3.1) is satisfied, is recorded by a detector and processed through software, resulting in an X-ray diffraction pattern [118]. The atomic distribution within the lattice determines said intensities; hence, the obtained XRD pattern is a fingerprint of the atomic arrangement of the investigated material [118].

$$n \lambda = 2 d \sin \theta \quad (3.1)$$

Where n is the order number, λ is the wavelength of the X-rays (nm), d is the interplanar spacing generating the diffraction (nm), and θ is the diffraction angle (rad) [118].

3.3.1.1 Experimental procedure

Sample preparation involved the crushing of a small amount of nanoparticle powder with an agate mortar and pestle into a fine powder. A small spatula was used to place the powdered sample onto a circular quartz glass substrate and mixed with a few drops of ethanol, forming a thin layer. The ethanol was allowed to evaporate prior to analysis. The XRD patterns of all the prepared samples were obtained with an Enhanced Mini-Materials Analyser (εMMA) X-Ray Diffractometer (XRD) (GBC Scientific Equipment, Melbourne, Australia). The samples were scanned between 2θ = 10 - 90°, at a scan speed of 4 °·min^{-1}, step size of 0.020° and using a CuKα (λ = 1.54059 Å) radiation source. The phases of the studied samples were identified by matching their diffraction pattern to those of a Powder Diffraction Card (PDF) using TRACES software. The mean crystallite size of the studied particles was calculated using the Scherrer equation, as per Appendix B.1.

3.3.2 Hydrodynamic particle size

Particle size and size distribution are important determining factors of a nanoparticle system since several properties relating to biocompatibility are strongly influenced by the size of the particle. These properties include the effectiveness of the photoprotection, photocytotoxicity and dermal penetration of TiO_2 and ZnO, as previously mentioned [1, 11]. A widely used technique to determine the diameter of nanoparticles in suspension is dynamic light scattering (DLS). This technique measures the changes in the scattering intensity originated from laser illumination of a nanoparticle suspension due to Brownian motion [120]. By using the Stokes-Einstein equation (Equation 3.2) the nanoparticle hydrodynamic diameter (d_{DLS}) (m) can be calculated from the translational diffusion coefficient (D) ($m^2 \cdot s^{-1}$):

$$d_{DLS} = \frac{k_B T}{3 \pi \eta D} \tag{3.2}$$

where k_B is the Boltzmann constant (1.38×10^{-23} $kg \cdot m^2 \cdot s^{-2} \cdot K^{-1}$), T is the temperature (K) and η is the dynamic viscosity of the suspending medium ($kg \cdot m^{-1} \cdot s^{-1}$) [120].

3.3.2.1 Experimental procedure

The size distribution of the particles used in this research was measured with a Zetasizer APS particle analyser (Malvern Instruments, Worcestershire, United Kingdom). Two nanoparticle solutions of varying concentration were used. Nanoparticle stock suspensions of 500 $mg \cdot L^{-1}$ in DMEM/F12 media were prepared on the experiment day, sonicated for 1 hour using a Branson 1800 ultrasonic bath (Branson Ultrasonics, Danbury, CT, USA), diluted 10-fold and analysed. The new 50 $mg \cdot L^{-1}$ solutions were sonicated for 10 minutes prior to their measurement. The size distribution measurements were performed using 100 µL aliquots of each concentration in a flat bottom 96-well plate.

3.3.3 Specific surface area

The surface area of materials can be used as an indicator of their reactivity. Nanomaterials are characterised by high surface areas, and thus, high reactivity, which could potentially cause cytotoxicity on living organisms and the environment [97]. The Brunauer-Emmett-Teller (BET) method is employed to determine the specific surface area of nanoparticles.

This method assumes that gas adsorption on a solid surface occurs in a close-packed multilayer state through which the volume of adsorbed gas can be used to determine the specific surface area (Equations 3.3 and 3.4) [121, 122].

$$\frac{1}{v\left(\frac{p_0}{p}-1\right)} = \frac{1}{v_m c} + \frac{c-1}{v_m c}\frac{p}{p_0} \tag{3.3}$$

$$S_{BET} = \frac{v_m N A_{CS}}{V a} \tag{3.4}$$

Where p and p_0 are the equilibrium and gas saturation pressure (Pa), respectively, v is the volume of gas adsorbed at pressure p (m^3), v_m is the volume of gas constituting an adsorbed monolayer (m^3) and c is the BET constant [121]. The specific surface area, S_{BET} ($m^2 \cdot g^{-1}$), is defined by v_m, Avogadro's number (N, 6.022×10^{23} mol^{-1}), the adsorbate cross sectional area (A_{CS}, m^2), the molar volume of the adsorbate gas (V, $m^3 \cdot mol^{-1}$), and the weight of the studied solid (a, g) [121].

3.3.3.1 Experimental procedure

The surface area of all the particles was investigated using a TriStar II (Micromeritics Instrument Corp., Norcross, GA, USA) surface area and porosity analyser. Sample preparation consisted of weighing a small amount (< 100 mg) of powder samples into a glass sample tube, which was then placed in a VacPrep™ 061 (Micromeritics Instrument Corp., Norcross, GA, USA) and degassed under vacuum overnight at 120 °C to remove any atmospheric adsorbed contaminants (water vapor and gas) from the surface of the particles. The tubes were then placed in the TriStar II analyser and multipoint BET surface area measurements were performed using nitrogen, N_2, gas as the adsorbate which has a cross sectional area of 0.162 nm^2 at 77 K [123].

3.3.4 Electron microscopy

The morphology of the synthesised particles was investigated through electron microscopy. Electron microscopy is an imaging technique based on the bombardment of a sample with an electron beam as illumination source [124]. The electron-matter interaction results in the emission of multiple signals, as highlighted in Figure 3.4, which are then recorded by a detector and an image is then reproduced.

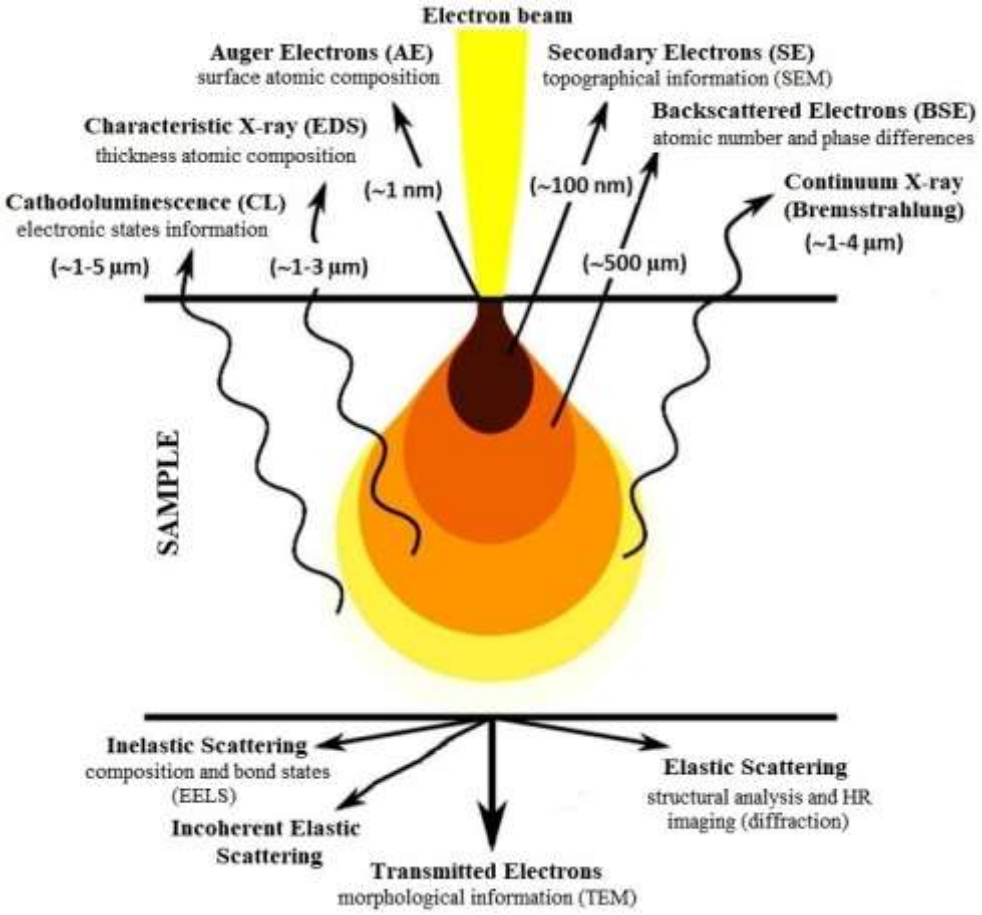

Figure 3.4: Signals generated due to electron-mater interaction volume. Figure reproduced from Chauhan (2018) [125].

The multiple electron microscopy techniques differ in the recorded signals used to image the sample, and thus, obtain different information regarding the investigated specimen, such as its topography and composition. For example, in scanning electron microscopy (SEM) an image of the sample surface is produced from the detection of scattered electrons, either secondary or backscattered, whereas scanning transmission electron microscopy (STEM) produces an image from elastically scattered transmitted electrons [124]. Electron microscope instruments can be equipped to perform energy-dispersive X-ray spectroscopy (EDS) [126]. Such a technique enables compositional elemental analysis of specific regions of the sample through the detection of emitted X-rays intrinsic to the sample [124]. The imaging methods employed in this thesis include SEM, STEM and EDS, and their experimental procedures are outlined below.

3.3.4.1 Scanning Electron Microscopy (SEM)

Scanning electron microscopy (SEM) was used to learn about the size distribution and shape of the prepared samples. A small amount of powder was placed on a piece of double-sided carbon tape. Micrographs of these particles were obtained using a JSM-7500FA cold Field Emission Gun Scanning Electron Microscopy (FEGSEM) (JEOL, Tokyo, Japan).

3.3.4.2 Scanning Transmission Electron Microscopy (STEM)

The morphology, atomic distribution and size of the nanoparticles mentioned in Section 3.1 were studied using a JEM-ARM200F STEM (JEOL, Tokyo, Japan) (Figure 3.5). Small amounts of sample were suspended in ethanol and sonicated for 1 hour until a homogeneous mixture was obtained, of which two drops were placed onto a lacey 200 mesh carbon coated copper TEM grid and allowed to dry prior to analysis. The particle size distribution of each sample was obtained using ImageJ software on the corresponding micrographs and then plotted.

Figure 3.5: JEOL JEM-ARM200F Cs Corrected S/TEM [127].

3.3.4.3 Energy-dispersive X-ray Spectroscopy (EDS)

Energy-dispersive X-ray spectroscopy (EDS) was used to determine the presence of any contamination generated during synthesis or handling of the nanoparticles used in this work, as well as to determine the coating wt% of the synthesised particles. High resolution EDS mapping was performed using a JEM-ARM200F cold FEGSEM (JEOL, Tokyo,

Japan) and a 100 mm^2 detection area JEOL Centurio SDD detector. Sample preparation consisted in the procedure described in Section 3.2.4.1. An accelerating voltage of 200 kV and spatial resolution of 0.1 nm were utilised during analysis. NSS ARM EDS software was used to collect the EDS mapping images of the selected lacey mesh regions.

3.3.5 Ultraviolet-Visible spectroscopy

In order to determine the UV absorption efficiency of the synthesised particles and their band gap, UV-vis spectroscopy was used. These particles are semiconductors which, as mentioned before, reflect, scatter and absorb UV photons with energy greater than their band gap through the promotion of an electron from the valence band to the conduction band [13]. The energy of the incoming photons, hν, can be calculated using the following equation:

$$E_{photon} = h\nu = \frac{1240\ (eV \cdot nm)}{\lambda\ (nm)} \tag{3.5}$$

where λ is the wavelength of the photon. The band gap of a semiconductor can be calculated using the following expression:

$$(\alpha h\nu) = B(h\nu - Eg)^n \tag{3.6}$$

where α is the optical absorption coefficient (cm^{-1}) proportional to the absorbance of the samples, hν is the energy of the photon, B is a constant, and *Eg* (eV) is the band gap energy. The type of electronic transition determines the value of n. Direct and indirect transitions are represented by n = ½ and 2, respectively [128-130]. In this case n = ½ for a direct allowed transition was used [128-130]. By plotting $(\alpha h\nu)^n$ as a function of hν, a Tauc plot is constructed (Appendix D.2). The extrapolation of the linear fragment of the Tauc plot with the x-axis (hν) indicates the band gap of the investigated sample (Figure 3.6) [25].

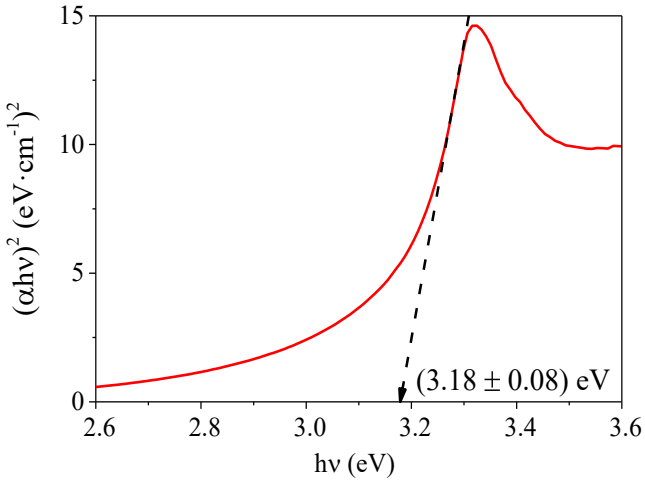

Figure 3.6: Tauc plot constructed from the UV-vis absorption spectrum of ZnO nanoparticles suspended in ethanol.

3.3.5.1 Experimental procedure

Suspensions of ~25 mg·L^{-1} of nanoparticles in absolute ethanol were freshly prepared on the experiment day. Such solutions were sonicated for 1 hour prior to their absorbance measurement between 200 and 800 nm using a UV-1800 Spectrophotometer (Shimadzu, Kyoto, Japan) and 1.4 mL quartz cuvettes with 1 cm path length. The scan speed and scan mode were set to medium and single, respectively, with a sampling interval of 1.0 nm.

Photocatalytic activity

Semiconductor nanoparticles, such as ZnO and TiO_2, are used to purify waste water through the degradation of organic pollutants [75, 131]. As mentioned in Section 2.2.2.2, upon irradiation of energy equal to or higher than the band gap of these particles, charge separation (e^-/h^+) and subsequent generation of free radicals takes place [131]. These highly active species, such as $^{\bullet}OH$ and $^{\bullet}O_2^-$, react with organic molecules and decompose them [83]. Thus, through the degradation of an organic dye, for instance crystal violet, the photocatalytic activity of nanoparticles can be assessed [131, 132]. Hydroxyl radicals attack the electron rich -C=C- bond of crystal violet, rendering the dye colourless (Figure 3.7) [132]. Hence, the change in maximum absorbance (590 nm) of the dye is proportional to the amount of $^{\bullet}OH$ generated [132].

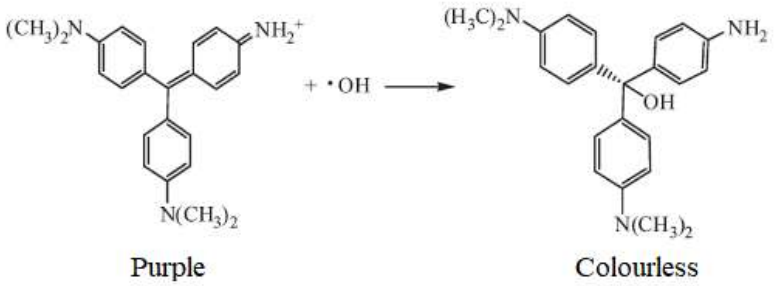

Figure 3.7: Degradation of crystal violet due to •OH radicals. Figure reproduced from Xue *et al.* (2011) [132].

3.3.5.2 Experimental procedure

The photocatalytic activity of the investigated/tested nanoparticles in this research was assessed through the degradation of crystal violet. Two light sources, UVA/UVB and simulated solar radiation, were employed as irradiation sources to induce free-radical generation by the tested particles, and thus, dye degradation.

UVA/UVB radiation

The acute photocatalytic effects of the examined particles were assessed with a RPR-200 photochemical reactor (Rayonet, Brandford, CT, USA) equipped UV phosphor-coated lamps (350 nm and 300 nm). Firstly, a stock solution of dye (c = 1305 $mg \cdot L^{-1}$) was prepared in a 100 mL volumetric flask covered with aluminium foil and kept in the dark in a dry cabinet. The photocatalyst nanoparticles stock solutions (c = 1000 $mg \cdot L^{-1}$) were prepared freshly on the experiment day and sonicated for 1 hour prior to their addition (0.50 mL) to 0.38 mL of dye stock solution into a 100 mL volumetric flask, which was then filled to the mark with DI water and mixed thoroughly. The mixture was then transferred to a quartz beaker and stirred in the dark with a magnetic bar for 30 min in the UV reactor with a constant nitrogen flow bar as to avoid sedimentation of the tested particles. A 10 mL aliquot was collected into a 15 mL centrifuge tube covered with aluminium foil (t = 0 min) followed by UV irradiation over a period of 30 min, where 10 mL aliquots were collected every 5 min (Figure 3.8).

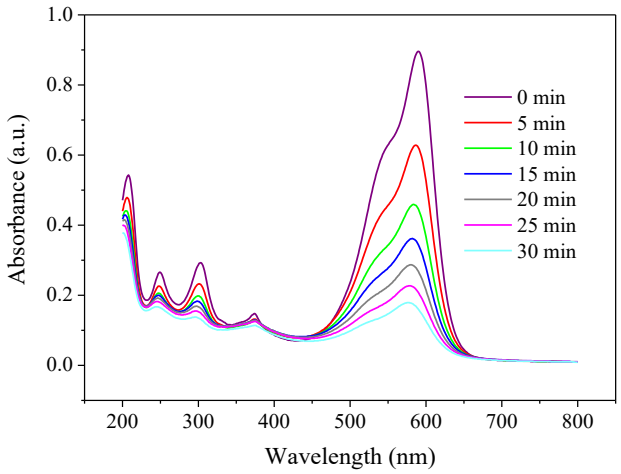

Figure 3.8: UV-vis absorption degradation curves of crystal violet suspended in DI water with TiO_2 nanoparticles.

Simulated solar radiation

Irradiation of the examined particles with simulated solar radiation allows for a better representation of real-life conditions, for instance, the application of sunscreen formulations containing these particles during outdoor activities. In this case, the sample was transferred to a PMMA glass vessel under continuous stirring and irradiated for 5 hours, where the absorbance was measured every hour. A halogen lamp (50 watts) and an illumination intensity of AM 1.5G one sun (100 $mW \cdot cm^{-2}$) were employed (Figure 3.9) [133].

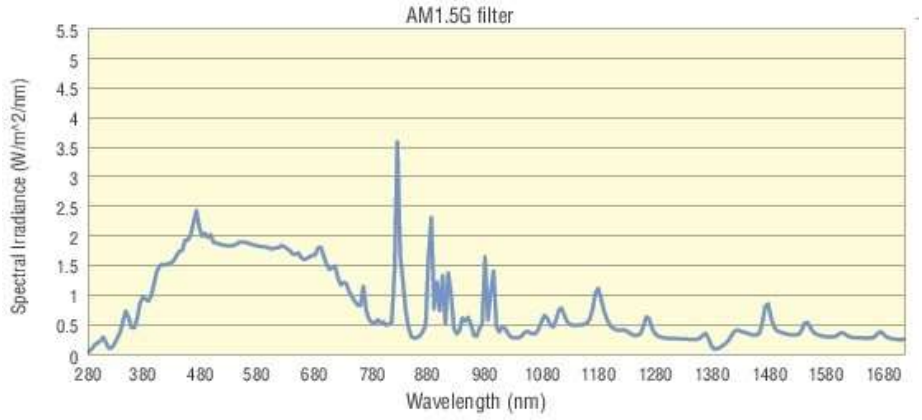

Figure 3.9: Light emission profile of the halogen lamp filtered with AM 1.5G one sun employed to create simulated solar radiation for a better representation of the photocatalytic activity of the studied particles in this thesis work under real-life conditions.

For both approaches, the absorbance measurement at 590 nm of each aliquot was carried out using a UV-1800 Spectrophotometer (Shimadzu, Kyoto, Japan), as outlined in Section 3.2.5.1. In order to assess the photocatalytic activity of the particles used in this research, the Langmuir-Hinshelwood model was used. The Langmuir-Hinshelwood (L-H) model is used to describe the photocatalytic oxidation of organic compounds, such as crystal violet, by means of the following equations [134, 135]:

$$r_{L\text{-}H} = \frac{dC}{dt} = \frac{kK_{ad}C}{1 + K_{ad}C_0} \tag{3.7}$$

where $r_{L\text{-}H}$ is the oxidation rate ($mg \cdot L^{-1} \cdot min^{-1}$) of crystal violet, C the concentration of crystal violet, t the irradiation time (min), k the reaction rate constant ($mg \cdot L^{-1} \cdot min^{-1}$) and K_{ad} the adsorption coefficient. Integrating Equation 3.7 for small C_0 (in the order of mM), the L-H expression is given as the following pseudo first-order rate equation [134, 135]:

$$\ln \frac{C_{cv}}{C_0} = -K_{ad}kt = -k_{app}t \tag{3.8}$$

thus, the slope obtained from plotting $-\ln (C/C_0)$ against t corresponds to the apparent rate constant, k_{app}, for the photodegradation of crystal violet in the presence of the tested nanoparticles (Appendix E.1).

3.4 Biological system characterisation

3.4.1 Cell line

The main organ exposed to nanoparticles present in sunscreen products is the skin. Therefore, the cell line used in this research was a spontaneously transformed aneuploid immortal human skin keratinocyte cell line, HaCaT cell line, as to obtain more representative data related to human exposure [136]. Such a cell line is obtained from adult human epidermis, the outermost layer of the skin. Furthermore, this cell line is immortal, which means it can be subcultured for longer periods of time than regular cell lines before dying out and without loss of properties.

3.4.2 Culture conditions

The aim of cell culturing is to preserve and nourish human (or animal) cells outside of their biological environment or host by regularly removing waste produced during incubation and nourishing the cells with culture media. Additionally, the incubation conditions should maintain the correct temperature, moisture, and CO_2 levels essential for normal cell survival.

The culture medium used to grow and preserve HaCaT cells in vented T75 cm^2 sterile tissue culture flasks was modified from previous studies [21, 137] and contained phenol red DMEM/F12 supplemented with 1% (v/v) GlutaMAX^{TM}-l (100x), 1% (v/v) Penicillin/Streptomycin and 10% (v/v) heat inactivated FBS. Cell cultures in T75 flasks were kept at 37 °C in a humidified 5% CO_2 incubator.

3.4.3 Cell subculturing

Cells were subcultured, and/or transferred to a new flask with fresh media, once ~90% confluency was reached in order to provide the cells with the necessary nutrients required for a healthy growth. Prior to subculturing, each cell culture in a T75 flask was visually examined under the microscope to control cell culture condition and look for signs of contamination. If no contamination was found, then the subculturing process was carried out. This process involved the following steps:

1. The culture media in the T75 flask was decanted and the confluent cell layer was washed with 3 mL of DPBS three times.
2. Then, 3 mL 0.25% trypsin/EDTA was added to the cell flask, which was then put in the incubator at 37 °C with 5% CO_2 for 3-5 minutes in order to enzymatically dissociate the cell monolayer formed in the T75 flask without damaging the cell membrane.
3. Culture media (5-10 mL) was added to the flask to stop the enzymatic activity and the flask was shaken to detach the cells from the T75 flask.
4. This solution containing culture media, trypsin/EDTA and suspended cells was transferred to a 50 mL centrifuge tube and centrifuged at 1200 rpm (300×g) for 5 minutes at 22 °C.
5. The resulting supernatant was decanted and the remaining pellet of cells was resuspended by pipetting in-and-out fresh culture media (7 mL).

6. Cell number, and hence, the volume of resuspended cells and fresh culture media added to a new T75 flask, was calculated. Finally, the new cell culture flask was kept in the humidified incubator for the necessary period of time to reach ~90% confluency.

3.4.4 Cell counting

Cell number was determined by mixing an equal volume of resuspended cells (Section 3.4.3) with an equal volume of trypan blue. This mixture was then placed onto a Neubauer hemocytometer containing two gridded counting chambers consisting of sixteen 1 mm^2 squares and thus a defined volume of 0.1 mm^3 or 0.0001 mL. Cell counting was performed in both chambers under a light microscope and the average number counted was then used to determine the cell concentration following Equation 3.9 [137].

$$\text{Cell concentration (cells}\cdot\text{mL}^{-1}) = \text{Average cell count} \times 2 \times 10^4 \qquad (3.9)$$

3.4.5 Cell density optimisation

Prior to each *in vitro* assay the optimal cell density or cell concentration yielding a spectroscopic absorbance of approximately 1 a.u., was determined according to the procedure described below.

1. Confluent cells were enzymatically detached from the T75 flask and resuspended in culture media, following Section 3.3.4, and the cell number was determined as per Section 3.3.5.
2. Serial dilutions of cells were prepared in a flat bottom 96-well plate by transferring 100 µL of media into columns 3 - 12 in four replicates, followed by the addition of 100 µL of cells into the 3rd column in four replicates, pipetting in-and-out the mixture and transferring 100 µL to the next column. At the end, 100 µL of mixture were discarded (Figure 3.10).
3. For each cell optimisation a background consisting of 100 µL of culture media was set up indicating IC_{100} (inhibitory concentration 100%) (Figure 3.10).
4. The plates were placed in the humidified incubator for 48 hours, and 20 µL of MTS reagent were added to each well 4 hours prior to its absorbance measurement using a SpectroStar Nano (BMG LabTech, Victoria, Australia) spectrophotometer.

5. From this data, a linear relationship between cell concentration and absorbance was obtained. Each incubation period experiment was carried out three times and cell optimisation was calculated from the average of those three experiments. The determined optimal cell density for 48 hours cell seeding was $(7.2 \pm 1.2)\times10^{3}$ cells·well^{-1}. Cell density optimisation plots can be found in Appendix F.

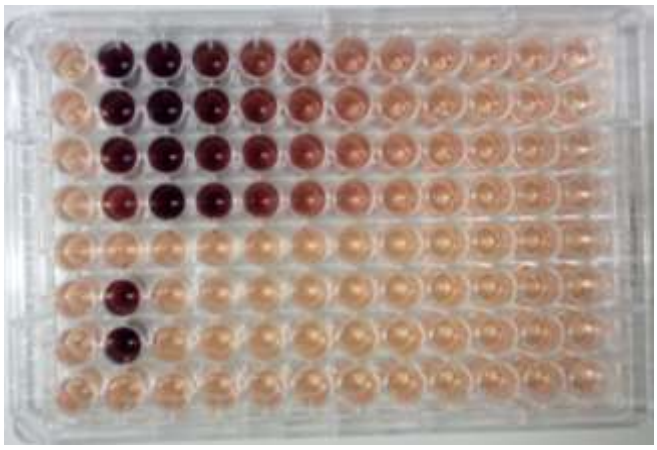

Figure 3.10: Brown formazan product metabolised by viable cells during a cell density optimisation assay. Darker and lighter regions indicate higher and lower number of metabolically active cells, respectively.

3.5 *In vitro* cytotoxicity assessment

In vitro toxicity assays assess cytotoxicity or cell death, cell viability and/or apoptosis. The quantification of changes in absorbance or fluorescence (spectrophotometric and spectrofluorometric assays) as the result of biochemical reactions, are the basis of these assays [138, 139]. Cytotoxic assays are differentiated by the biological endpoint measured. For example, the NRU (neutral red uptake) assay measures cell viability via assessing cellular lysosome integrity; the KB (kenacid blue) assay measures protein content and proliferation. In this thesis, the MTS tetrazolium salt assay, which measures mitochondrial activity, cell proliferation and/or cytotoxicity, will be used to assess the toxicity of inorganic UV filters present in sunscreens [140]. The MTS tetrazolium salt assay is an extensively used coluorimetric test in cytotoxicity due to its simple protocol. Moreover, it is not required to: wash nor harvest the cells, to transfer the sample to another well plate nor to use volatile organic solvents as with MTT methodologies [140]. The aforementioned MTS tetrazolium salt assay measures mitochondrial activity, cell

viability and cytotoxicity by the reduction of the tetrazolium salt to a soluble brown formazan product in culture media. The scheme of the reduction of MTS reagent to formazan by metabolically active cells is presented in Figure 3.11 [140]. The reduction of the MTS reagent to formazan is accomplished by NADPH or NADH generated by dehydrogenase enzymes in metabolically active cells [139, 140]. The formazan product is quantified by absorbance reading at 490 nm, which is illustrative of cell viability in culture media by plotting a dose/concentration-response curve. Thus, this assay can also be used to assess cell proliferation and cytotoxicity [139-141].

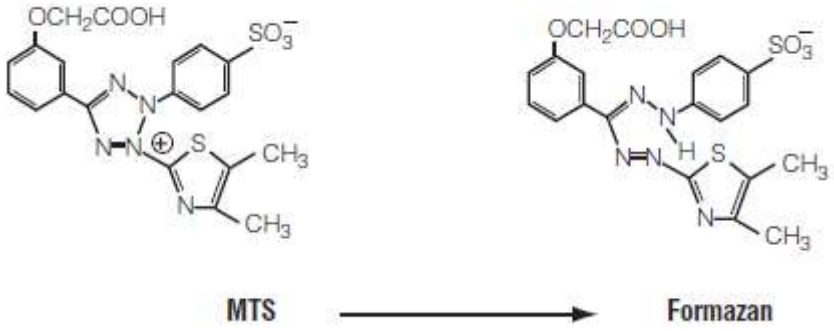

Figure 3.11: Conversion of MTS reagent to formazan. Figure reproduced from Promega technical bulletin [140].

3.5.1 The dose-response relationship

A dose-response curve indicates the toxicity of chemicals, and thus, safe levels of chemical exposure can be determined [142]. This curve is obtained by measuring the cumulative response between a subject treated with a chemical and its dose. Therefore, a dose-response curve is a measure of the toxicity of the chemical, resulting in a sigmoidal curve (Figure 3.12) [137, 142]. Several concentration values or toxicity endpoints can be determined from a dose-response relationship which can be used for regulatory toxicity evaluations [1, 137, 142]:

1. **NOAEC, NOEC** or **threshold** [No-Observed-(Adverse)-Effect Concentration] is the highest concentration at which no effects are observed.
2. **IC_{50}** (Inhibitory Concentration 50%) is the concentration at which the tested chemical produces 50% inhibition of cellular viability.

3. **TLC** (Total Lethal Concentration) is the concentration at which all cells activities are inhibited.

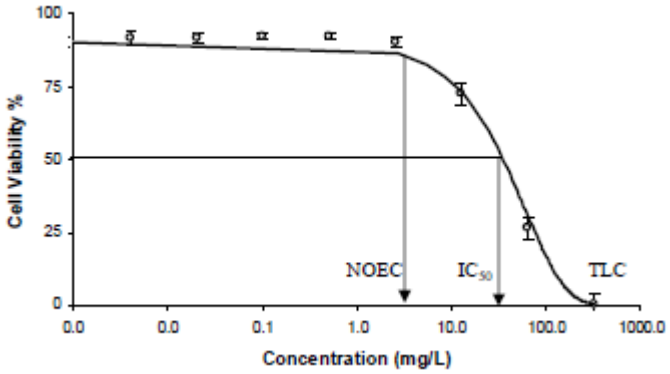

Figure 3.12: An example of a dose-response relationship *in vitro*. As the dose increases, the cell viability is reduced. Figure adapted from Bakand (2006) [137].

3.5.2 Cytotoxicity in the absence of simulated solar radiation

Following cell subculturing, the remaining resuspended cells (Section 3.4.3) were diluted in order to achieve the desired cell number in the 96-well plate, according to cell optimisation results (Appendix F), and incubated in a humidified incubator for 24 hours prior to the addition of the nanoparticles to be tested. The stock nanoparticle solutions were prepared by suspending the required amount of test particles in culture media. All nanoparticle samples were weighed with an analytical balance into a glass sample tube to obtain a stock concentration of 1000 $mg \cdot L^{-1}$ in supplemented culture media. Prior to the addition of media, the nanoparticles were sterilised to reduce any possible contamination to the cell culture by exposing the sample tubes to UVC in a Biosafety cabinet for 20 min. Two and a half hours before the addition of nanoparticles to the assay plate, the appropriate media volume was added to the sample tubes and sonicated for 2 hours in a Branson 1800 ultrasonic bath (Branson Ultrasonics, Danbury, CT, USA). The method by which the nanoparticles were added to the 96-well plate is outlined in Table 3.2 for 24 hour assays. Firstly, the volume of nanoparticles to be added to the plate was removed from the desired wells. Then, the 1000 $mg \cdot L^{-1}$ stock nanoparticle solution was diluted 1:10 and 1:100 to yield a 100 $mg \cdot L^{-1}$ and 10 $mg \cdot L^{-1}$ solution, respectively. Thirdly, the right volume of nanoparticles was added to each well after being shaken with a spin vortex in order to resuspend the particles. For each assay, two internal controls were set up indicating IC_{100} and IC_0 consisting of media and cells only, respectively, in addition to a

background consisting of media and the appropriate concentration of nanoparticles. Finally, the 96-well plate was put back into the incubator for 20 hours before 20 μL of MTS reagent were added and incubated for another 4 hours to let the formazan product be generated.

Table 3.2: Tabulated representation of the method followed for the addition of the nanoparticles to the 24 hours incubated plate.

	NP stock solution used ($mg \cdot L^{-1}$)							
	1000			100		10		
Column	3	4	5	6	7	8	9	10
Vol. media removed (μL)	50	20	10	50	25	50	25	10
Vol. NPs added (μL)	50	20	10	50	25	50	25	10
NP conc. in each well ($mg \cdot L^{-1}$)	500	200	100	50	25	5.0	2.5	1.0

Each absorbance measurement was performed three times and from the average of these, a concentration-response curve was plotted. The cell viability was calculated by the ratio of the absorbance of the treated and control wells, following Equation 3.10, and then plotted.

$$\text{Cell viability} = \left(\frac{\text{Mean absorbance of (treated cells - background)}}{\text{Mean absorbance of } (IC_0 - IC_{100})}\right) \qquad (3.10)$$

3.5.3 Cytotoxicity in the presence of simulated solar radiation

Cytotoxicity of cells treated with nanoparticles was investigated in the presence of simulated solar radiation as to obtain better representative data for the application of the examined material in sunscreen products.

3.5.3.1 Chamber set up

The set up employed to irradiate the cells treated with nanoparticles with simulated solar radiation consisted in the chamber shown in Figure G.1. This chamber was designed to accommodate the sunlamp (300 W Ultra-Vitalux, OSRAM) used to simulate solar radiation and a fan. The fan was used to remove part of the heat emitted by the lamp as to maintain temperatures close to ambient ones. Additionally, the 96-well plates were placed on an ice pack to also aid in maintaining an adequate temperature when irradiating the treated cells.

3.5.3.2 Lamp intensity distribution

In order to examine the homogeneity of the lamp across a 96-well plate, and thus, determine the working wells, the intensity distribution of the sunlamp whose light emission profile is shown in Figure 3.13, was assessed by the degradation of crystal violet due to TiO_2. Crystal violet was dissolved in DPBS and added to a 96-well plate along with 2 hour sonicated TiO_2 nanoparticle solutions in DPBS, at a concentration of 500 $mg \cdot L^{-1}$ so as to ensure noticeable and assessable dye degradation. The lamp was pre-ran for 2 hours to allow the output to stabilise then, the 96-well plate was placed on an ice pack under the lamp for 15 min at the chosen intensity of approximately 6 $mW \cdot cm^{-2}$, as measured by a UVA/B meter (model 850009, Sper Scientific). Then, the absorbance of the dye was measured and an intensity map across the exposed 96-well plate was determined with a 'colour scale' format in Microsoft Excel.

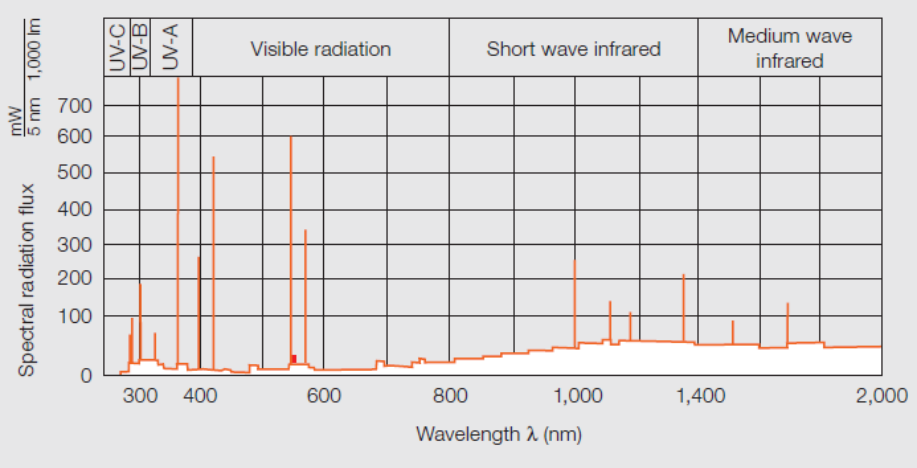

Figure 3.13: Light emission profile of OSRAM Ultra-Vitalux 300 W Sunlamp. Figure reproduced from [143].

3.5.3.3 Experimental plate set up

The cytotoxicity of TiO_2 based nanoparticles was assessed under simulated solar radiation at approximately 6 $mW \cdot cm^{-2}$ for 5 and 15 minutes. These exposures are equivalent to approximately 2 and 7 minutes in Darwin (Australia), where the highest sun intensity is recorded over the months of summer, which is double of that in European cities, such as Paris (France) [144]. First of all, a new cell optimisation was performed as radiation alone resulted in cell death. Such optimisation was performed as described in Section 3.4.5 concurrently for both exposure times, using the determined working wells from the previous Section. Next, cells were seeded in a 96-well plate as described in Section 3.4.5 for 24 hours prior to the addition of nanoparticles. For every experiment, three plates were used, an 'incubator control' (unexposed plate) and a 5 and 15min exposed plates. The 'incubator control' plate consisted of one column containing 3 replicates of IC_0 and IC_{100}. The 15 and 5min exposed plates were replicates comprising IC's and nanoparticle treated cells. The three tested nanoparticle samples were tested simultaneously at single concentrations of 25, 50 or 100 $mg \cdot L^{-1}$. Unlike in Section 3.5.2, nanoparticles were diluted in DPBS to avoid absorbance and interference from the media components (Figure 3.14) when exposing the plates to simulated solar radiation. The nanoparticles were allowed to settle for approximately 1 hour before exposure. Control cells were treated the same way, and thus, media was replaced with DPBS for 1 hour and the same amount of simulated solar exposure time. After simulated solar exposure, DPBS was replaced with media and the plates were incubated for 20 hours before MTS addition, as described in Section 3.5.2. Cell viability (%) was calculated following Equation 3.10, where the 'incubator control' plate was used as the control of the exposed plates.

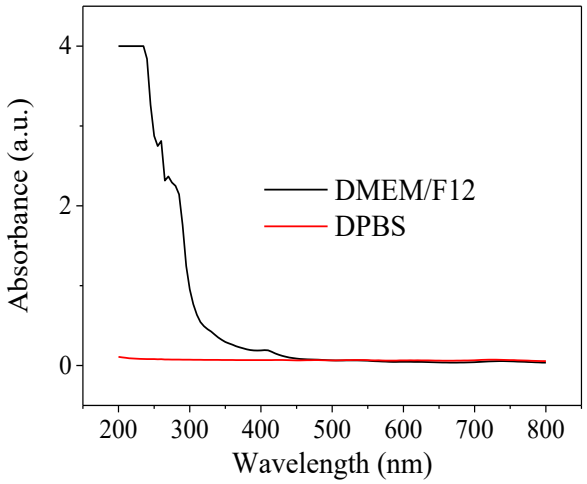

Figure 3.14: UV-vis spectra of phenol red free supplemented DMEM/F12 media and DPBS.

3.5.4 Data analysis

3.5.4.1 Cytotoxicity endpoints

The calculated cell viability values were plotted against their respective nanoparticle concentration, resulting in dose/concentration-response curves. From these curves, the NOAEC, IC_{50} and TLC endpoints (Section 3.4.1) were determined when possible. The NOAEC values were determined by extrapolating the end of the plateau in the dose-response curve. The IC_{50} values were calculated by fitting the plotted concentration-response curves to a sigmoidal curve, when possible.

3.5.4.2 Statistical analysis

Data were expressed as mean ± standard deviation (SD) from three independent experiments in order to demonstrate the reproducibility of the results. One-way analysis of variance (ANOVA) followed by Tukey's post-hoc test was used to establish the significance of the calculated data, where a value was considered statistically significant when $p < 0.05$, with p being the probability.

Chapter 4

Results and Discussion

4.1 Structural, elemental and physical characterisation

The XRD patterns of pristine and annealed (at 500 °C for 4 hours in air) TiO_2 (Figure 4.1 (a)) display sharp diffraction peaks at 25° and 48° which correspond to the (101) and (200) anatase crystal phase planes, respectively (JCPDS Card No. 03-065-5714). In the same patterns, strong diffraction peaks at 27° and 36° corresponded to the (110) and (101) rutile phase planes, respectively (JCPDS Card No. 03-065-1119), as is expected for mixed-phase P25 TiO_2. No significant difference can be seen between both patterns suggesting no anatase-to-rutile phase transformation at the employed calcination conditions occurred. The onset anatase-to-rutile phase transition temperature has been reported to vary between 400 and 1200 °C; nevertheless, most studies on this topic have stated an irreversible phase transition to rutile at an onset temperature of 600 °C [64, 145]. Thus, the obtained results are in agreement with previous studies where the reported crystal phase transformation temperature is above the 500 °C used here.

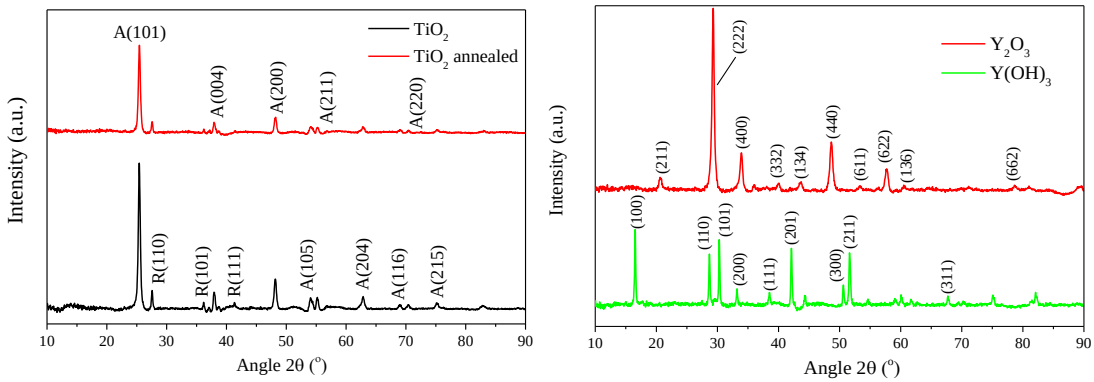

(a) (b)

Figure 4.1: X-ray diffraction pattern of (a) commercial and annealed TiO_2 at 500 °C for 4 hours in air and (b) synthesised $Y(OH)_3$ and Y_2O_3 particles.

As shown in Figure 4.1 (b), a highly crystalline $Y(OH)_3$ precursor (JCPDS Card No. 01-074-1705) and Y_2O_3 (JCPDS Card No. 03-065-3178) were obtained by the hydrothermal synthesis method described in Section 3.1.1. This revealed that to synthesise Y_2O_3, high annealing temperatures were not required, as opposed to that reported in the literature where temperatures from 600 °C up to 1000 °C are used [114, 116, 117, 146, 147]. Such high temperatures would have been not ideal for the composite particles containing mixed-phase TiO_2, as they would have caused the transformation of anatase-to-rutile TiO_2 phase (Section 2.2.2.2).

Highlighted in Figure 4.2 are the XRD patterns of the synthesised composite particles before annealing (precursors, TiO_2@$Y(OH)_3$) (Figure 4.2 (a)) and the annealed samples (TiO_2@Y_2O_3) (Figure 4.2 (b)). Diffraction peaks associated with $Y(OH)_3$ phase were not observed in the 5 wt% sample; nevertheless, broad peaks located at 15°, corresponding to the (100) $Y(OH)_3$ crystal plane, can be observed with increasing the $Y(OH)_3$ content. The broadness of these $Y(OH)_3$ peaks indicate the poor crystallinity of the samples. Contrarily, only annealed 25 wt% samples exhibited peaks low in intensity at 29°, corresponding to the (222) Y_2O_3 crystal plane. This suggests that the Y_2O_3 amount on the 5 and 10 wt% samples was too small to be detected. The appearance of these diffraction peaks is directly related to the increased $Y(NO_3)_3$ content during synthesis, resulting in a higher amount of $Y(OH)_3$ and Y_2O_3 formed.

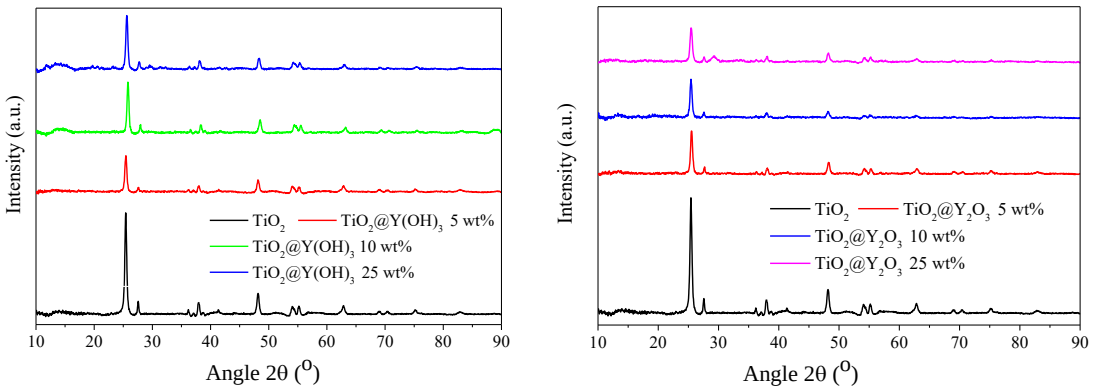

(b) (b)

Figure 4.2: X-ray diffraction pattern of TiO_2 and (a) prepared TiO_2@$Y(OH)_3$ precursor at 5, 10 and 25 wt% and (b) synthesised TiO_2@Y_2O_3 5, 10 and 25 wt% by annealing of their respective precursors.

The mean crystallite grain size of these samples was calculated using the Scherrer equation (Equation B.1). A reduction in grain size was observed for the synthesised TiO_2@$Y(OH)_3$ and TiO_2@Y_2O_3 particles (Table 4.1), compared to pristine TiO_2 ((34.9 ± 0.3) nm). Such a reduction has been previously reported during the hydrothermal synthesis of silica-modified TiO_2 nanoparticles[148]. It was found that the presence of silica supressed the formation of the rutile phase in addition to the growth of TiO_2 crystals even at 1000 °C [148]. In a similar fashion, the conservation of the anatase phase can be due to the presence of Ti-O-Y bonds at the surface of TiO_2 which could inhibit the crystal phase transition. Such an effect is confirmed by the reduction in crystallite size occurring during hydrothermal synthesis (TiO_2@$Y(OH)_3$) and further reduction after sintering of the precursor samples. The exception to this is with the 5 wt% sample, where an increase in size is observed upon heat treatment (from (30.1 ± 0.2) nm to (32.7 ± 0.3) nm). This is most likely due to higher TiO_2 surface exposed because of the lower $Y(NO)_3$ loading and partial coating formed. Furthermore, the detected reduction is dependent on the Y_2O_3 content as the crystallite size of pristine TiO_2 decreased from (32.7 ± 0.3) nm to (26.6 ± 0.2) nm as the coating layer increased from 5 to 25 wt% (Table 4.1).

Table 4.1: Mean crystallite size of the studied nanomaterials in this research calculated with the Scherrer equation.

Sample		Mean crystallite size (nm)
ZnO		77 ± 1
TiO_2		34.9 ± 0.3
TiO_2 annealed		35.6 ± 0.3
TiO_2@$Y(OH)_3$	5 wt%	30.1 ± 0.2
	10 wt%	33.4 ± 0.3
	25 wt%	30.7 ± 0.2
TiO_2@Y_2O_3	5 wt%	32.7 ± 0.3
	10 wt%	30.9 ± 0.2
	25 wt%	26.6 ± 0.2

STEM micrographs of TiO_2 (Figure 4.3) show the tendency of these particles to form agglomerates of sizes ranging from approximately 50 nm up to 500 nm in diameter. However, the particles forming these agglomerates vary in size, as shown by the particle size distribution histogram (Figure C.5), from 10 to 45 nm. A mean particle size of (23 ± 7) nm was determined using ImageJ, which is in agreement with the reported particle size of 21 nm by the product supplier [149]. Furthermore, according to hydrodynamic size measurements (Table 4.5), once in suspension and sonicated for 1- 2 hours, the larger agglomerates dissociate into possibly smaller clusters ((70 ± 1) nm).

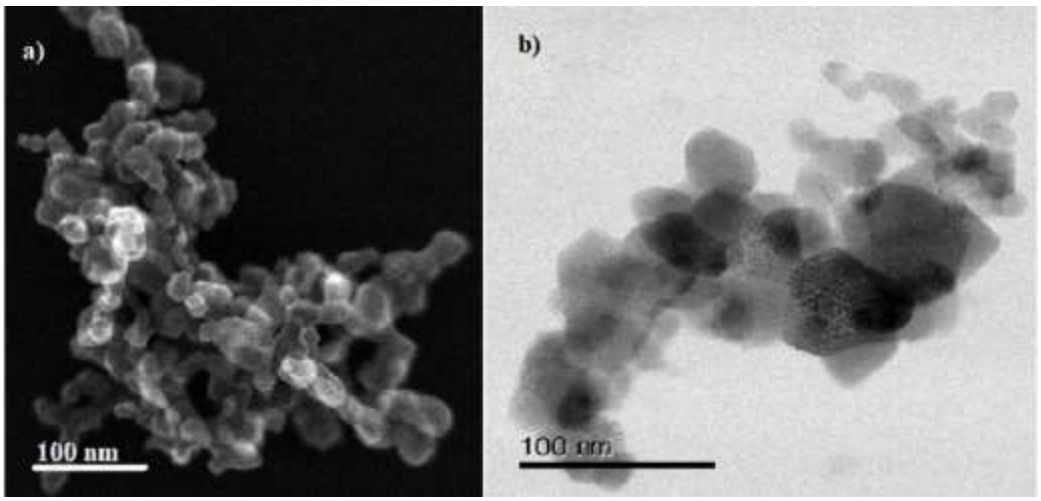

Figure 4.3: STEM micrographs of TiO_2 obtained in (a) SEM and (b) bright field imaging modes.

Highlighted in Figure 4.4 are the morphology and general size distribution of the synthesised precursor (Figures 4.4 (a) and (b)) and annealed (Figures 4.4 (c) and (d)) samples at 10 and 25 wt%. It can be seen that these samples contain a mixture of morphologies, from spherical TiO_2 particles to plate like particles ($Y(OH)_3$ and/or Y_2O_3) found across the TiO_2 particles, as confirmed by EDS mapping (Figures C.3 and C.4). These plate particles are present in both precursor and annealed samples, as shown in Figure 4.4 (a) and (c); thus, the formation of such particles occurred during the hydrothermal synthesis. Such formation is highly likely due to the lack of stirring during autoclaving, resulting in the sedimentation of $Y(OH)_3$ and further nucleation, resulting in densification of the plate shaped structures with widths of approximately 500 nm (Figures C.4 and C.7).

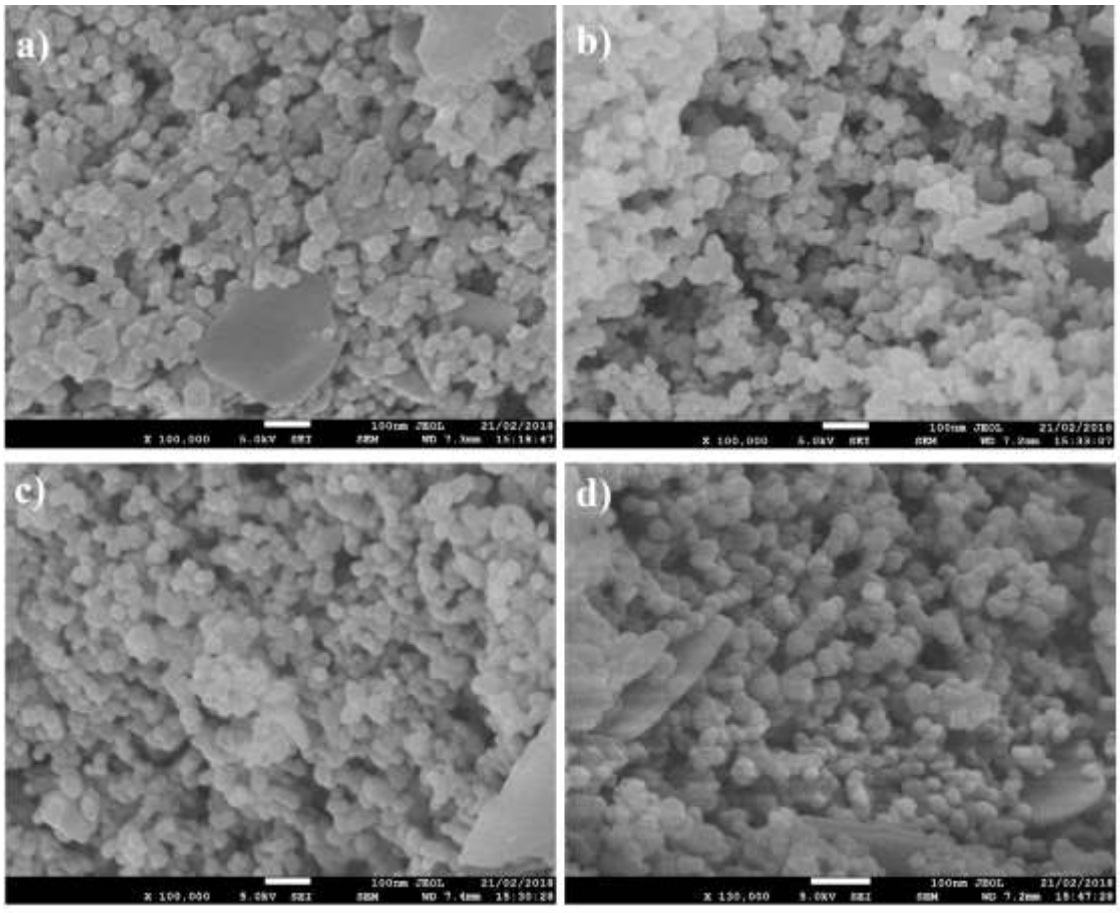

Figure 4.4: SEM micrographs of (a) TiO_2@$Y(OH)_3$ 10 wt%, (b) TiO_2@$Y(OH)_3$ 25 wt%, (c) TiO_2@Y_2O_3 10 wt% and (d) TiO_2@Y_2O_3 25 wt%.

TEM micrographs of TiO_2@Y_2O_3 at 5, 10 and 25 wt% are shown in Figure 4.5. In all the images, the TiO_2 core displays high crystallinity which coincides with the XRD patterns

in Figure 4.2. Moreover, the Y_2O_3coating layer is very thin in all the annealed samples, suggesting that the diffraction peaks related to the formation of Y_2O_3 in Figure 4.2 (b) arise from the mentioned plate shaped particles in Figure 4.4. The morphology of these particles remains unaltered, resembling pristine TiO_2 particles, as seen in the STEM and SEM micrographs (Figures 4.3 and 4.4). The TEM micrographs of the precursor samples (Figure C.2) show semi-amorphous coating layers on TiO_2, supporting the evidence of the amorphous phase in Figure 4.2 (a) at 25 wt% at 15°, whereas the annealed samples display crystalline Y_2O_3 coating layers. Moreover, as highlighted in Table 4.2, the mean particle size determined from the TEM micrographs of the synthesised particles follows the trend observed with the mean crystallite sizes calculated using the Scherrer equation (Table 4.1), whereby the particle size is reduced upon heat treatment.

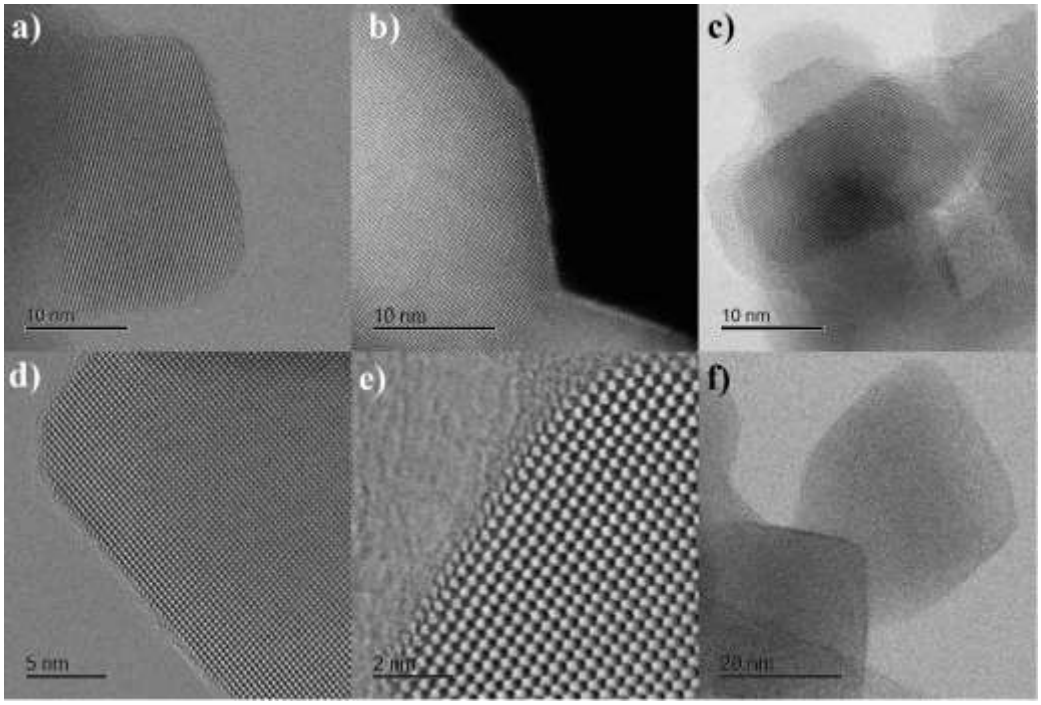

Figure 4.5: TEM micrographs of TiO_2@Y_2O_3 at (a), (d) 5 wt%, (b), (e) 10 wt% and (c), (f) 25 wt% Y content.

Energy-dispersive X-ray spectroscopy (EDS) was used to determine possible sodium (Na) contamination arising from the synthesis procedures where NaOH was used as the precipitating agent (Section 3.2). No Na was detected through EDS analysis of the precursor particles, suggesting that the washing of the sample prior to being dried and annealed removed all traces of Na from autoclaving.

High resolution EDS mapping was also used to confirm the theoretical Y wt% values in the $TiO_2@Y_2O_3$ samples and its distribution along the TiO_2 core (Figure 4.6). The EDS images show that yttrium (green) is distributed around TiO_2 (red) particles forming a coating layer, confirming what was found by the TEM micrographs. Furthermore, Figure 4.6 shows the increase in Y content from (a) to (c), as theoretically calculated. The calculated weight percentage using the EDS mapping data for $TiO_2@Y_2O_3$ 5 and 10 wt% was (4.6 ± 0.3) wt% and (9.2 ± 0.8) wt%, respectively; thus, the Y content in these samples correlates well with the theoretical values. However, the actual ratio for the 25 wt% sample was much lower than the target ratio, which was (15.2 ± 0.3) wt%. Such a result could be due to the favourable nucleation and formation of sheet like particles at high yttrium salt content used during synthesis (Figure C.4 (b)). This leads to reduced growth of Y_2O_3 on the surface of TiO_2, and thus, lower Y wt% content calculated with EDS mapping performed on the synthesised core particles.

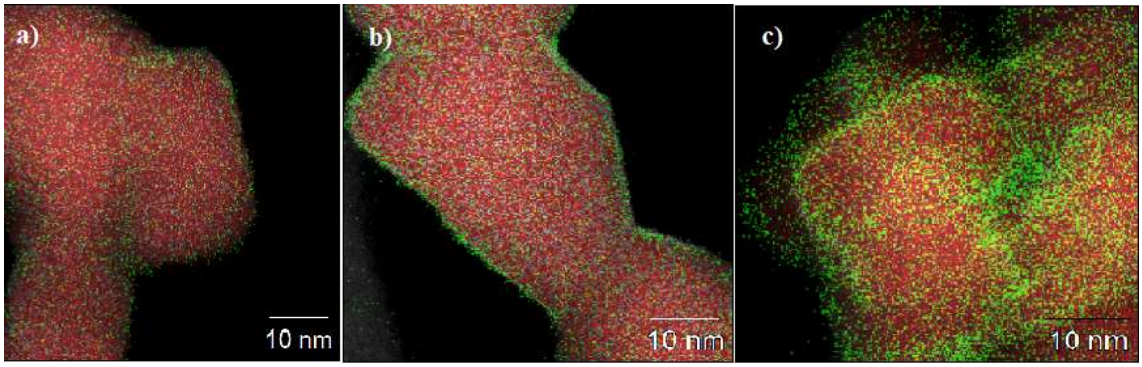

Figure 4.6: EDS mapping of $TiO_2@Y_2O_3$ at (a) 5 wt%, (b) 10 wt% and (c) 25 wt% Y content. Red and green regions correspond to Ti and Y atoms, respectively.

The specific surface area of ZnO, TiO_2 and the synthesised coated TiO_2 particles was measured in order to determine the relationship between the specific surface area and any potential change in the photocatalytic activity of TiO_2. Moreover, the cytotoxicity of TiO_2 nanoparticles has been reported to be correlated to high surface areas due to higher interaction with biomolecules and production of free radicals upon UV excitation [150].

The specific surface area of the particles was determined using Brunaeur-Emmett-Teller (BET) analysis. The determined BET surface areas of TiO_2 and ZnO are (48 ± 2) $m^2 \cdot g^{-1}$ and (13.4 ± 0.4) $m^2 \cdot g^{-1}$(Table 4.2), respectively, which coincide with the suppliers product information ((50 ± 15) $m^2 \cdot g^{-1}$ and 15-25 $m^2 \cdot g^{-1}$, respectively) [149]. The small measured surface area of ZnO could be attributed to large particles (Table 4.2), and thus, reduced

available surface area for nitrogen adsorption. Furthermore, these findings are in line with the calculated mean crystallite and particle size determined for pristine TiO_2 ((34.9 ± 0.3) nm and (23 ± 7) nm, respectively) (Tables 4.1 and 4.2), highlighting the inverse relationship between the specific surface area and size of a particle. Annealing of pristine TiO_2 results in a reduction in surface area and increase of crystallite and particle size, from (48 ± 2) $m^2 \cdot g^{-1}$ to (40 ± 1) $m^2 \cdot g^{-1}$ and from (34.9 ± 0.3) nm to (35.6 ± 0.3) nm and from (23 ± 7) nm to **(**29 ± 9) nm, respectively. Heat treatment of nanoparticles results in the formation of large agglomerates as these are more energetically favourable due to the reduced free surface energy. Hence, a reduction in the surface area is observed due to increased crystallite and particle size (Tables 4.1 and 4.2) [145].

Table 4.2: Mean particle sizes and BET specific surface area of the studied nanomaterials in this research.

Sample		Mean particle size (nm)	Specific surface area ($m^2 \cdot g^{-1}$)
ZnO		80 ± 40	13.4 ± 0.4
TiO_2		23 ± 7	48 ± 2
TiO_2 annealed		29 ± 9	40 ± 1
TiO_2@$Y(OH)_3$	5 wt%	19 ± 7	52 ± 1
	10 wt%	24 ± 8	62 ± 6
	25 wt%	21 ± 6	48 ± 2
TiO_2@Y_2O_3	5 wt%	20 ± 6	46 ± 5
	10 wt%	21 ± 7	128 ± 9
	25 wt%	21 ± 7	54 ± 3

The relation between the specific surface area and the Y content in the precursor and annealed coated particles is shown in Figure 4.7 and Table 4.2. Generally, the synthesised particles display higher surface area than pristine TiO_2. There is an increase in surface area as the Y content increases from 5 to 10 wt% and a reduction from 10 to 25 wt%. This effect is more predominant on the annealed samples, as shown in Figure 4.7. Additionally, annealing of the TiO_2@$Y(OH)_3$ samples results in an increase in surface area, arising from possible pore formation on the coating layer as the reduction of particle size is not

significant (Table 4.2) [75]. An exception to this is the 5 wt% sample, where a slight decrease is observed (from (52 ± 1) $m^2 \cdot g^{-1}$ to (46 ± 5) $m^2 \cdot g^{-1}$) due to the increase in size. The significant increase in the surface area of $TiO_2@Y_2O_3$ 10 wt% could be attributed to a favourable pore formation from the decomposition of the hydroxide precursor (Equation A.2), as previously reported [75]. The thermal decomposition of $Y(OH)_3$ has been established to mainly follow two steps as determined via thermo-gravimetric analysis and differential-thermo analysis [114]. First, dehydration of $Y(OH)_3$ through the loss of absorbed and bonding water molecules and second, crystallisation of Y_2O_3 [114]. During the dehydration process, the amount of gas molecules produced aids in decomposing the solid or in pore formation and thus, an increase on surface area at temperatures between 350 - 600 °C [151-153]. Porosity results in increased surface area since these structures allow for more gas molecules to be adsorbed as they translocate into the porous formations. However, by further increasing the yttrium salt content during synthesis, only a slight increase in surface area is observed upon heat treatment, potentially attributed to a higher formation tendency of plate like particles mentioned in the previous section.

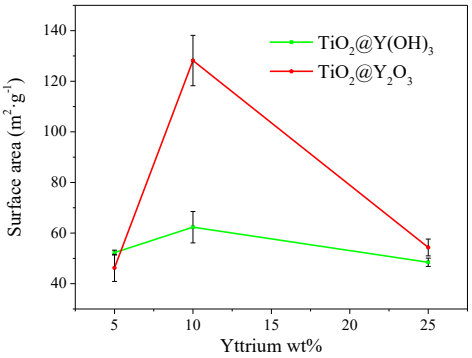

Figure 4.7: Specific surface area of the synthesised nanoparticles for each Y wt% of the precursor and annealed samples using BET analysis.

4.2 Optical properties and bang gap calculations

Ultraviolet filters protect the human skin against UV radiation through reflection, scattering or absorption of incident UV rays [13]. Hence, an essential requirement for UV filters is that they absorb radiation within the UV range of the electromagnetic spectrum. As such, the suitability of the synthesised particles for UV filtration applications was assessed through UV-vis spectrophotometry, along with the UV-vis absorption characterisation of commercial ZnO and TiO_2 nanoparticles.

Highlighted in Figure 4.8 are the UV-vis absorption spectra of commercial TiO_2 (25 mg·L^{-1}) and ZnO at 25 and 50 mg·L^{-1}. These curves depict the same characteristic absorption spectra as depicted in Figure 2.9 for TiO_2 and ZnO nanoparticles, with broad absorption peaks between 200-400 nm corresponding to UVB and UVA absorption. The broadness of the peak in the TiO_2 curve could be due to the presence of rutile in the crystal phase of the material as the rutile phase absorbs at 360 nm whereas the anatase form absorbs at 320 nm [154]. The low intensity absorption of ZnO compared to TiO_2 is ascribed to fewer available excitation states of ZnO due to its conduction band being formed by filled 3d orbitals whereas the Ti conduction band is partially filled. This allows for a greater number of excitations to take place from the valence to the conduction band (O 2p orbitals to Ti 3d orbitals) of TiO_2, in addition to the greater number of surface atoms due to the reduced particle size to interact with the incident radiation [155, 156]. Moreover, both commercial particle solutions scatter significant amount of visible light possibly due to agglomeration, resulting in scattering of wavelengths corresponding to the visible light region (Appendix D.1). The calculated energy band gap (Table 4.3 and Figures D.2 and 3.6) for TiO_2 and ZnO is (3.21 ± 0.02) eV and (3.15 ± 0.08) eV, respectively. These values are close to those specified by the TiO_2 supplier, where a band gap of 3.05 and 3.29 eV corresponding to the rutile and anatase phase, respectively, are given [149]. The *Eg* value obtained for ZnO ((3.15 ± 0.08) eV) falls within that found in the literature (3.1 to 3.3 eV) [69].

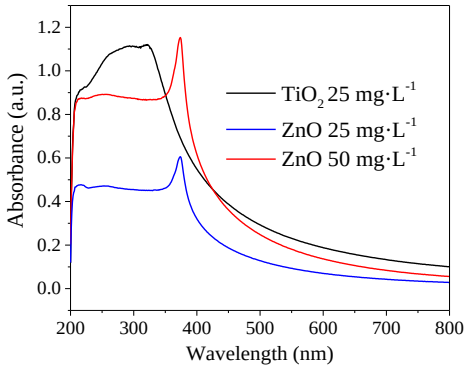

Figure 4.8: UV-vis absorption spectra of commercial TiO_2 and ZnO nanoparticles at different nanoparticle concentration suspended in ethanol.

As shown in Figure 4.9, the synthesised particles showed significant absorption over the UVB and short UVA range (280–340 nm). Additionally, in general, the addition of Y on TiO_2 results in a higher absorbance intensity, an effect that is more pronounced for the TiO_2@Y_2O_3 5 and 10 wt% samples. Such an increase in intensity can be due to the

scattering of incidents photons by Y into TiO_2; thus, triggering charge separation, as it has been previously reported for rare earth oxides [157] and organic semiconductor coated silver particles [158]. Since such an effect is highlighted on particles with partial coating at Y 5 and 10 wt%, a significant absorption enhancement is observed for TiO_2@Y_2O_3 5 and 10 wt% due to the higher degree of exposed TiO_2 surface available for uptake of scattered photons. Similarly, a moderate increase in the absorbance intensity is seen in the rest of the synthesised samples. This difference could be attributed to the difference in the thickness of Y coating formed on TiO_2 at varying Y content. Once the surface of TiO_2 is covered with $Y(OH)_3$/Y_2O_3 at 25 wt%, a reduction in the incident photons scattered towards TiO_2 occurs (Figure 4.9). The precursor samples do not show the same significant absorption enhancement as the annealed samples. Such a result could be ascribed to reduced scattering due to $Y(OH)_3$ as compared to Y_2O_3 (Figure D.1) and subsequent reduction in scattering induced absorption. Moreover, the synthesised particles show improved transparency through a reduction in scattering over wavelengths above 350 nm compared to pristine TiO_2 possibly due to reduced size, as outlined in Table 4.2. As such, cosmetic products containing these particles will appear more transparent than those containing TiO_2, and hence, be more aesthetically appealing.

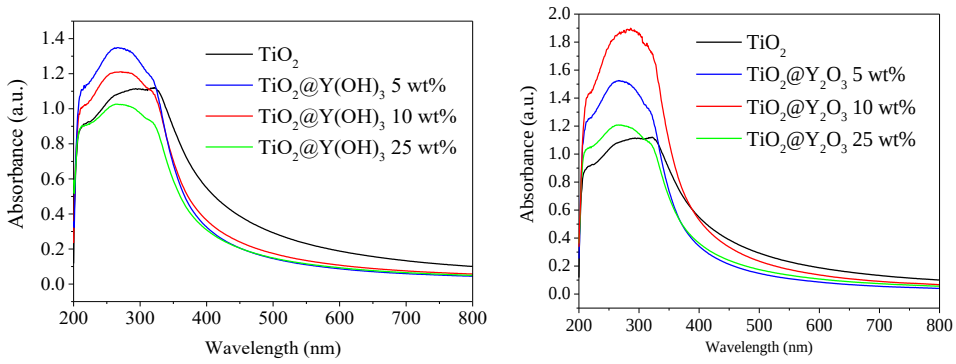

Figure 4.9: UV-vis spectra of (a) TiO_2@$Y(OH)_3$ and (b) TiO_2@Y_2O_3 coated particles at varying Y wt%.

Furthermore, from the optical *Eg* of these materials (Table 4.3) calculated using Tauc plots derived from Equation 3.6 (Figure D.2), the incorporation of Y on TiO_2 slightly affects the absorption and optical band gap of the nanocomposites, compared to pristine

TiO_2. A slight blue shift in the absorption is observed when comparing the absorbance of pristine and coated TiO_2 alongside with a band gap widening of pristine TiO_2. As previously reported in Section 4.1, the synthesised particles are smaller than TiO_2 which, as per the quantum confinement effect, results in the aforementioned blue shift. Additionally, as yttria has a higher band gap relative to the core TiO_2, the addition of yttria onto the core particles could result in the mentioned band gap widening of the nanocomposite particles. Furthermore, as reported in the literature, an heterojunction could be formed between the TiO_2 core and the yttrium layer, shifting the Fermi level of TiO_2 towards the conduction band resulting in the expanded optical *Eg* calculated [75].

Table 4.3: Calculated optical *Eg* of the materials used in this research.

Sample		Optical *Eg* (eV)
ZnO		3.18 ± 0.08
TiO_2		3.21 ± 0.02
TiO_2@$Y(OH)_3$	5 wt%	3.47 ± 0.02
	10 wt%	3.43 ± 0.03
	25 wt%	3.43 ± 0.04
TiO_2@Y_2O_3	5 wt%	3.50 ± 0. 04
	10 wt%	3.43 ± 0.02
	25 wt%	3.48 ± 0.02

The spectroscopic properties of the synthesised composite materials make them suitable for their inclusion in sunscreen products as they show increased UV absorbance as well as improved transparency over the visible light region, which would result in more aesthetically pleasant cosmetic products.

4.3 Photocatalytic activity characterisation

Ultraviolet filters present in sunscreen products are semiconductor nanoparticles which, upon UV excitation, generate free radical species owing to their photocatalytic activity [14]. These ROS have the potential to induce the degradation of the organic components in sunscreens as well as toxic effects to the environment and product users [83]. As such, less photocatalytically active nanoparticle ingredients are preferred. The assessment and

characterisation of the photocatalytic activity of the studied materials used in this thesis was performed through the degradation of crystal violet.

Crystal violet (CV) degradation due to excited TiO_2 and ZnO nanoparticles under UV and simulated solar radiation, and thus, the photocatalytic activity of these materials is highlighted in Figure 4.10 and Table 4.4 through the apparent rate constant (k) calculated as per Equation 3.8 from the kinetic plots (Figure E.1). As expected, TiO_2 showed the highest activity, and thus, the greatest dye degradation due to generation of ROS upon both radiation types (96 and 98 % dye degradation upon UV and simulated solar radiation, respectively). As ZnO has a similar band gap to TiO_2 ((3.18 ± 0.08) eV and (3.21 ± 0.02) eV, respectively), it also expected to get excited under both irradiation types used and degrade the dye, as shown in Figure 4.10 and Table 4.4. However, as reflected by a lower rate constant and reduced dye degradation, ZnO is less photocatalytically active than TiO_2. An explanation for this could be due the smaller specific surface area of ZnO ((13.4 ± 0.4) $m^2 \cdot g^{-1}$) compared to TiO_2 ((48 ± 2) $m^2 \cdot g^{-1}$). This could suggest there are fewer reaction sites for the dye molecules to adsorb onto the particles surface, and hence, the observed reduction in photocatalytic activity of ZnO, highlighting the relationship between specific surface area and photocatalytic activity mentioned in the literature [83]. Furthermore, as shown in Figure 4.8, ZnO does not absorb UV light as efficiently as TiO_2 and, as such, excitation of e^- to form an e^-/h^+ pair and subsequent ROS generation does not take place as readily as for TiO_2.

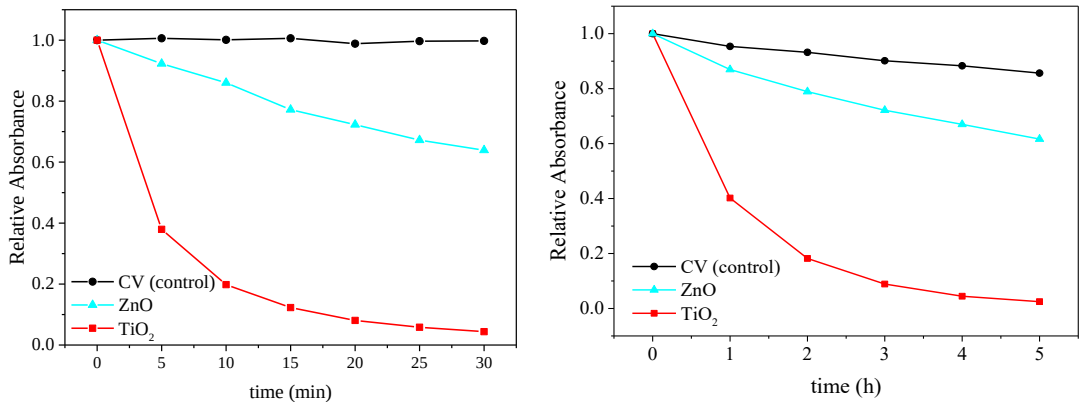

(a) (b)

Figure 4.10: Photocatalytic degradation of crystal violet due to commercial TiO_2 and ZnO nanoparticles under (a) UV and (b) simulated solar radiation.

Shown in Table 4.4 are the calculated apparent rate constant (k) using the Langmuir-Hinshelwood model (Figure E.1) for the synthesised core-shell particles as well as their dye degradation efficiencies. All samples display reduced photocatalytic activity compared to bare TiO_2, which is enhanced with increasing yttrium content (Figure 4.11). This trend could be the result of the improved coating layer as the Y content increases. As mentioned in Section 2.2.2.2, the photocatalytic reaction takes place on the surface of TiO_2; thus, by reducing the TiO_2 area exposed to the dye with a coating layer, a significant reduction in the catalytic activity is observed. The yttrium coating layer could directly inhibit the formation of hydroxyl radicals by blocking the surface migration of the e^-/h^+ pairs formed or act as a recombination centre and further prevent reactions with adsorbed dye molecules. This would result in the observed activity reduction of both the precursor and annealed samples with increasing Y content compared to pristine TiO_2. [65, 159, 160]. In the case of the precursor samples, the slight reduction could be explained by the semi amorphous $Y(OH)_3$ layer acting as a trap for the e^-/h^+ pairs, reducing the charge recombination efficiency and resulting in the observed higher activity compared to the annealed samples [161].

Table 4.4: Apparent rate constant (k) and photocatalytic efficiency of commercial ZnO, TiO_2 and synthesised $TiO_2@Y(OH)_3$ and $TiO_2@Y_2O_3$ particles at different Y wt% under UV and simulated solar radiation.

Sample		UVA/UVB radiation		Simulated solar radiation	
		k ($\times 10^{-2}$ min^{-1})	Dye degradation (%)	k ($\times 10^{-3}$ min^{-1})	Dye degradation (%)
CV (control)		0.03 ± 0.02	0.2	0.50 ± 0.03	14
ZnO		1.5 ± 0.2	36	1.57 ± 0.09	38
TiO_2		10 ± 1	96	12.3 ± 0.4	98
$TiO_2@Y(OH)_3$	5 wt%	7.69 ± 0.07	90	4.5 ± 0.4	74
	10 wt%	3.9 ± 0.1	69	3.1 ± 0.1	61
	25 wt%	2.4 ± 0.1	52	1.59 ± 0.07	39
$TiO_2@Y_2O_3$	5 wt%	2.11 ± 0.04	48	3.8 ± 0.1	68
	10 wt%	0.90 ± 0.06	25	2.26 ± 0.04	49
	25 wt%	0.64 ± 0.04	18	1.90 ± 0.08	44

Moreover, annealing further reduces the photocatalytic activity of the particles under UV excitation (Figure 4.11 (a) and (b)). Such an outcome could be the result of the synthesis method employed. As shown in Equation 2.6, surface adsorbed OH^- accepts photogenerated holes migrated to the surface of TiO_2 to form hydroxyl radicals which degrade the dye. Hence, the OH^- group on the $Y(OH)_3$ layer could react with the h^+ formed on TiO_2, resulting in the increased dye reduction observed (90% compared to 48% after heat treatment of the 5 wt% samples) [28]. In a similar fashion, by annealing the precursor samples a reduction in adsorbed OH^- is achieved. Consequently, a decrease in dye degradation and rate constant is obtained regardless of the increased surface area and UV absorption properties of annealed samples reported in Table 4.2 and Figure 4.9, respectively (Table 4.4 and Figure 4.11). It has been shown that the surface area plays an important role in the photocatalytic activity of TiO_2 [150]. Thus, according to previous results, the photocatalytic activity of the annealed samples should follow the next trend: 10 wt% ($(128 \pm 9)\ m^2 \cdot g^{-1}$) > 25 wt% ($(54 \pm 3)\ m^2 \cdot g^{-1}$) > 5 wt% ($(46 \pm 5)\ m^2 \cdot g^{-1}$). However, as mentioned before, this is not the case. The lower the Y content in the sample, the higher the photocatalytic activity. As a result, $TiO_2@Y_2O_3$ 25 wt% exhibits the highest reduction in the photocatalytic activity of TiO_2, followed by $TiO_2@Y_2O_3$ 10 and 5 wt% ($(0.64 \pm 0.04)\times10^{-2}$ min^{-1}, $(0.90 \pm 0.06)\times10^{-2}$ min^{-1} and $(2.11 \pm 0.04)\times10^{-2}$ min^{-1}, respectively). Furthermore, as per the UV absorption efficiencies of these samples, charge separation is favoured at 10 wt% yttrium content followed by 5 and 25 wt% yttrium content (Figure 4.9 (b)). By a combination of greater surface area for dye molecules to be adsorbed and enhanced UV absorptivity or charge separation, it would have been expected for $TiO_2@Y_2O_3$ 10 wt% to display the highest dye degradation and photocatalytic activity. Nevertheless, this is not the case, suggesting that the photocatalytic efficiency of the annealed samples is governed by another mechanism than surface area and UV absorptivity. As mentioned in Section 2.5.2, yttria behaves as a free radical scavenger due to its high oxygen affinity and nonstoichiometric oxygen [112]. Thus, the observed further reduction in the photocatalytic activity of $TiO_2@Y(OH)_3$ upon annealing could also be the result of the antioxidant property of the Y_2O_3 layer. Moreover, this antioxidant behaviour would explain the photocatalytic activity reduction being dependant on the Y_2O_3 content on the sample instead of the surface area and/or UV absorption properties of the $TiO_2@Y_2O_3$ samples.

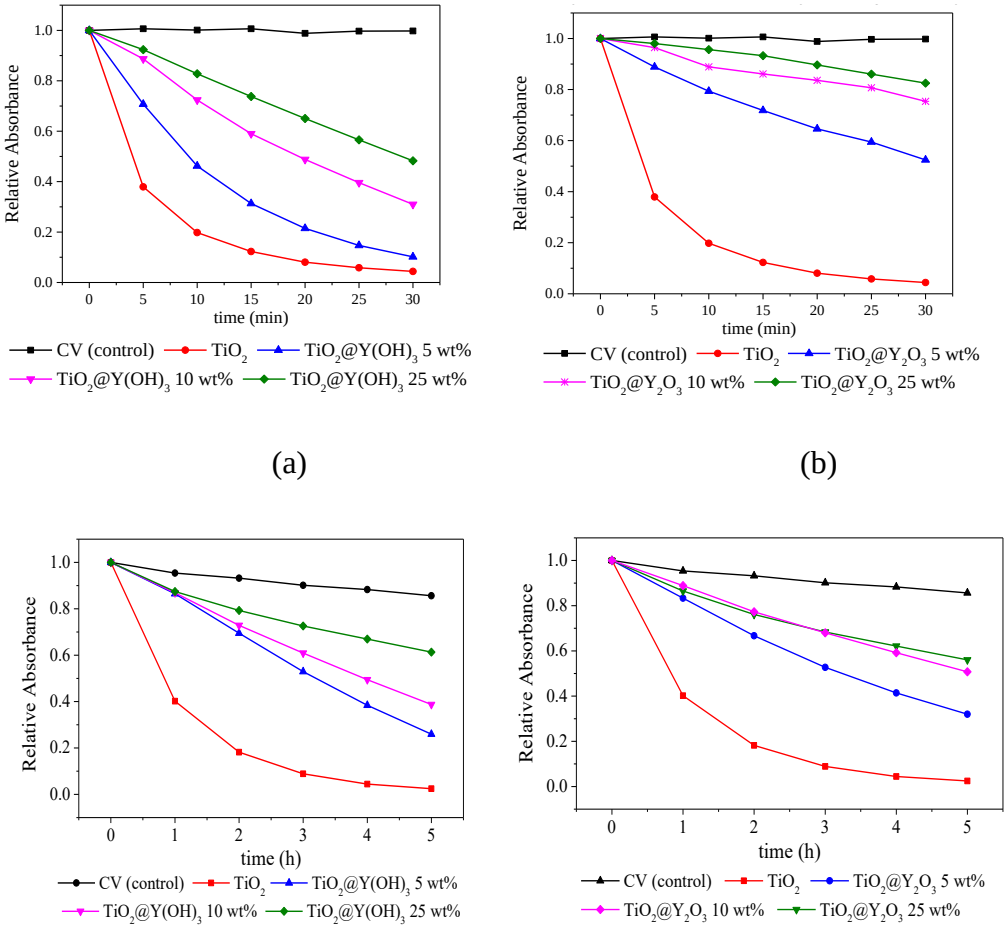

Figure 4.11: Photocatalytic degradation of crystal violet due to TiO_2@$Y(OH)_3$ and TiO_2@Y_2O_3 under UV radiation (a) and (b), respectively, and under simulated solar radiation (c) and (d), respectively, at varying Y content.

Under simulated solar radiation, the photocatalytic efficiency of the precursor and annealed samples seem to lessen and improve, respectively, compared to the UV based degradation results (Table 4.4). As with UV exposure, under simulated solar light the $Y(OH)_3$ layer is suggested to block the e^-/h^+ pair from reacting with the dye molecules leading to a reduction in their subsequent degradation. Under simulated solar radiation, the rate and amount at which free radical species are formed is diminished as reflected by a 10-fold k reduction ($\times 10^{-3}$ min^{-1}) compared to UV radiation rate constants ($\times 10^{-2}$ min^{-1}). As such, the more efficient activity reduction in the first case could potentially indicate a charge trapping centre saturation reached upon UV radiation but not upon simulated solar radiation. Hence, the enhanced photocatalytic activity reduction of TiO_2@$Y(OH)_3$ 25 wt% compared to the 10 wt% sample upon solar light degradation.

The observed enhancement in photocatalytic efficiency of the annealed samples upon change in light source could be explained by a tunnelling effect and subsequent sensitisation of TiO_2 to degrade the dye (Appendix E.2) [75, 162]. In this process, the dye molecules get excited and form cationic dye radicals which transfer an e^- to the conduction band of TiO_2. The charged particle then reacts with adsorbed aqueous, molecules resulting in the decolourisation of the organic dye molecules, as outlined in Equations E.1-E.6 and Figure 3.7 [163]. An apparent plateau is reached at $TiO_2@Y_2O_3$ 10 wt% (49% dye degradation compared to 44% at 25 wt%), as such, yttria layers above 10wt% do not seem to impart a significant effect on the photocatalytic activity of TiO_2. Such an effect could be explained by the increase in layer thickness and consequent reduction of photoinjected electron transfer from the excited dye molecule to the TiO_2 core. The free radical scavenging behaviour or charge recombination rate in the composites outweighs the tunnelling effect; thus, significantly low photocatalytic activity is still maintained compared to pristine TiO_2.

Enhanced UV absorption and low photocatalytic activity are ideal for UV filter nanoparticles for the inhibition of states of oxidative stress whilst protecting the human skin from UV exposure. Thus, $TiO_2@Y_2O_3$ 5 and 10 wt% are the most promising samples for UV filtration and potential biocompatibility due to a combination of their enhanced UV absorption properties and reduced photocatalytic activity as compared to pristine TiO_2. As such, these synthesised materials which absorb UV light while inhibiting the production of free radicals, could potentially be beneficial for the cosmetic industry. The incorporation of these particles in, for example, sunscreen products, would result in protection against UV radiation, reduction of free radicals produced, and therefore, possible antioxidant stabilisation for the organic filters present in the product; thus, maintaining an adequate SPF level and increasing the overall biocompatibility of UV filters.

4.4 *In vitro* cytotoxicity in HaCaT cells

The biocompatibility of commercial UV filters, ZnO and TiO_2, along with the most promising synthesised materials for UV filtration in sunscreen products, $TiO_2@Y_2O_3$ 5 and 10 wt%, was assessed through treatment of HaCaT cells with these particles for 24 hours in the absence and presence of simulated solar/UV light using the MTS

tetrazolium salt assay. This assay enables an assessment of the cytotoxicity of the studied materials by measuring the absorbance of formazan produced as a result of the reduction of MTS via mitochondrial activity [141, 164].

4.4.1 Cytotoxicity of ZnO nanoparticles in the absence of UV light

Cell viability reduction due to ZnO in HaCaT cells followed a concentration-response curve, as shown in Figure 4.12. A cell viability reduction at low nanoparticle concentration can be observed, from (84.7 ± 3.4)% to (73.8 ± 9.3)% at 2.5 and 5 $mg \cdot L^{-1}$, respectively. As such, the NOAEC of ZnO nanoparticles in HaCaT cells was determined to be < 2.5 $mg \cdot L^{-1}$ (Table 4.5). As the nanoparticle concentration increases, a sharp reduction in cell viability occurred, until a plateau at (2.5 ± 2.4)% was reached between 100-200 $mg \cdot L^{-1}$ (TLC of (100 ± 2) $mg \cdot L^{-1}$).

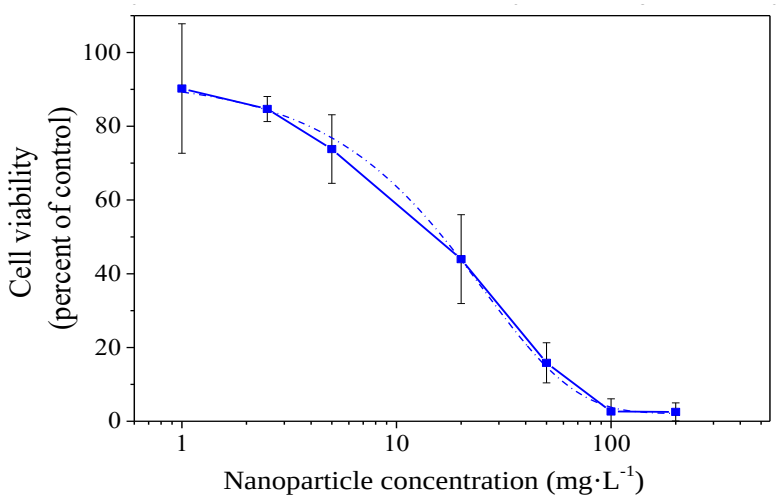

Figure 4.12: Concentration-response curve of HaCaT cells after 24 hour exposure to ZnO nanoparticles, expressed as percentage of viable cells with respect to IC_0 control.

The mechanism by which ZnO induces cytotoxicity is uncertain. Nevertheless, the generation of intracellular free radicals and the release of Zn^{2+} ions due to the high solubility of ZnO nanoparticles are believed to be the main mechanisms [2, 69]. In this research, the toxicity exerted by these nanoparticles is suspected to be due to both mechanisms, ion-shedding and generation of intracellular free radicals, leading to subsequent DNA damage (Figure H.1). The release of Zn^{2+} ions could explain the reduction of cell viability even at low nanoparticle concentration, due to greater dispersibility at lower nanoparticle concentration, and thus, higher surface area available

for Zn^{2+} ions to be released from (Figure 4.12) [69]. The solubility of ZnO nanoparticles is greater in acidic media than neutral media [69]. Therefore, the solubility of the tested ZnO particles is reduced in the culture media used since the pH is 7.4 in order to maintain a healthy environment for the cells to grow. Phenol red changes in colour to yellow in acidic conditions and to purple in basic conditions. Thus, qualitatively, the pH remained stable over the assay period as no change in phenol red colour occurred, possibly resulting in a decreased release of Zn^{2+} ions due to a reduced solubility of ZnO. However, the sharp reduction in cell viability as the nanoparticle concentration increases, could be caused by a combination of free radicals stimulated by the dissolved ions and the latter. As previously reported, it is highly possible that some ZnO nanoparticles attach to the cell membrane and, consequently, they are internalised through endocytosis [69]. Once in the cytoplasm, these particles could dissolve because of the acidic conditions within the cell and release Zn^{2+} ions, damaging the mitochondria and resulting in the generation of free radicals and reduced formazan product (Figure H.1) [69].

The obtained results highlight the high toxicity of ZnO nanoparticles in HaCaT cells and thus, the calculated low IC_{50} of (11 ± 1) $mg \cdot L^{-1}$ (Table 4.5). This value is in agreement with that reported in a recent study where an IC_{50} of ZnO in HaCaT cells was found to be between 10-20 $mg \cdot L^{-1}$ [165]. As mentioned in Section 2.3.2, Dechsakulthorn *et al.* (2008) reported an IC_{50} of (50 ± 13) $mg \cdot L^{-1}$ on human skin fibroblasts after 24 hour exposure to ZnO nanoparticles whereas an IC_{50} of $(2.70 \pm 0.67) \times 10^3$ $mg \cdot L^{-1}$ was reported for TiO_2, showing the higher cytotoxicity of ZnO over TiO_2 nanoparticles [21].

Multiple analyses methods should be performed in conjunction with the MTS tetrazolium salt assay in order to determine the mechanism by which ZnO nanoparticles induce cytotoxicity in HaCaT cells. However, this is beyond the scope of this thesis.

4.4.2 Cytotoxicity of TiO_2 based nanoparticles

The cytotoxicity of TiO_2 and $TiO_2@Y_2O_3$ 5 and 10 wt% in HaCaT cells was assessed under the absence and presence of simulated solar radiation, emulating acute UV exposures reflective of Darwin, Australia [144].

4.4.2.1 In the absence of UV light

The effect of pristine TiO_2 and coated $TiO_2@Y_2O_3$ 5 and 10wt% samples on the viability of HaCaT cells is shown in Figure 4.13. As observed in this figure, cell viability of HaCaT cells was reduced in a concentration dependent manner following 24 hour treatment with TiO_2 nanoparticles. At high nanoparticle concentrations, 100-500 $mg \cdot L^{-1}$, a reduction in HaCaT cell viability can be observed in cells treated with TiO_2 even without UV irradiation, from (93.2 ± 1.6)% to (66.2 ± 9.8)% at 100 and 500 $mg \cdot L^{-1}$, respectively.

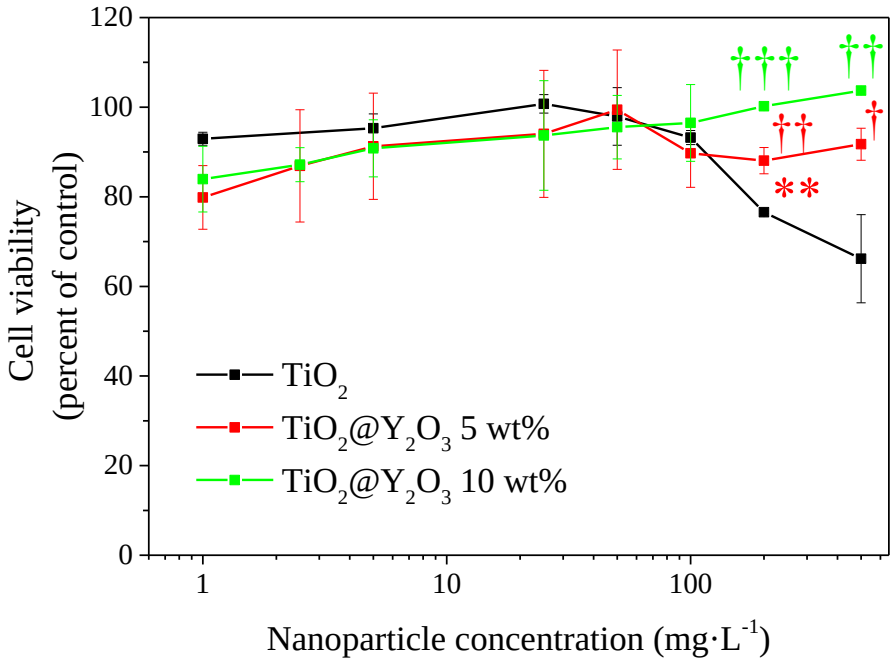

Figure 4.13: Reduction in HaCaT cell viability due to 24 hour exposure to TiO_2, $TiO_2@Y_2O_3$ 5 and 10 wt%, expressed as percentage of viable cells with respect to IC_0 control. Compared to TiO_2 † indicates $p < 0.05$, †† indicates $p < 0.01$ and ††† indicates $p < 0.001$. Compared between the synthesised particles ** indicates $p < 0.01$.

Such high nanoparticle concentrations might cause cell or organelle membrane injury and oxidative stress [69]. Multiple studies have assessed the cytotoxicity of TiO_2 nanoparticles on different systems in the absence of UV exposure and attributed the observed toxicological effects to increased intracellular ROS production upon internalisation and subsequent oxidative stress and apoptosis [166-172]. In a theoretical framework, TiO_2 was proposed to have an oxidative stress potential/band gap comparable to redox potentials of biological reactions involved in the formation of radical species

[100, 173]. This suggests a favoured electron transfer between TiO_2 and cellular components and, consequently, induced oxidative stress [100, 173]. Furthermore, recent studies on several cell types exposed to TiO_2 nanoparticles have found that generated ROS induced oxidative stress through a cascade of processes initiated by the induction of endoplasmic reticulum stress and, ultimately, autophagy (Figure H.2) [169, 174-176]. The endoplasmic reticulum is an organelle primarily responsible for protein synthesis, folding and sorting, and calcium storage and release [175, 177, 178]. Shortage of calcium causes the inactivation of chaperons in the endoplasmic reticulum which leads to misfolded proteins [176]. Aggregation of misfolded proteins brings about endoplasmic reticulum stress and subsequent initiation of the unfolded protein response and autophagy [172, 175, 176]. These responses are responsible for restoring homeostasis within the endoplasmic reticulum [175, 176]. Autophagy is the process by which foreign, unnecessary and dysfunctional cellular matter within the cytoplasm is encapsulated in a vesicle, which then fuses with a lysosome resulting in the degradation of the unwanted products [169, 179]. This process, is triggered by oxidative stress mechanisms such as mitochondrial damage or, as mentioned before, endoplasmic reticulum stress [172]. Thus, autophagy is involved in the improvement of stress conditions through the clearance of aggregated misfolded proteins. Autophagy in the presence of TiO_2 nanoparticles has been evaluated and shown through TEM, where a double membrane organelle contained cellular material, as well as TiO_2 particles [180]. Hence, in a similar fashion, in our case, at low TiO_2 nanoparticle concentrations no toxicological effects were observed in HaCaT cells (Figure 4.13) possibly due to successful degradation of potentially internalised TiO_2 [169] or oxidated damaged molecules and cell structures due to ROS generation [180]. However, at higher nanoparticle concentrations possible autophagy blockade occurred, and thus, impeded clearance of oxidative stress inductors and damaged cellular components, resulting in organelle damage, mitochondrial dysfunction through an imbalance of calcium and oxidative stress through imbalance of free radicals, as previously reported [172, 174, 178].

Commercial TiO_2 nanoparticles caused the highest cell viability reduction followed by $TiO_2@Y_2O_3$ 5 and 10 wt% at the highest tested concentration of 500 $mg \cdot L^{-1}$ ((91.7 ± 3.6)% and (103.71 ± 0.07)%, respectively), compared to IC_0. Such an outcome could be the result of larger $TiO_2@Y_2O_3$ 10 wt% particles formed in media (Table 4.5), compared to the other two samples, suggesting that both particles tend to form clusters

when dispersed in solution; however, these differences are not significant. Thus, another explanation could be the reduced photocatalytic activity of TiO_2 because of the presence of Y_2O_3 as $TiO_2@Y_2O_3$ 10 wt% yields the lowest activity followed by $TiO_2@Y_2O_3$ 5 wt% and TiO_2. This trend is highlighted by the calculated differences in NOAEC values (Table 4.5). Furthermore, $TiO_2@Y_2O_3$ 10 wt% treatment at 500 $mg \cdot L^{-1}$ promoted cell viability. As reported in the literature [101, 111, 181], Y_2O_3 behaves as an antioxidant implying that at high nanoparticle concentration, potential free radicals generated due to nanoparticle presence could have been scavenged by the antioxidant coating layer. Hence, oxidative stress mediated toxicity mechanisms explained above could have potentially been avoided. Similarly, suppression of fullerene nanoparticle oxidative stress mediated autophagy in HeLa cells was achieved by N-acetylcysteine, an antioxidant [172]. The study of the potential cyto- or geno-toxic mechanisms of TiO_2 in HaCaT cells are out of the scope of this thesis. Nevertheless, we can infer that TiO_2 ROS generation mediated cytotoxicity in HaCaT cells is the main toxic mechanism as the cytotoxicity was affected by the presence of Y_2O_3, an antioxidant as per previous studies.

Table 4.5: Measured hydrodynamic size of the tested nanoparticles in DMEM/F12 media and calculated NOAEC, IC_{50} and TLC end points of the tested nanoparticles in HaCaT cells after 24 hour treatment in the absence of simulated solar radiation.

Sample		Hydrodynamic size (nm)	NOAEC ($mg\ L^{-1}$)	IC_{50} ($mg \cdot L^{-1}$)	TLC ($mg \cdot L^{-1}$)
ZnO		75 ± 6	< 2.5	11 ± 1	100 ± 2
TiO_2		70 ± 1	100 ± 5	> 500	> 500
$TiO_2@Y_2O_3$	5 wt%	69 ± 2	200 ± 2	> 500	> 500
	10 wt%	75 ± 4	500 ± 1*	> 500	> 500

*The observed effect is positive not adverse (NOEC).

The IC_{50} obtained for these samples are highlighted in Table 4.5. All tested particles display IC_{50} above the treatment concentrations employed. Similarly, Dechsakulthorn *et al.* (2008) calculated an IC_{50} of $(2.70 \pm 0.67) \times 10^3$ $mg \cdot L^{-1}$ for TiO_2 incubated with human

skin fibroblasts [21]. The difference in these two IC_{50} values could be due to the protocol followed as Dechsakulthorn *et al.* (2008) did not allow the cells to attach to the wells for 24 hours prior to the addition of the nanoparticles, but rather mixed the cells and nanoparticles at the same time. Moreover, the reported IC_{50} values depend on the cell line used. For instance, in the study of the toxicity of TiO_2 towards two malignant bone tumour cell lines for a 24 hour assay, IC_{50} values of (210 ± 15) $mg \cdot L^{-1}$ and $(5.41 \pm 0.05) \times 10^3$ $mg \cdot L^{-1}$ were obtained [182]. Hence, highlighting the effect of the protocol and cell line used in toxicological studies since, as shown, cell lines differ in inherent resistance against the same nanoparticles; thus, multiple IC_{50} values are obtained for the same nanomaterial. Nevertheless, the synthesised particles seem to promote cell viability since, as mentioned above, Y_2O_3 could potentially be acting as an ROS scavenger. Hence, cell viability seems to increase with increasing nanocomposite concentration (Figure 4.13).

Thus, these results show that in the absence of UV light the as-synthesised particles are less toxic than TiO_2, protecting the cells against potential oxidative stress and cell death, highlighting their improved biocompatibility.

4.4.2.2 In the presence of UV light

The effect of TiO_2, $TiO_2@Y_2O_3$ 5 and 10 wt% was assessed in HaCaT cells treated with these nanoparticles for 24 hours after 5 and 15 min exposure to simulated solar radiation as to emulate real life conditions (Figure 4.14). From the previous section, a reduction in cell viability was observed above 100 $mg \cdot L^{-1}$, suggesting cytotoxicity from possible oxidative stress induced cell or organelle damage. Thus, in this case, cells were treated with a nanoparticle centration range between 0-100 $mg \cdot L^{-1}$ as to ensure any effect caused on the cells did not rise from the intrinsic properties of the particles but rather from their photocatalytic activity and subsequent free radical generation, reduction or lack thereof.

As shown in Figure 4.14, 5 and 15 min exposure of HaCaT cells to simulated solar radiation resulted in a dose dependent cell viability reduction to (43 ± 3)% and (22 ± 3)%, respectively, as compared to a non-irradiated cell control plate set as 100% cell viability. Several studies have investigated the effect of UV radiation in HaCaT cells, establishing that UV radiation acts as a stressor in HaCaT cells, resulting in inflammation, oxidative and endoplasmic reticulum stress mediated apoptosis and cell proliferation inhibition

[183-189]. The irradiation dosage plays an important role in the resultant deleterious biological effects. It has been found that HaCaT cells exposed to UVB (10-30 $mJ \cdot cm^{-2}$) resulted in increased ROS levels within the cells, causing cell viability reduction in a dose dependent manner [183]. Additionally, the produced ROS facilitated calcium storage depletion in the endoplasmic reticulum leading to, as mentioned in the previous section, endoplasmic reticulum stress [183]. In a recent study, superoxide dismutase activity was significantly diminished in HaCaT cells after UVB irradiation (70 $mJ \cdot cm^{-2}$) [190]. Superoxide dismutase is an enzyme responsible for maintaining balanced levels of ROS by converting superoxide anions into hydrogen peroxide and molecular oxygen within the cells [28].

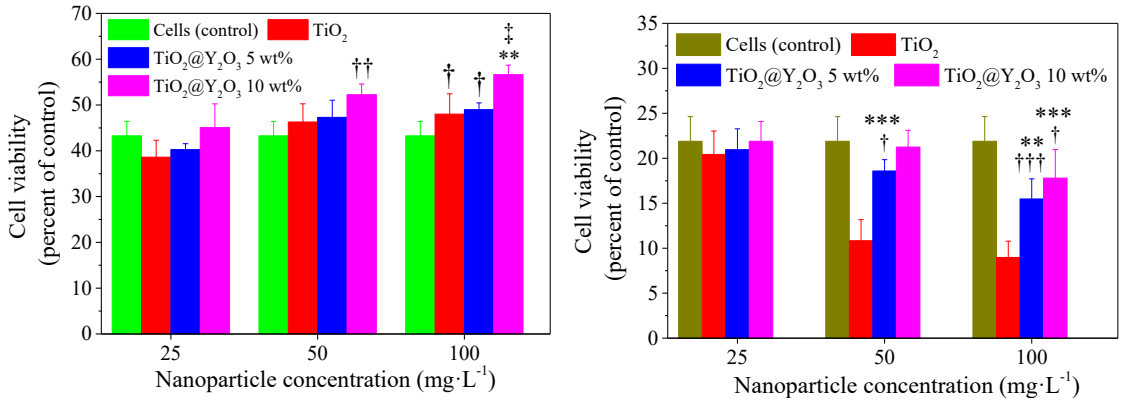

Figure 4.14: Change in HaCaT cell viability after 24 hour treatment with TiO_2 and $TiO_2@Y_2O_3$ 5 and 10wt% at 25, 50 and 100 $mg \cdot L^{-1}$ upon (a) 5 and (b) 15 min UV irradiation, expressed as percentage of viable cells with respect to IC_0 control (no UV). Cells (control) group has been plotted for each nanoparticle concentration to assist with comparisons. Compared with cells (control) † indicates $p < 0.05$, †† indicates $p < 0.01$ and ††† indicates $p < 0.001$. Compared to TiO_2 ** indicates $p < 0.01$ and *** indicates $p < 0.001$. Compared to $TiO_2@Y_2O_3$ 5wt% ‡ indicates $p < 0.05$.

Notably, at low UV doses the tested particles provided protection against UV radiation; however, at higher doses these particles induced cell death (Figure 4.14). This suggests the governance of different nanoparticle properties upon 5 and 15 min UV exposure, in addition of potential ROS scavenging from Y_2O_3. For instance, in the first case, the UV absorption efficiency of the tested particles prevails over free radical formation in a

concentration dependent manner. Nanoparticle treated cells resulted in higher cell viability than the control, most likely due to their absorptivity properties (Section 4.2). Furthermore, this also explains why $TiO_2@Y_2O_3$ 10 wt% resulted in the highest cell viability at all concentrations tested. Nevertheless, such an effect is only significant from 50 $mg \cdot L^{-1}$ for $TiO_2@Y_2O_3$ 10 wt% and at 100 $mg \cdot L^{-1}$ for TiO_2 and $TiO_2@Y_2O_3$ 5 wt% ((52 ± 4)%, (48 ± 4)% and (49 ± 1)%, respectively) (Figure 4.14 (a)). This effect was further enhanced by $TiO_2@Y_2O_3$ 5 and 10 wt% due to improved UV absorption compared to TiO_2 resulting in greater protection against UV radiation than TiO_2. However, such an improvement is only significant for $TiO_2@Y_2O_3$ 10 wt% at 100 $mg \cdot L^{-1}$ where a cell viability of (57 ± 2)% compared to (48 ± 4)% for TiO_2 was obtained. Similarly, silver nanoparticles have been found to also protect HaCaT cells exposed to low levels of UVB (40 $mJ \cdot cm^{-2}$) [191].

In the second case, the tested particles reduced cell viability in a concentration dependent manner (Figure 4.14 (b)), most likely due to ROS generation owing to their photocatalytic nature (Section 4.3), as supported by previous studies [20, 46, 97, 98, 192, 193]. Upon UV exposure, excitation of the tested nanomaterials could have occurred as per Section 4.3, and thus, the formed electron could have potentially reacted with molecular oxygen to generate ROS, ultimately resulting in cyto- and geno-toxicity through the complex network of processes mentioned in the previous section [194]. As observed in Figure 4.14 (b), the higher the yttria content, the less pronounced the cell viability reduction appeared. These results coincide with the reduction in photocatalytic activity of TiO_2 with increasing yttria content. No significant differences in cell viability were obtained when the nanoparticle concentration was 25 $mg \cdot L^{-1}$, neither compared with the control nor between nanoparticles. However, a significant cell viability reduction took place with TiO_2 treated cells at 50 and 100 $mg \cdot L^{-1}$((11 ± 2)% and (9 ± 2)%, respectively). A significant cell viability reduction at 50 $mg \cdot L^{-1}$ due to $TiO_2@ Y_2O_3$ 5 wt% and at 100 $mg \cdot L^{-1}$ due to 5 and 10 wt% composites occurred ((19 ± 1)%, (15 ± 2)% and (18 ± 3)%, respectively), compared to the control. In addition of being less photocatalytically efficient, and consequently being less prone to generate ROS, the synthesised composites could potentially be preventing cell death through the scavenging behaviour of the coating layer. As mentioned before, Y_2O_3 behaves as an antioxidant, hence, the detected inhibition on cell viability reduction could be a product of the suppression of ROS mediated cytotoxicity, as reported for multiple antioxidants [175,

183, 185, 195]. A series of studies have documented the inhibition of endoplasmic reticulum stress induced apoptosis upon treatment with antioxidants, resulting in the suppression of endoplasmic reticulum stress and consequent apoptosis [183, 195].

Cell protection and induced cell death upon 5 and 15 min UV irradiation occurred in a concentration dependent manner for all the assessed nanomaterials. Titanium dioxide caused the highest cell viability reduction after 15 min UV exposure. Between the synthesised nanoparticles, $TiO_2@Y_2O_3$ 10 wt% provided the most protection and least ROS formation. Such outcomes are hypothesised to be the result of a combination of a charge transfer blockage and free radical scavenging due to its coating layer; hence, displaying the highest biocompatibility between these particles.

Chapter 5

Conclusion and Future Work

In this project, TiO_2@$Y(OH)_3$/Y_2O_3 nanoparticles with varying yttrium content were synthesised through a hydrothermal method. The crystal structure and composition, specific surface area, size and morphology of these particles were studied. Additionally, the optical properties of these particles were also investigated. It was found that the introduction of yttrium on TiO_2 resulted in a high absorbance in the UVB and short UVA region, thus highlighting the potential application of these nanoparticles as UV filters. Moreover, scattering in the visible region was reduced, compared to pristine TiO_2, further highlighting the applicability of these particles in sunscreen products as these will appear transparent and be more aesthetically pleasant. Furthermore, a significant reduction in the photocatalytic activity of TiO_2 was achieved by these composites, as assessed upon UV and simulated solar irradiation. The underlying mechanism of such reduction was most likely due to an active charge carrier transfer blockage from the coating layer, as well as, the free radical scavenging property of yttrium oxide. Moreover, the toxicity of these composite particles along with pristine TiO_2 and ZnO in the absence of UV light was assessed in HaCaT human skin cells for 24 hour exposure via the MTS tetrazolium salt assay. The commercial samples, ZnO and TiO_2, displayed the highest toxicity towards HaCaT cells, the former being the most cytotoxic. The coated TiO_2@Y_2O_3 5 and 10 wt% particles exhibited the highest cell viability in all the tested conditions. Such an effect was found to be strongly related to the Y_2O_3 content, in that, the higher the Y_2O_3 loading, the higher the cell viability. In the absence of UV radiation, the composites seemed to

promote cell proliferation in a concentration, and yttria loading, dependent manner. Such an effect was suggested to be due to the antioxidant behaviour of the coating layer, as it has been previously reported in the literature. Under more realistic conditions, i.e. under simulated solar radiation, TiO_2 based nanoparticles were shown to induce contrasting effects at low and high UV doses, with cell protection against incident radiation and increased cell death, respectively. Protection and cell death were attributed to the previously determined UV absorption and photocatalytic efficiencies of the tested materials, respectively. Thus, $TiO_2@Y_2O_3$ 10 wt% displayed the highest protection and least induced cell death followed by the 5 wt% composite and TiO_2. These results highlight the improved biocompatibility of TiO_2 upon coating with Y_2O_3, as a potential result of the antioxidant coating layer. Overall, the synthesised nanomaterials show improved optical properties and biocompatibility and reduced photocatalytic activity, thus highlighting the potential benefits of the inclusion of these materials in sunscreen products for UV filtration.

The findings of this thesis highlight the complexity of the underlying toxic mechanism of nanoparticles in living organisms. As such, additional techniques should be used in conjunction with the MTS tetrazolium salt assay in order to elucidate the mechanism by which these particles exert toxicity in HaCaT cells. Also, longer treatment times could be used to determine subchronic effects caused by these particles as after sunscreen application they might remain in the skin even after long periods of time. The synthesised particles reduced intracellular ROS levels, possibly due to the antioxidant behaviour of the yttria coating layer, and thus, prevented cell death due to oxidative stress. Oxidative stress has been linked to multiple diseases including cancer; hence, the synthesised particles could potentially be used as therapeutic agents.

Appendix A

Synthesis of Y_2O_3

Synthesis of Y_2O_3 via a hydrothermal method involved the precipitation of $Y(OH)_3$ through the addition of NaOH (Equation A.1) followed by the calcination of the hydroxide precursor formed (Equation A.2), as proven by their XRD patterns (Figure 4.1 (b)).

$$Y(NO_3)_3 \cdot 6H_2O\ (aq) + NaOH\ (aq) \rightarrow Y(OH)_3\ (s) \qquad (A.1)$$

$$2Y(OH)_3\ (s) \xrightarrow{\Delta} Y_2O_3\ (s) + 3H_2O \qquad (A.2)$$

As previoulsy mentioned in Section 3.2, the synthesised $Y(OH)_3$ and Y_2O_3 particles display high crystallinity as confirmed by the sharp peaks in Figure 4.1 (b).

Appendix B

X-ray Diffraction

B.1 Mean crystallite size

The mean crystallite size was calculated using Scherrer equation on the (101) anatase plane as following [129]:

$$P = \frac{0.9\,\lambda}{\beta\cos\theta} \qquad \text{(B.1)}$$

Where λ is the CuKα wavelength (1.54059 Å), β is the FWHM (full width at half maximum) (minus the broadening caused by the silicon substrate and instrument which was measured to be 0.142) and θ (in radians) is the Bragg angle at (101).

B.2 X-ray diffraction pattern

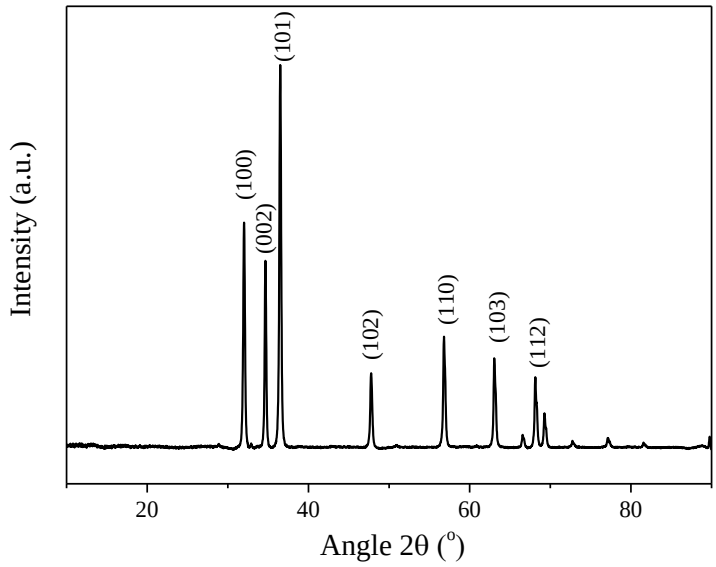

Figure B.1: X-ray diffraction pattern of ZnO.

Appendix C

Electron Microscopy

C.1 Scanning Transmission Electron Microscopy (STEM)

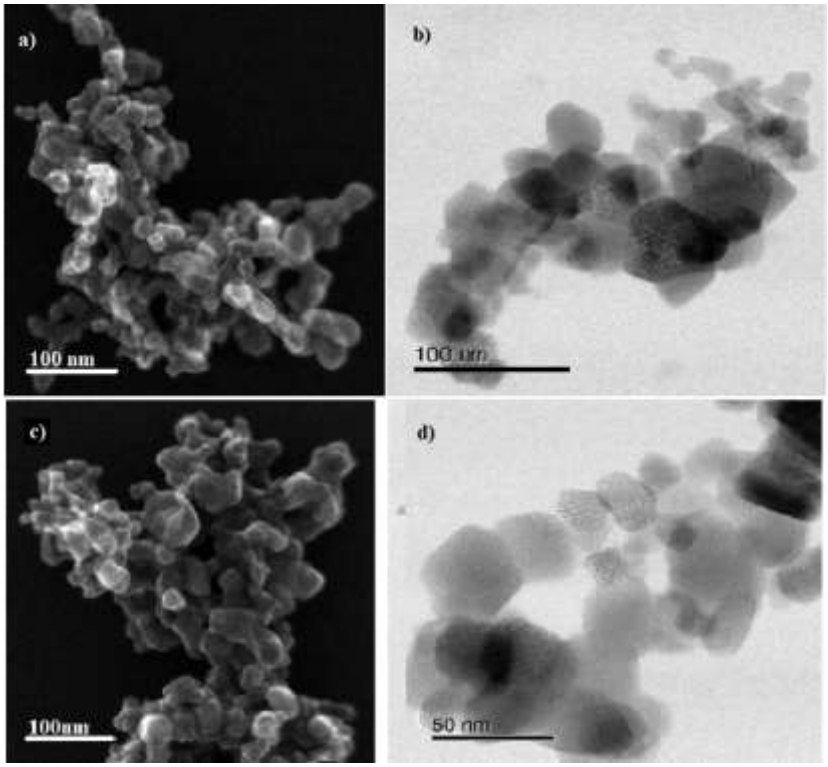

Figure C.1: STEM micrographs of (a), (b) TiO_2 and (c), (d) annealed TiO_2.

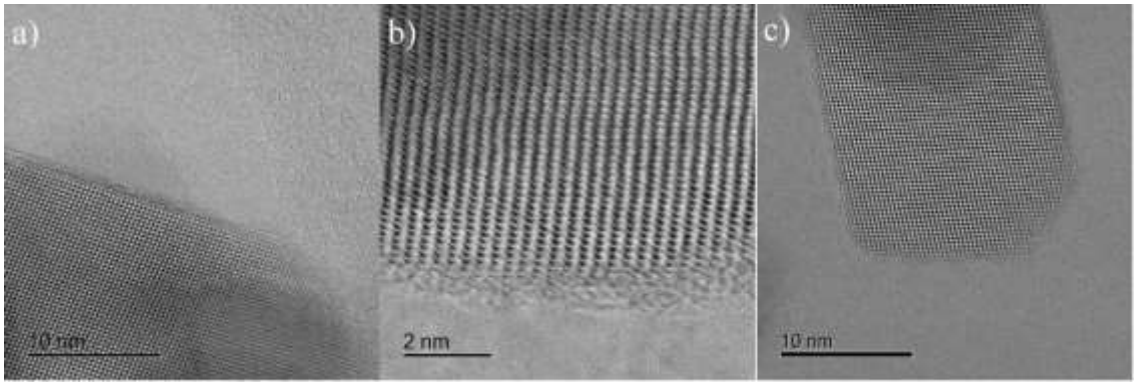

Figure C.2: TEM micrographs of TiO_2@$Y(OH)_3$ at (a) 5 wt%, (b) 10 wt% and (c) 25 wt% Y content.

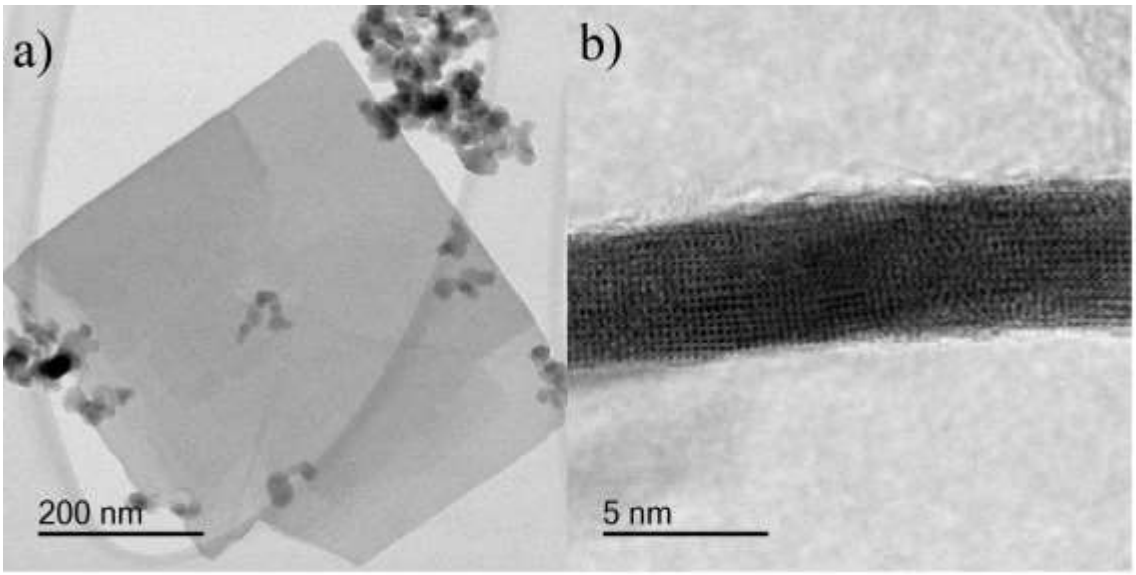

Figure C.3: Sheet and rod particles present in (a) TiO_2@$Y(OH)_3$ and (b) TiO_2@Y_2O_3 at 10 wt% Y content.

C.2 Energy-dispersive X-ray Spectroscopy (EDS)

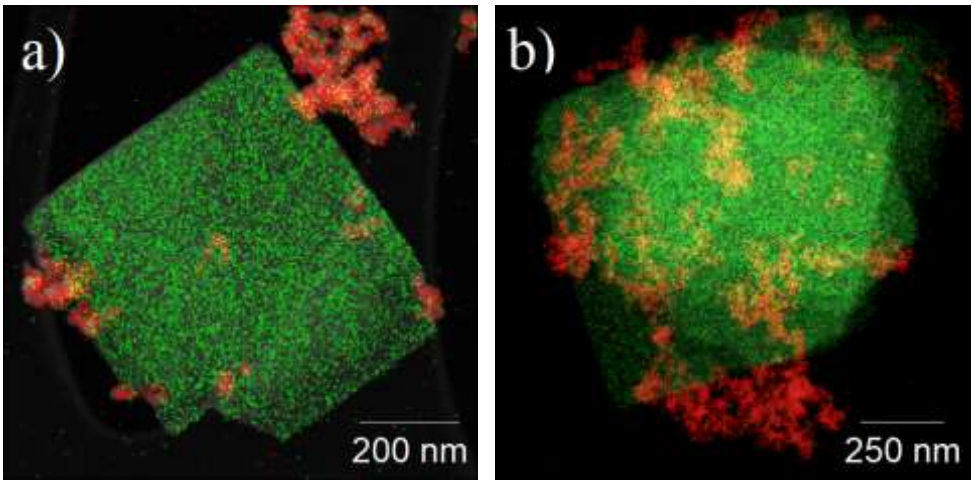

Figure C.4: EDS mapping of (a) TiO_2@$Y(OH)_3$ 10 wt% and (b) TiO_2@Y_2O_3 25 wt% Y content. Red and green regions correspond to Ti and Y atoms, respectively.

C.3 Size distribution

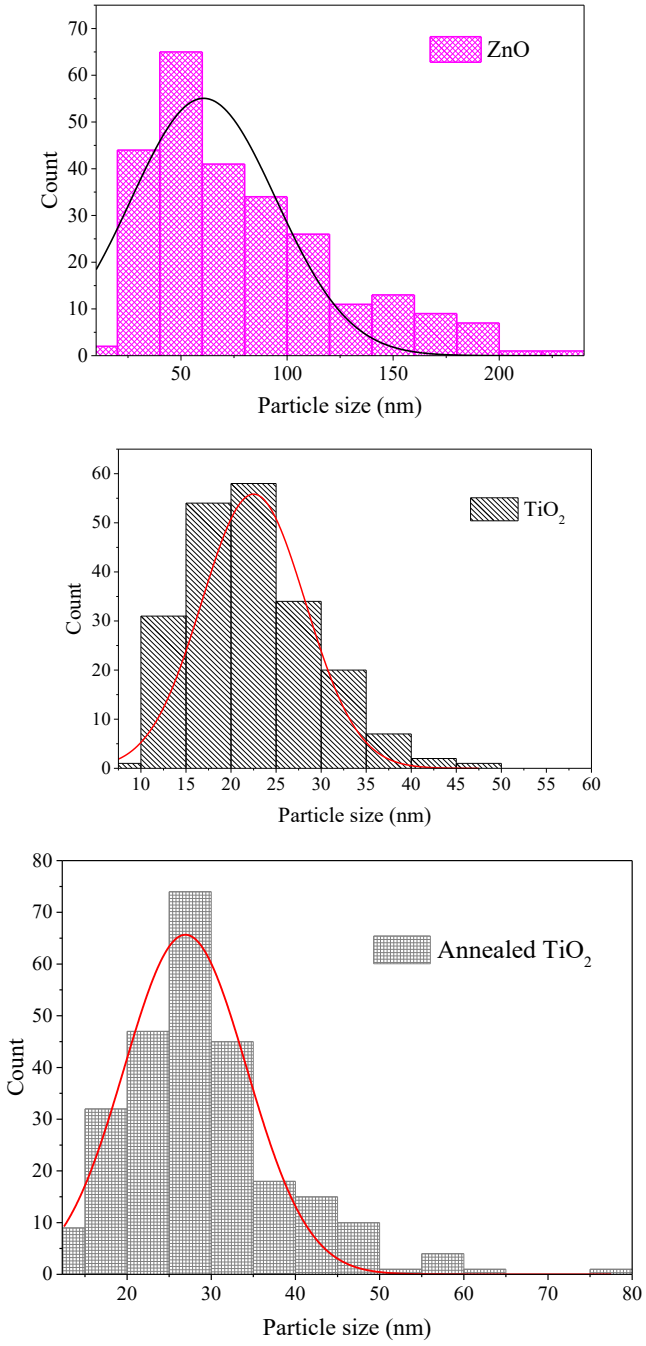

Figure C.5: Particle size distribution histograms of commercial ZnO, TiO_2 and annealed TiO_2 (top to bottom) as measured from TEM micrographs.

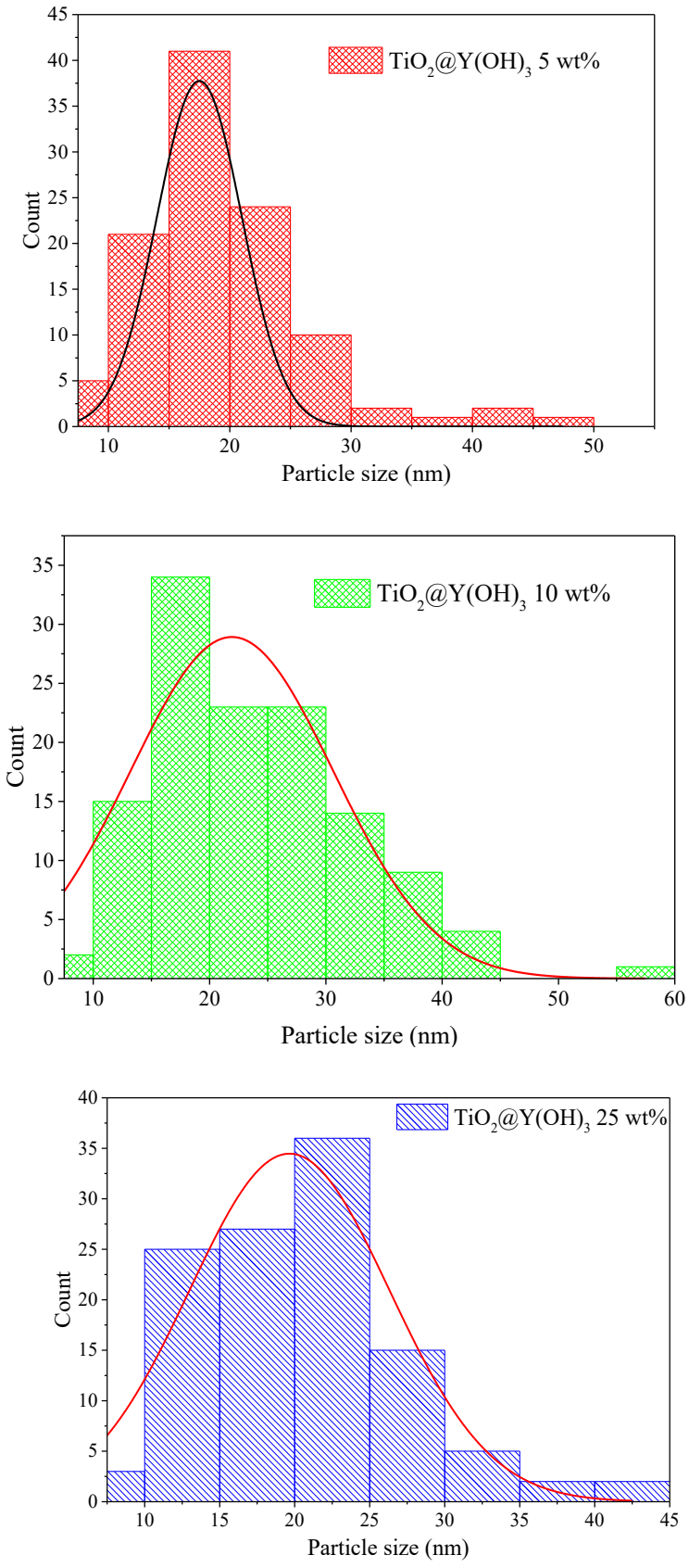

Figure C.6: Particle size distribution histograms of TiO_2@$Y(OH)_3$ 5, 10 and 25 wt% (top to bottom) as measured from TEM micrographs.

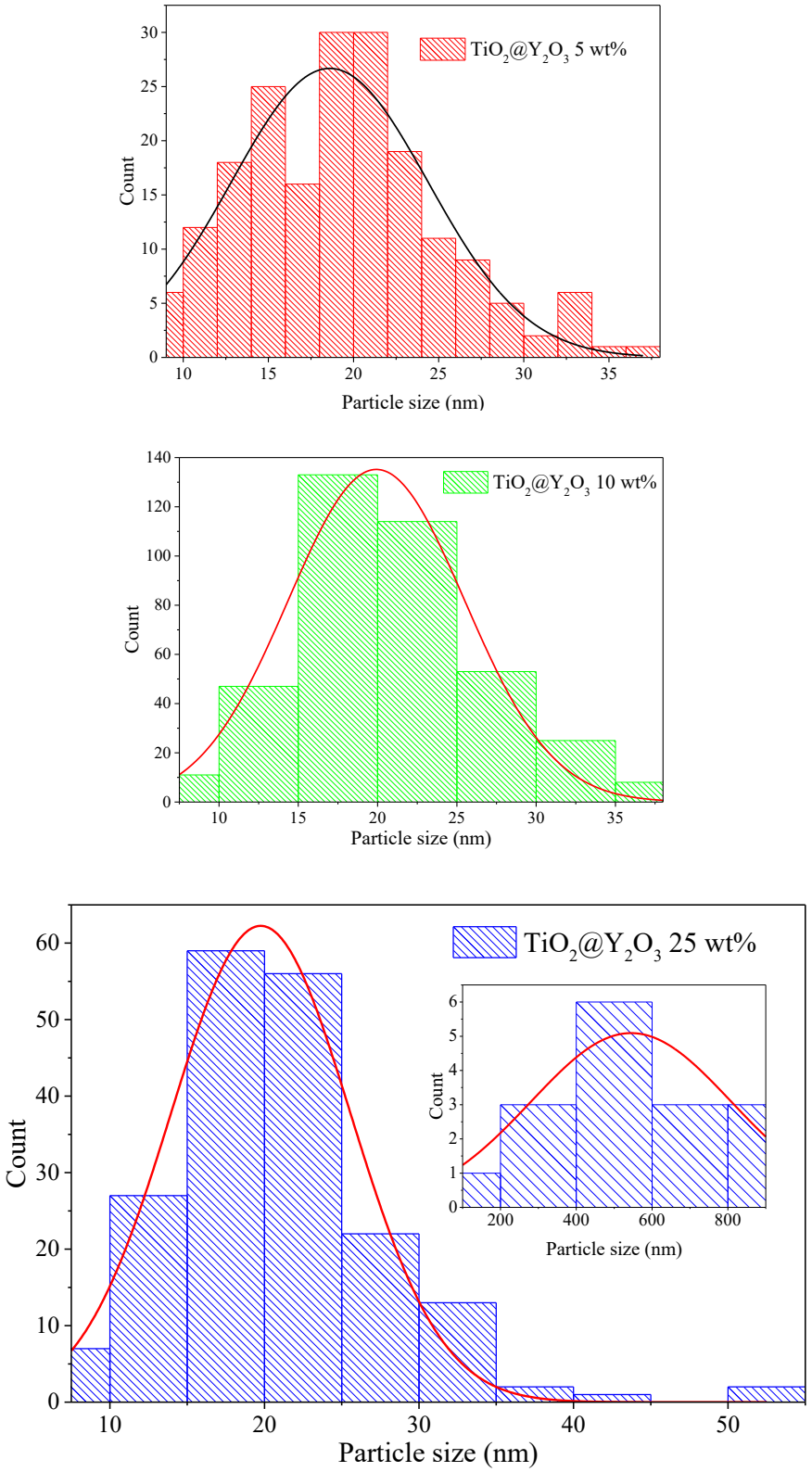

Figure C.7: Particle size distribution histograms of $TiO_2@Y_2O_3$ 5, 10 and 25 wt% (top to bottom) as measured from TEM micrographs. Inset in $TiO_2@Y_2O_3$ 25 wt% represents the size distribution of the plate like particles formed during the synthesis process with an average size of (500 ± 200) nm.

Appendix D

Optical Properties

D.1 Rayleigh scattering

The absorption and scattering of nanoparticles in suspension primarily depend on the size of the nanomaterial and the wavelength (λ) of the incident radiation [196]. Scattering due to nanoparticles less than a tenth in diameter (d) of λ, is governed by the Rayleigh scattering regime (Equation D.1).

$$I = I_0 \frac{1 + \cos^2\theta}{2R^2} \left(\frac{2\pi}{\lambda}\right)^4 \left(\frac{n^2 - 1}{n^2 + 2}\right)^2 \left(\frac{d}{2}\right)^6 \quad \text{(D.1)}$$

Where I and I_0 are the intensity and initial intensity of the scattered light, respectively, θ the scattering angle of the scattered light, R the distance to the scattering particle and n the refractive index. The intensity of the scattered light (I) can be approximated to $1 \cdot \lambda^{-4}$ [197]. Hence, smaller particles scatter shorter wavelengths more intensely, as shown in Figure 4.9. The synthesised samples do not scatter as much visible light as pristine TiO_2, which has been determined to be larger than the coated particles (Section 4.1).

D.2 UV-vis spectroscopy

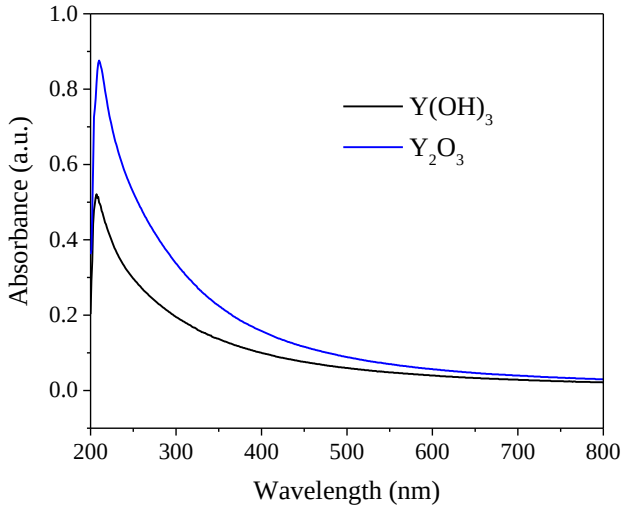

Figure D.1: UV-vis spectra of the synthesised $Y(OH)_3$ and Y_2O_3 particles suspended in ethanol.

D.3 Band gap energy (*Eg*)

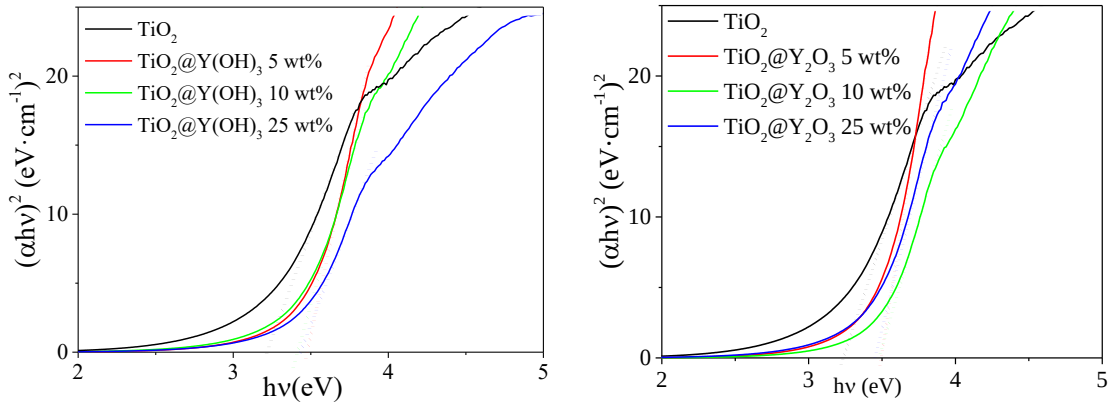

(a) (b)

Figure D.2: Tauc plot constructed from the UV-vis absorption spectrum of TiO_2 along with (a) TiO_2@$Y(OH)_3$ and (b) TiO_2@Y_2O_3 nanoparticles at varying Y content suspended in ethanol.

Appendix E

Photocatalytic activity and Langmuir-Hinshelwood Kinetics

E.1 Langmuir-Hinshelwood kinetic plots

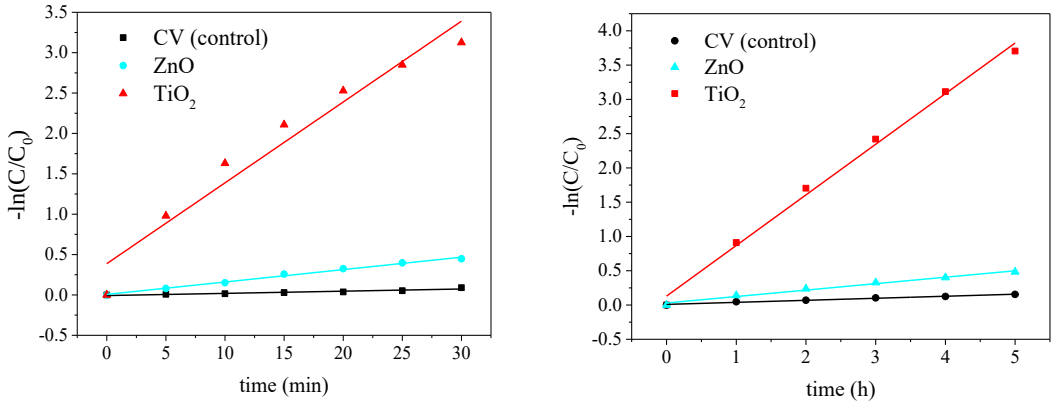

(b) (b)

Figure E.1: Kinetic plots derived from the Langmuir-Hinshelwood model for commercial TiO_2 and ZnO excited trough (a) UV radiation and (b) simulated solar radiation.

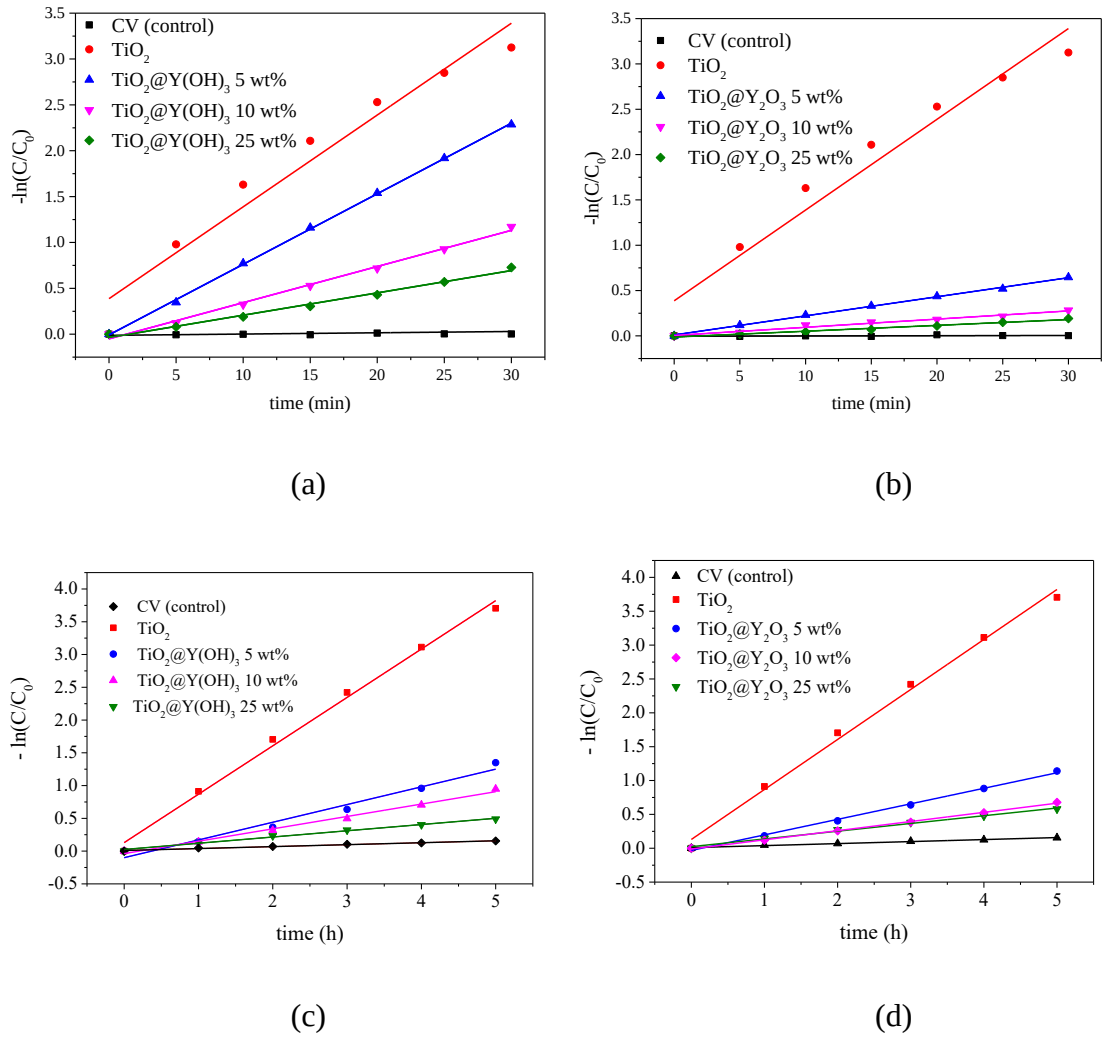

Figure E.2: Kinetic plots derived from the Langmuir-Hinshelwood model for TiO_2@$Y(OH)_3$ and TiO_2@Y_2O_3 excited under UV radiation (a) and (b), respectively, and under simulated solar radiation (c) and (d), respectively, at varying Y content.

E.2 Dye sensitisation process of TiO_2 under simulated solar radiation

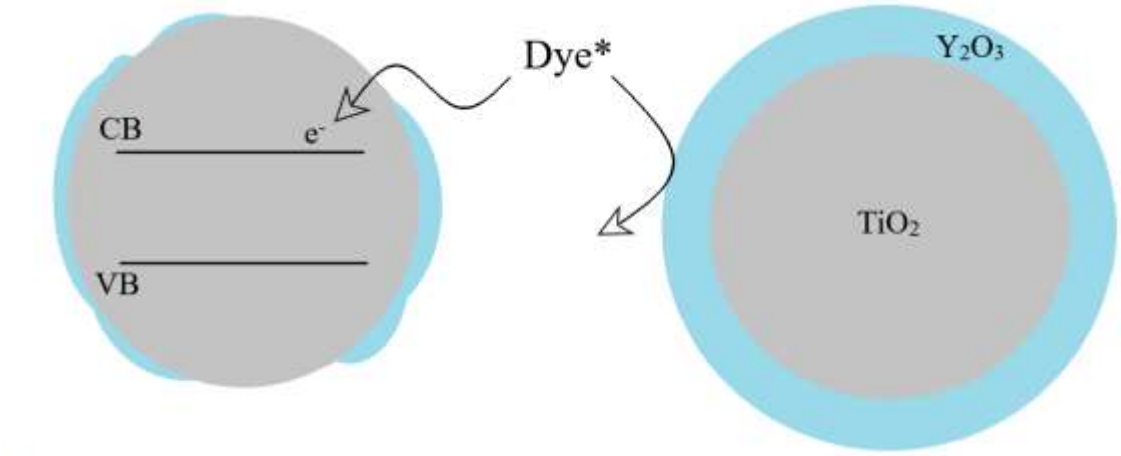

Figure E.3: Diagram of the dye sensitisation process of TiO_2 (grey) at varying Y_2O_3 (blue) coating thickness.

$$Dye + h\nu \rightarrow dye^* \quad \text{(E.1)}$$

$$TiO_2 + dye^* \rightarrow TiO_2\,(e^-) + {}^{\bullet}dye^+ \quad \text{(E.2)}$$

$$O_2 + TiO_2\,(e^-) \rightarrow TiO_2 + {}^{\bullet}O_2^- \quad \text{(E.3)}$$

$${}^{\bullet}O_2^- + H_2O \rightarrow {}^{\bullet}HO_2 + OH^- \quad \text{(E.4)}$$

$${}^{\bullet}HO_2 + H_2O + TiO_2\,(e^-) \rightarrow TiO_2 + H_2O_2 + OH^- \quad \text{(E.5)}$$

$$H_2O_2 + TiO_2\,(e^-) \rightarrow TiO_2 + OH^- + {}^{\bullet}OH \quad \text{(E.6)}$$

Appendix F

Cell optimisation

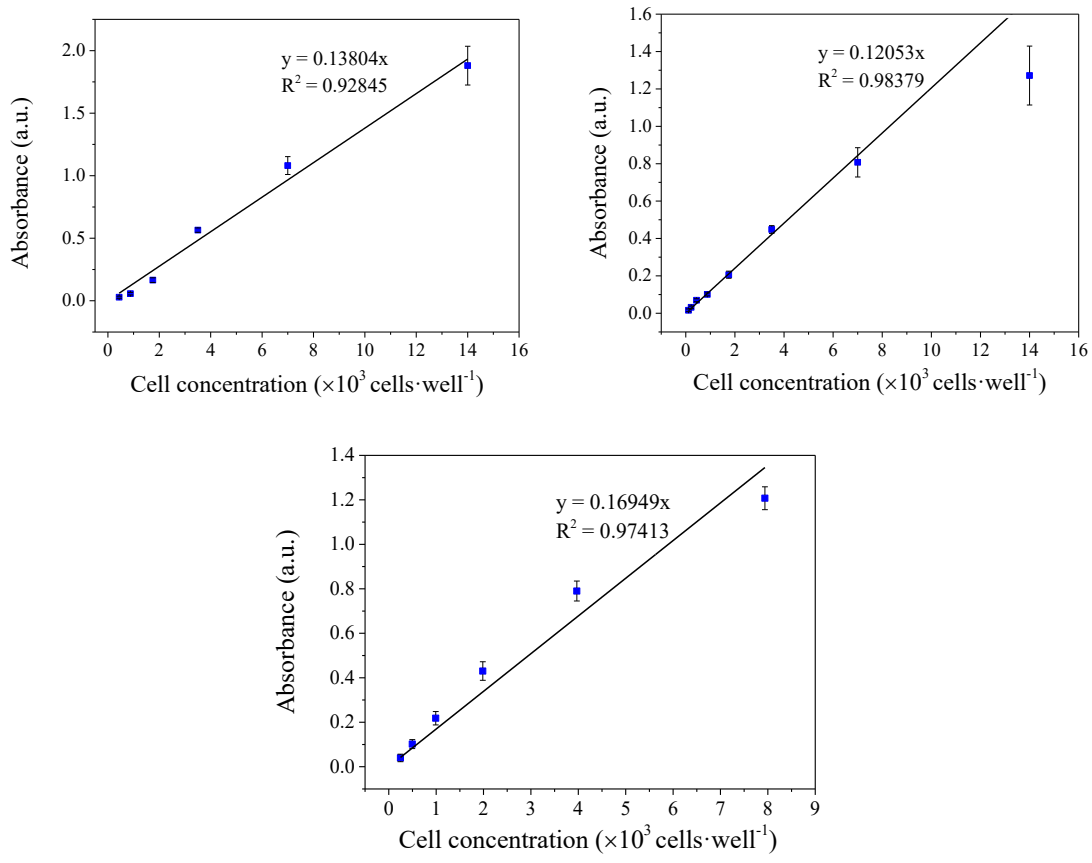

Figure F.1: 48 hour cell optimisation.

Appendix G

Chamber set up

Figure G.1: Chamber used to assess the toxicity of TiO_2 based nanoparticles under simulated solar radiation.

Appendix H

Toxicity mechanism of ZnO and TiO_2

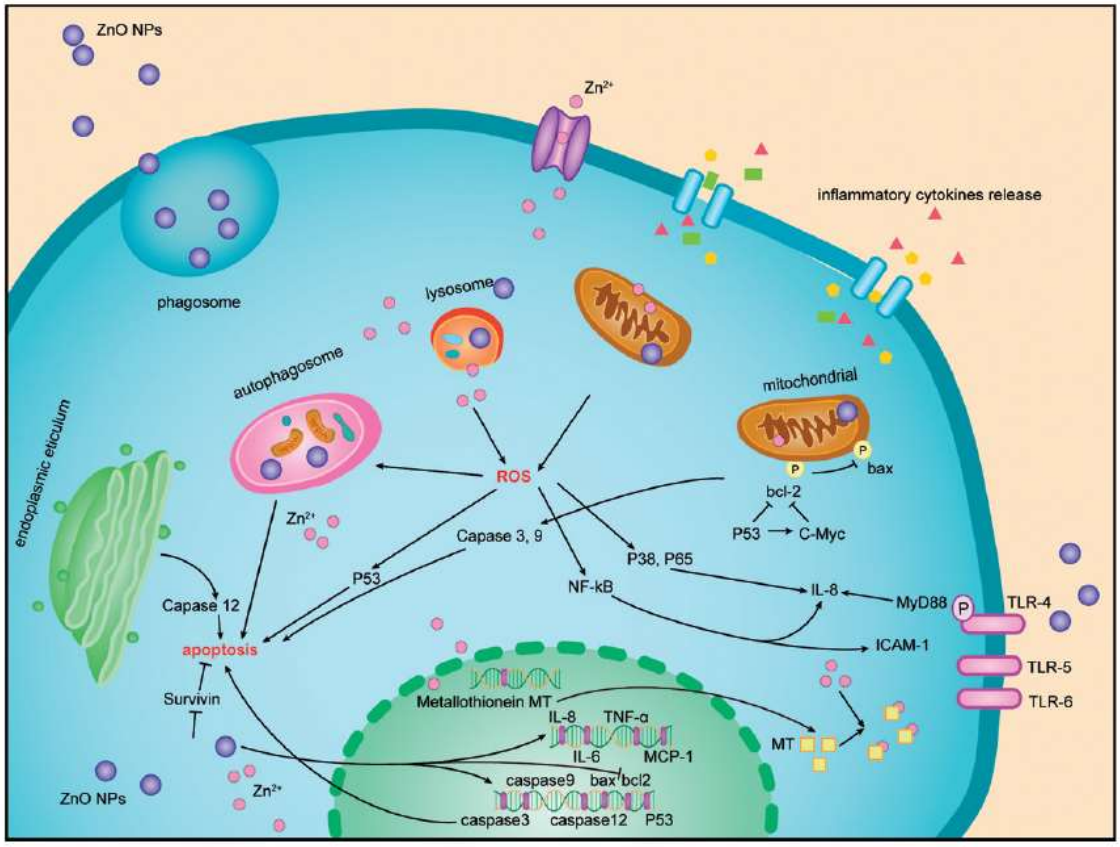

Figure H.1: Toxic mechanism of ZnO in cells. Figure reproduced from Liu *et al.* (2016) [69].

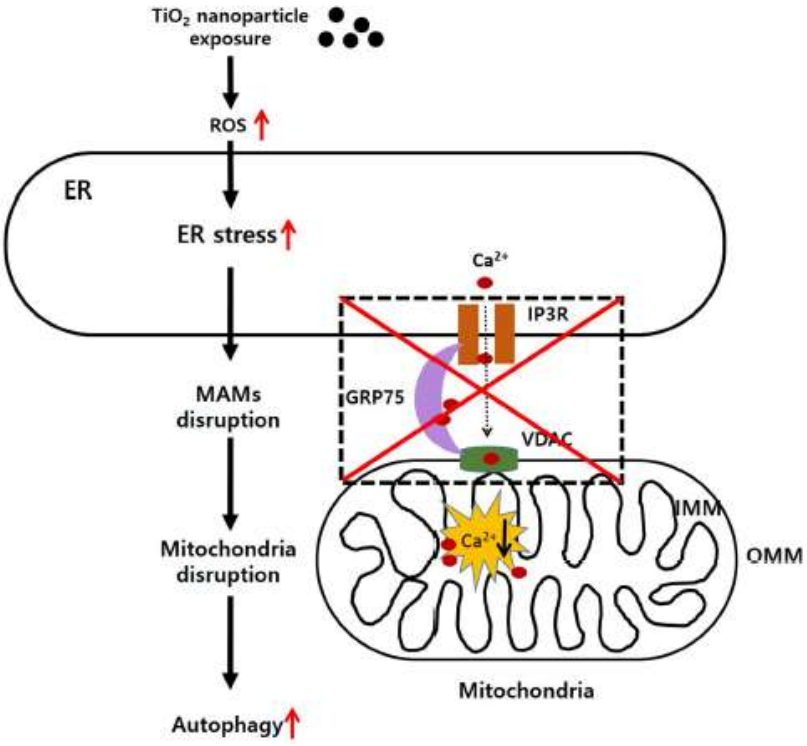

Figure H.2: Schematic toxic mechanism of TiO_2 in human bronchial epithelial cells in the absence of UV light. Figure reproduced from Yu *et al.* (2015) [174].

References

1. Cassarett, L.J., Doull, J. *Toxicology: the basic science of poisons*. Eighth Edition ed. 2013: McGraw-Hill Education. Editor^Editors
2. Annangi, B., L. Rubio, M. Alaraby, J. Bach, R. Marcos,A. Hernández *Acute and long-term in vitro effects of zinc oxide nanoparticles.* Archives of Toxicology, 2016, **90**(9): 2201-2213.
3. Mihranyan, A., Ferraz, N., Strømme, M. *Current status and future prospects of nanotechnology in cosmetics.* Progress in Materials Science, 2012, **57**(5): 875-910.
4. Damiani, E., Ullrich, S. E. *Understanding the connection between platelet-activating factor, a UV-induced lipid mediator of inflammation, immune suppression and skin cancer.* Progress in Lipid Research, 2016, **63**: 14-27.
5. D'Orazio, J., Jarrett, S., Amaro-Ortiz, A., Scott, T. *UV radiation and the skin.* International Journal of Molecular Sciences, 2013, **14**(6): 12222-12248.
6. Gilbert, E., Pirot, F., Bertholle, V., Roussel, L., Falson, F., Padois, K. *Commonly used UV filter toxicity on biological functions: Review of last decade studies.* International Journal of Cosmetic Science, 2013, **35**(3): 208-219.
7. Lucas, R.M., Yazar, S., Young, A. R., Norval, M., de Gruijl, F. R., Takizawa, Y., Rhodes, L. E., Sinclair, C. A., Neale, R. E. *Human health in relation to exposure to solar ultraviolet radiation under changing stratospheric ozone and climate.* Photochemical & photobiological sciences : Official journal of the European Photochemistry Association and the European Society for Photobiology, 2019, **18**(3): 641-680.
8. Lucas R., M.T., Smith W., Armstrong B. *Solar Ultraviolet Radiation: global burden of disease from solar ultraviolet radiation.* WHO, Geneva, 2006.
9. Cancer Council, A. *Skin cancer*. 2017 Last update: 13/04/2017: 11/08/2017].
10. TGA *Australian regulatory guidelines for sunscreens.* 2016.
11. Manaia, E.B., Kaminski, R. C. K., Corrêa, M. A., Chiavacci, L. A. *Inorganic UV filters.* Brazilian Journal of Pharmaceutical Sciences, 2013, **49**(2): 201-209.

12. Wharton, M., Geary, M., O'Connor, N., Murphy, B. *A rapid High Performance Liquid Chromatographic (HPLC) method for the simultaneous determination of seven UV filters found in sunscreen and cosmetics.* International Journal of Cosmetic Science, 2011, **33**(2): 164-170.
13. Shaath, N.A. *Ultraviolet filters.* Photochemical and Photobiological Sciences, 2010, **9**(4): 464-469.
14. Leong, K., Ching, S., Saravanan, P.,Ibrahim, S. (2016) *Light Driven Nanomaterials for Removal of Agricultural Toxins.* In: S. Ranjan, Dasgupta, N., Lichtfouse, E. (eds) *Nanoscience in Food and Agriculture 3. Sustainable Agriculture Reviews*, vol. 23. Springer, Cham 2017, pp. 225-242.
15. Fujishima, A., Rao, T. N., Tryk, D. A. *Titanium dioxide photocatalysis.* Journal of Photochemistry and Photobiology C: Photochemistry Reviews, 2000, **1**(1): 1-21.
16. Clark, A., Zhu, A., Sun, K., Petty, H. R. *Cerium oxide and platinum nanoparticles protect cells from oxidant-mediated apoptosis.* Journal of Nanoparticle Research, 2011, **13**(10): 5547-5555.
17. Saeidnia, S., Abdollahi, M. *Toxicological and pharmacological concerns on oxidative stress and related diseases.* Toxicology and Applied Pharmacology, 2013, **273**(3): 442-455.
18. Yusa, V., Millet, M., Coscolla, C., Roca, M. *Analytical methods for human biomonitoring of pesticides. A review.* Analytica Chimica Acta, 2015, **891**: 15-31.
19. Barker, P.J., Branch, A. *The interaction of modern sunscreen formulations with surface coatings.* Progress in Organic Coatings, 2008, **62**(3): 313-320.
20. Tiano, L., Armeni, T., Venditti, E., Barucca, G., Mincarelli, L., Damiani, E. *Modified TiO2 particles differentially affect human skin fibroblasts exposed to UVA light.* Free Radical Biology and Medicine, 2010, **49**(3): 408-415.
21. Dechsakulthorn, F., Hayes, A., Bakand, S., Joeng, L., Winder, C. *In vitro cytotoxicity assessment of selected nanoparticles using human skin fibroblasts.* Japanese Society for Alternatives to Animal Experiments, 2008, **AATEX 14**(Special Issue): 397-400.
22. Kim, K., Kim, Y. W., Lim, S. K., Roh, T. H., Bang, D. Y., Choi, S. M., Lim, D. S., Kim, Y. J., Baek, S., Kim, M., Seo, H., Kim, M., Kim, H. S., Lee, J. Y.,

Kacew, S., Lee, B. *Risk assessment of zinc oxide, a cosmetic ingredient used as a UV filter of sunscreens.* Journal of Toxicology and Environmental Health - Part B: Critical Reviews, 2017, **20**(3): 155-182.

23. Soh, Y.C., Roddick, F., Van Leeuwen, J. *The future of water in Australia: The potential effects of climate change and ozone depletion on Australian water quality, quantity and treatability.* Environmentalist, 2008, **28**(2): 158-165.
24. Séite, S., Moyal, D., Richard, S., De Rigal, J., Lévêque, J. L., Hourseau, C., Fourtanier, A. *Mexoryl® SX: A broad absorption UVA filter protects human skin from the effects of repeated suberythemal doses of UVA.* Journal of Photochemistry and Photobiology B: Biology, 1998, **44**(1): 69-76.
25. Truffault, L., Ta, M. T., Devers, T., Konstantinov, K., Harel, V., Simmonard, C., Andreazza, C., Nevirkovets, I. P., Pineau, A., Veron, O., Blondeau, J. P. *Application of nanostructured Ca doped CeO_2 for ultraviolet filtration.* Materials Research Bulletin, 2010, **45**(5): 527-535.
26. Uhoda, E., Piérard, G. E. *From sun to earth.* Revue Medicale de Liege, 2005, **60**(SUPPL. 1): 2-9.
27. Gupta, S.C.H., D.; Patchva, S.; Park, B.; Koh, W.; Aggarwal, B. B. *Upsides and downsides of reactive oxygen species for Cancer: The roles of reactive oxygen species in tumorigenesis, prevention, and therapy.* Antioxidants and Redox Signaling, 2012, **16**(11): 1295-1322.
28. Hayyan, M., Hashim, M. A., Alnashef, I. M. *Superoxide Ion: Generation and Chemical Implications.* Chemical Reviews, 2016, **116**(5): 3029-3085.
29. McLafferty, E., Hendry, C., Alistair, F. *The integumentary system: anatomy, physiology and function of skin.* Nursing standard (Royal College of Nursing (Great Britain) : 1987), 2012, **27**(3): 35-42.
30. Terenetskaya, I., Orlova, T. *Variability of solar UV-B irradiance: In situ monitoring and model calculation of the vitamin D synthetic capacity of sunlight.* International Journal of Remote Sensing, 2011, **32**(21): 6205-6218.
31. Reichrath, J., Reichrath, S. *Hope and challenge: The importance of ultraviolet (UV) radiation for cutaneous Vitamin D synthesis and skin cancer.* Scandinavian Journal of Clinical and Laboratory Investigation, 2012, **72**(SUPPL. 243): 112-119.

32. American Academy of Dermatology. *The layers of your skin*. 2017: 05/09/2017].
33. Holick, M.F., Maclaughlin, J. A., Clark, M. B., Holick, S. A., Potts Jr, J. T., Anderson, R. R., Blank, I. H., Parrish, J. A., Elias, P. *Photosynthesis of previtamin D3 in human skin and the physiologic consequences.* Science, 1980, **210**(4466): 203-205.
34. Holick, M.F., Maclaughlin, J. A., Doppelt, S. H. *Regulation of cutaneous previtamin D3 photosynthesis in man: Skin pigment is not an essential regulator.* Science, 1981, **211**(4482): 590-593.
35. Holick, M.F. *The cutaneous photosynthesis of previtamin D3: A unique photoendocrine system.* Journal of Investigative Dermatology, 1981, **77**(1): 51-58.
36. Lucas, R.M., Byrne, S. N., Correale, J., Ilschner, S., Hart, P. H. *Ultraviolet radiation, vitamin D and multiple sclerosis.* Neurodegenerative disease management, 2015, **5**(5): 413-424.
37. Jablonski, N.G., Chaplin, G. *The roles of vitamin D and cutaneous vitamin D production in human evolution and health.* International Journal of Paleopathology, 2018, **23**: 54-59.
38. Diffey, B.L. *Solar ultraviolet radiation effects on biological systems.* Physics in Medicine and Biology, 1991, **36**(3): 299-328,001.
39. Panich, U., Sittithumcharee, G., Rathviboon, N., Jirawatnotai, S. *Ultraviolet radiation-induced skin aging: The role of DNA damage and oxidative stress in epidermal stem cell damage mediated skin aging.* Stem Cells International, 2016, **2016**,7370642.
40. Bernstein, E.F., D.B. Brown, F. Urbach, D. Forbes, M. Del Monaco, M. Wu, S.D. Katchman,J. Uitto *Ultraviolet radiation activates the human elastin promoter in transgenic mice: A novel in vivo and in vitro model of cutaneous photoaging.* Journal of Investigative Dermatology, 1995, **105**(2): 269-273.
41. Koken, P.J.M., Willems, B. A. T., Vrieze, O. J., Frick, R. A. *Modelling the ozone depletion, UV radiation and skin cancer rates for Australia.* Environmetrics, 1998, **9**(1): 15-30.

42. Morlando, A.C., D.; Devers, T. and Konstantinov, K. *Titanium doped tin dioxide as potential UV filter with low photocatalytic activity for sunscreen products.* Materials Letters, 2016, **171**: 289-292.
43. Ouhtit, A., Nakazawa, H., Armstrong, B. K., Kricker, A., Tan, E., Yamasaki, H., English, D. R. *UV-radiation-specific p53 mutation frequency in normal skin as a predictor of risk of basal cell carcinoma.* Journal of the National Cancer Institute, 1998, **90**(7): 523-531.
44. The Cancer Council Australia *Skin cancer and outdoor work: A guide for employers.* 2007.
45. Rigel, D.S. *Cutaneous ultraviolet exposure and its relationship to the development of skin cancer.* Journal of the American Academy of Dermatology, 2008, **58**(5 SUPPL. 2): S129-S132.
46. Tyagi, N., Srivastava, S. K., Arora, S., Omar, Y., Ijaz, Z. M., Al-Ghadhban, A., Deshmukh, S. K., Carter, J. E., Singh, A. P., Singh, S. *Comparative analysis of the relative potential of silver, Zinc-oxide and titanium-dioxide nanoparticles against UVB-induced DNA damage for the prevention of skin carcinogenesis.* Cancer Letters, 2016, **383**(1): 53-61.
47. TEMIS. *UV radiation monitoring archive*. [Accessed: 30/04/2019]; Available from: http://www.temis.nl/uvradiation/UVarchive.html.
48. Veronovski, N., Lešnik, M., Lubej, A., Verhovšek, D. *Surface treated titanium dioxide nanoparticles as inorganic UV filters in sunscreen products.* Acta Chimica Slovenica, 2014, **61**(3): 595-600.
49. Juliano, C.,G. Magrini *Cosmetic Ingredients as Emerging Pollutants of Environmental and Health Concern. A Mini-Review.* Cosmetics, 2017, **4**(2): 11.
50. Sohn, M., Herzog, B., Osterwalder, U., Imanidis, G. *Calculation of the sun protection factor of sunscreens with different vehicles using measured film thickness distribution - Comparison with the SPF in vitro.* Journal of Photochemistry and Photobiology B: Biology, 2016, **159**: 74-81.
51. El-Boury, S., Couteau, C., Boulande, L., Paparis, E., Coiffard, L. J. M. *Effect of the combination of organic and inorganic filters on the Sun Protection Factor (SPF) determined by in vitro method.* International Journal of Pharmaceutics, 2007, **340**(1-2): 1-5.

52. Damiani, E., Astolfi, P., Giesinger, J., Ehlis, T., Herzog, B., Greci, L., Baschong, W. *Assessment of the photo-degradation of UV-filters and radical-induced peroxidation in cosmetic sunscreen formulations.* Free Radical Research, 2010, **44**(3): 304-312.

53. Young, A.R., Claveau, J., Rossi, A. B. *Ultraviolet radiation and the skin: Photobiology and sunscreen photoprotection.* Journal of the American Academy of Dermatology, 2017, **76**(3): S100-S109.

54. Schalka, S., dos Reis, V. M. S., Cucé, L. C. *The influence of the amount of sunscreen applied and its sun protection factor (SPF): Evaluation of two sunscreens including the same ingredients at different concentrations.* Photodermatology Photoimmunology and Photomedicine, 2009, **25**(4): 175-180.

55. Boutard, T.R., B.; Couteau, C.; Tomasoni, C.; Simonnard, C.; Jacquot, C.; Coiffard, L. J. M.; Konstantinov, K.; Devers, T. and Roussakis, C. *Comparison of photoprotection efficiency and antiproliferative activity of ZnO commercial sunscreens and CeO_2.* Materials Letters, 2013, **108**: 13-16.

56. Abid, A.R., B. Marciniak, T. Pędziński,M. Shahid *Photo-stability and photo-sensitizing characterization of selected sunscreens' ingredients.* Journal of Photochemistry and Photobiology A: Chemistry, 2017, **332**: 241-250.

57. Afonso, S., K. Horita, J.P. Sousa E Silva, I.F. Almeida, M.H. Amaral, P.A. Lobão, P.C. Costa, M.S. Miranda, J.C.G. Esteves Da Silva,J.M. Sousa Lobo *Photodegradation of avobenzone: Stabilization effect of antioxidants.* Journal of Photochemistry and Photobiology B: Biology, 2014, **140**: 36-40.

58. Mturi, G.J., Martincigh, B. S. *Photostability of the sunscreening agent 4-tert-butyl-4'-methoxydibenzoylmethane (avobenzone) in solvents of different polarity and proticity.* Journal of Photochemistry and Photobiology A: Chemistry, 2008, **200**(2-3): 410-420.

59. He, T., Tsui, M. M. P., Tan, C. J., Ma, C. Y., Yiu, S. K. F., Wang, L. H., Chen, T. H., Fan, T. Y., Lam, P. K. S., Murphy, M. B. *Toxicological effects of two organic ultraviolet filters and a related commercial sunscreen product in adult corals.* Environmental Pollution, 2019: 462-471.

60. Danovaro, R., Bongiorni, L., Corinaldesi, C., Giovannelli, D.,Damiani, E., Astolfi, P., Greci, L., Pusceddu, A. *Sunscreens cause coral bleaching by*

promoting viral infections. Environmental Health Perspectives, 2008, **116**(4): 441-447.

61. Wong, T., Orton, D. *Sunscreen allergy and its investigation.* Clinics in Dermatology, 2011, **29**(3): 306-310.
62. Karlsson, I., Hillerström, L., Stenfeldt, A. L., Mårtensson, J., Börje, A. *Photodegradation of dibenzoylmethanes: Potential cause of photocontact allergy to sunscreens.* Chemical Research in Toxicology, 2009, **22**(11): 1881-1892.
63. Rodine-Hardy, K., Pathalam, N. *American sunscreen may damage coral reefs — unlike sunscreen you can buy overseas. Here's why.*, in *The Washington POst*. 2019.
64. Hanaor, D.A.H., Sorrell, Charles C. *Review of the anatase to rutile phase transformation.* Journal of Materials Science, 2011, **46**(4): 855-874.
65. Tran, D.T., Salmon, R. *Potential photocarcinogenic effects of nanoparticle sunscreens.* Australasian Journal of Dermatology, 2011, **52**(1): 1-6.
66. Ma, X., Wu, Y., Lv, Y., Zhu, Y. *Correlation effects on lattice relaxation and electronic structure of zno within the GGA+ U formalism.* Journal of Physical Chemistry C, 2013, **117**(49): 26029-26039.
67. Hariharan, C. *Photocatalytic degradation of organic contaminants in water by ZnO nanoparticles: Revisited.* Applied Catalysis A: General, 2006, **304**(1-2): 55-61.
68. Lee, K.M., Lai, C. W., Ngai, K. S., Juan, J. C. *Recent developments of zinc oxide based photocatalyst in water treatment technology: A review.* Water Research, 2016, **88**: 428-448.
69. Liu, J., Feng, X., Wei, L., Chen, L., Song, B., Shao, L. *The toxicology of ion-shedding zinc oxide nanoparticles.* Critical Reviews in Toxicology, 2016, **46**(4): 348-384.
70. Mudunkotuwa, I.A., Rupasinghe, T., Wu, C. M., Grassian, V. H. *Dissolution of ZnO nanoparticles at circumneutral pH: A study of size effects in the presence and absence of citric acid.* Langmuir, 2012, **28**(1): 396-403.
71. Shi, H., Magaye, R., Castranova, V., Zhao, J. *Titanium dioxide nanoparticles: A review of current toxicological data.* Particle and Fibre Toxicology, 2013, **10**(1),15.

72. Wright, C., Iyer, A. K. V., Wang, L., Wu, N., Yakisich, J. S., Rojanasakul, Y., Azad, N. *Effects of titanium dioxide nanoparticles on human keratinocytes.* Drug and Chemical Toxicology, 2017, **40**(1): 90-100.

73. Crosera, M., Prodi, A., Mauro, M., Pelin, M., Florio, C., Bellomo, F., Adami, G., Apostoli, P., De Palma, G., Bovenzi, M., Campanini, M., Filon, F. L. *Titanium dioxide nanoparticle penetration into the skin and effects on HaCaT cells.* International Journal of Environmental Research and Public Health, 2015, **12**(8): 9282-9297.

74. Levina, A., Ismagilov, Z., Repkova, M., Shatskaya, N., Shikina, N., Tusikov, F., Zarytova, V. *Nanocomposites consisting of titanium dioxide nanoparticles and oligonucleotides.* Journal of Nanoscience and Nanotechnology, 2012, **12**(3): 1812-1820.

75. Zhao, B., Wang, J., Li, H., Xu, Y., Yu, H., Jia, X., Zhang, X., Hao, Y. *Solar-to-Electric Performance Enhancement by Titanium Oxide Nanoparticles Coated with Porous Yttrium Oxide for Dye-Sensitized Solar Cells.* ACS Sustainable Chemistry and Engineering, 2015, **3**(7): 1518-1525.

76. Zhigalina, V.G., Lizunova, A. A., Sulyanov, S. N., Ivanov, V. V., Kiselev, N. A. *Dimensional and phase characteristics of aluminum oxide and titanium dioxide nanoparticles.* Nanotechnologies in Russia, 2014, **9**(9-10): 492-501.

77. TGA *Literature Review on the safety of titanium dioxide and zinc oxide nanoparticles in sunscreens.* 2016.

78. Thamaphat, K., Limsuwan, P., Ngotawornchai, B. *Phase characterization of TiO2 powder by XRD and TEM\n*. Vol. 42. 2008. 357-361. Editor^Editors

79. Ahmad, M.I., S.S. Bhattacharya, C. Fasel,H. Hahn *Effect of gas flow rates on the anatase-rutile transformation temperature of nanocrystalline tio 2 synthesised by chemical vapour synthesis.* Journal of Nanoscience and Nanotechnology, 2009, **9**(9): 5572-5577.

80. Wetchakun, N., Incessungvorn, B., Wetchakun, K., Phanichphant, S. *Influence of calcination temperature on anatase to rutile phase transformation in TiO 2 nanoparticles synthesized by the modified sol-gel method.* Materials Letters, 2012, **82**: 195-198.

81. PaveMaintenance. *Titanium Dioxide (TiO_2) Photocatalysis in Concrete*. 29 March 2018]; Available from: http://pavemaintenance.wikispaces.com/tio2+photocatalys+-+shannon.
82. Yin, J.J., Liu, J., Ehrenshaft, M., Roberts, J. E., Fu, P. P., Mason, R. P., Zhao, B. *Phototoxicity of nano titanium dioxides in HaCaT keratinocytes-Generation of reactive oxygen species and cell damage.* Toxicology and Applied Pharmacology, 2012, **263**(1): 81-88.
83. Behnajady, M.A., Modirshahla, N., Shokri, M., Elham, H., Zeininezhad, A. *The effect of particle size and crystal structure of titanium dioxide nanoparticles on the photocatalytic properties.* Journal of Environmental Science and Health - Part A Toxic/Hazardous Substances and Environmental Engineering, 2008, **43**(5): 460-467.
84. Linsebigler, A.L., Lu, G., Yates, J. T., Jr. *Photocatalysis on TiO_2 Surfaces: Principles, Mechanisms, and Selected Results.* Chemical Reviews, 1995, **95**(3): 735-758.
85. Piasecka-Zelga, J., Zelga, P., Górnicz, M., Strzelczyk, P., Sójka-Ledakowicz, J. *Acute dermal toxicity and sensitization studies of novel nano-enhanced UV absorbers.* Journal of Occupational Health, 2015, **57**(3): 275-284.
86. Mielke, H., Strickland, J., Jacobs, M. N., Mehta, J. M. *Biometrical evaluation of the performance of the revised OECD Test Guideline 402 for assessing acute dermal toxicity.* Regulatory Toxicology and Pharmacology, 2017, **89**: 26-39.
87. Kim, J.S., Song, K. S., Sung, J. H., Ryu, H. R., Choi, B. G., Cho, H. S., Lee, J. K., Yu, I. J. *Genotoxicity, acute oral and dermal toxicity, eye and dermal irritation and corrosion and skin sensitisation evaluation of silver nanoparticles.* Nanotoxicology, 2013, **7**(5): 953-960.
88. Henry, M.C. *USEPA efforts in harmonization of acute toxicity test guidelines with OECD.* Journal of the American College of Toxicology, 1992, **11**(3): 285-291.
89. Nohynek, G.J., Dufour, E. K., Roberts, M. S. *Nanotechnology, cosmetics and the skin: Is there a health risk?* Skin Pharmacology and Physiology, 2008, **21**(3): 136-149.

90. Newman, M.D., Stotland, M., Ellis, J. I. *The safety of nanosized particles in titanium dioxide- and zinc oxide-based sunscreens.* Journal of the American Academy of Dermatology, 2009, **61**(4): 685-692.
91. Nohynek, G.J. *Safety of nanotechnology in sunscreens and personal care products.* Journal of Applied Cosmetology, 2011, **29**(1): 17-25.
92. Nohynek, G.J., Dufour, E. K. *Nano-sized cosmetic formulations or solid nanoparticles in sunscreens: A risk to human health?* Archives of Toxicology, 2012, **86**(7): 1063-1075.
93. Henkler, F., Tralau, T., Tentschert, J., Kneuer, C., Haase, A., Platzek, T., Luch, A., Götz, M. E. *Risk assessment of nanomaterials in cosmetics: A European union perspective.* Archives of Toxicology, 2012, **86**(11): 1641-1646.
94. Popov, A., Lademann, J., Priezzhev, A., Myllylä, R. *Interaction of sunscreen TiO_2 nanoparticles with skin and UV light: Penetration, protection, phototoxicity*. in *Optics InfoBase Conference Papers*. 2009.
95. SCCNFP *Opinion concerning Zinc Oxide.* 2003(COLIPA #S76).
96. Yin, H., Casey, P. S., McCall, M. J. *Surface modifications of ZnO nanoparticles and their cytotoxicity.* Journal of Nanoscience and Nanotechnology, 2010, **10**(11): 7565-7570.
97. Xue, C., Luo, W., Yang, X. L. *A mechanism for nano-titanium dioxide-induced cytotoxicity in HaCaT cells under UVA irradiation.* Bioscience, Biotechnology and Biochemistry, 2015, **79**(8): 1384-1390.
98. Xue, C., Li, X., Liu, G., Liu, W. *Evaluation of Mitochondrial Respiratory Chain on the Generation of Reactive Oxygen Species and Cytotoxicity in HaCaT Cells Induced by Nanosized Titanium Dioxide under UVA Irradiation.* International Journal of Toxicology, 2016, **35**(6): 644-653.
99. Bernauer, U., Chaudhry, Q., Dusinska, M., Lilienblum, W., Platzek, T., J. van Benthem, Chaudhry, Q., *Opinion of the Scientific Committee on Consumer safety (SCCS) - Revision of the opinion on the safety of the use of titanium dioxide, nano form, in cosmetic products.* Regulatory Toxicology and Pharmacology, 2015, **73**(2): 669-670.
100. Luttrell, T., Halpegamage, S., Tao, J., Kramer, A., Sutter, E., Batzill, M. *Why is anatase a better photocatalyst than rutile? - Model studies on epitaxial TiO_2 films.* Scientific Reports, 2015, **4**: 4043-4050,4043.

101. Schubert, D., Dargusch, R., Raitano, J., Chan, S. W. *Cerium and yttrium oxide nanoparticles are neuroprotective.* Biochemical and Biophysical Research Communications, 2006, **342**(1): 86-91.

102. Khaksar, M.R., Rahimifard, M., Baeeri, M., Maqbool, F., Navaei-Nigjeh, M., Hassani, S., Moeini-Nodeh, S., Kebriaeezadeh, A., Abdollahi, M. *Protective effects of cerium oxide and yttrium oxide nanoparticles on reduction of oxidative stress induced by sub-acute exposure to diazinon in the rat pancreas.* Journal of Trace Elements in Medicine and Biology, 2017, **41**: 79-90.

103. Cardillo, D., Weiss, M., Tehei, M., Devers, T., Rosenfeld, A., Konstantinov, K. *Multifunctional Fe_2O_3/CeO_2 nanocomposites for free radical scavenging ultraviolet protection.* RSC Advances, 2016, **6**(70): 65397-65402.

104. Truffault, L.W., B.; Choquenet, B.; Andreazza, C.; Simmonard, C.; Devers, T.; Konstantinov, K.; Couteau, C. and Coiffard, L. J. M. *Cerium oxide based particles as possible alternative to ZnO in sunscreens: Effect of the synthesis method on the photoprotection results.* Materials Letters, 2012, **68**: 357-360.

105. Karakoti, A., Singh, S., Dowding, J. M., Seal, S., Self, W. T. *Redox-active radical scavenging nanomaterials.* Chemical Society Reviews, 2010, **39**(11): 4422-4432.

106. Heckert, E.G., Karakoti, A. S., Seal, S., Self, W. T. *The role of cerium redox state in the SOD mimetic activity of nanoceria.* Biomaterials, 2008, **29**(18): 2705-2709.

107. Trogadas, P., Parrondo, J., Ramani, V. *CeO_2 surface oxygen vacancy concentration governs in situ free radical scavenging efficacy in polymer electrolytes.* ACS Applied Materials and Interfaces, 2012, **4**(10): 5098-5102.

108. Liu, X., Zhou, K., Wang, L., Wang, B., Li, Y. *Oxygen vacancy clusters promoting reducibility and activity of ceria nanorods.* Journal of the American Chemical Society, 2009, **131**(9): 3140-3141.

109. Sun, X., Nouri, M., Wang, Y., Li, D. Y. *Corrosive wear resistance of Mg-Al-Zn alloys with alloyed yttrium.* Wear, 2013, **302**(1-2): 1624-1632.

110. Jollet, F., Noguera, C., Gautier, M., Thromat, N., Duraud, J. -P *Influence of Oxygen Vacancies on the Electronic Structure of Yttrium Oxide.* Journal of the American Ceramic Society, 1991, **74**(2): 358-364.

111. Mitra, R.N., Merwin, M. J., Han, Z., Conley, S. M., Al-Ubaidi, M. R., Naash, M. I. *Yttrium oxide nanoparticles prevent photoreceptor death in a light-damage model of retinal degeneration.* Free Radical Biology and Medicine, 2014, **75**: 140-148.

112. Jollet, F., Maire, P., Gautier, M., Duraud, J. P., Gressus, C. L. *Influence of Stoichiometry on the Electrical and Mechanical Behavior of Yttrium Oxide Ceramics.* Journal of the American Ceramic Society, 1988, **71**(9): C-396-C-398.

113. Maria Magdalane, C., Kaviyarasu, K., Judith Vijaya, J., Siddhardha, B., Jeyaraj, B. *Facile synthesis of heterostructured cerium oxide/yttrium oxide nanocomposite in UV light induced photocatalytic degradation and catalytic reduction: Synergistic effect of antimicrobial studies.* Journal of Photochemistry and Photobiology B: Biology, 2017, **173**: 23-34.

114. Khajelakzay, M., Shoja Razavi, R., Barekat, M., Naderi, M., Milani, M. *Synthesis of yttria nanopowders by two precipitation methods and investigation of synthesis conditions.* International Journal of Applied Ceramic Technology, 2016, **13**(1): 209-218.

115. Ekambaram, S., Patil, K. C. *Combustion synthesis of yttria.* Journal of Materials Chemistry, 1995, **5**(6): 905-908.

116. Avdin, V.V., E.P. Yudina,I.V. Krivtsov *Preparation of layered yttrium oxide by hydrolysis of yttrium nitrate*, in *Materials Science Forum*. 2016. p. 10-15.

117. Li, N., Yanagisawa, K. *Controlling the morphology of yttrium oxide through different precursors synthesized by hydrothermal method.* Journal of Solid State Chemistry, 2008, **181**(8): 1738-1743.

118. Bunaciu, A.A., E.G. Udriştioiu,H.Y. Aboul-Enein *X-Ray Diffraction: Instrumentation and Applications.* Critical Reviews in Analytical Chemistry, 2015, **45**(4): 289-299.

119. Kot, M. *In-operando hard X-ray photoelectron spectroscopy study on the resistive switching physics of HfO_2-based RRAM*. 2014.

120. Braun, A., O. Couteau, K. Franks, V. Kestens, G. Roebben, A. Lamberty,T.P.J. Linsinger *Validation of dynamic light scattering and centrifugal liquid sedimentation methods for nanoparticle characterisation.* Advanced Powder Technology, 2011, **22**(6): 766-770.

121. Brunauer, S., P.H. Emmett,E. Teller *Adsorption of Gases in Multimolecular Layers.* Journal of the American Chemical Society, 1938, **60**(2): 309-319.
122. Sing, K. *The use of nitrogen adsorption for the characterisation of porous materials.* Colloids and Surfaces A: Physicochemical and Engineering Aspects, 2001, **187-188**: 3-9.
123. Thommes, M., Kaneko, K., Neimark Alexander, V., Olivier James, P., Rodriguez-Reinoso, F., Rouquerol, J., Sing Kenneth, S. W. *Physisorption of gases, with special reference to the evaluation of surface area and pore size distribution (IUPAC Technical Report)*, in *Pure and Applied Chemistry*. 2015. p. 1051.
124. Sielicki, P., Janik, H., Guzman, A., Namieśnik, J. *The progress in electron microscopy studies of particulate matters to be used as a standard monitoring method for air dust pollution.* Critical Reviews in Analytical Chemistry, 2011, **41**(4): 314-334.
125. Chauhan, A. *Deformation and damage mechanisms of ODS steels under high-temperature cyclic loading*. 2018.
126. Luo, Q. *Electron microscopy and spectroscopy in the analysis of friction and wear mechanisms.* Lubricants, 2018, **6**(3),58.
127. JEOL. *JEOL JEM-ARM200F Cs Corrected S/TEM*. [cited: 13/08/2019].
128. Vijayalakshmi, R., Rajendran, V. *Synthesis and characterization of nano-TiO_2 via different methods.* Archives of Applied Science Research, 2012, **4**(2): 1183-1190.
129. Abubakar, S., Kaya, S., Aktag, A., Yilmaz, E. *Yttrium oxide nanostructured thin films deposited by radio frequency sputtering: the annealing optimizations and correlations between structural, morphological, optical and electrical properties.* Journal of Materials Science: Materials in Electronics, 2017, **28**(18): 13920-13927.
130. López, R., Gómez, R. *Band-gap energy estimation from diffuse reflectance measurements on sol-gel and commercial TiO_2: A comparative study.* Journal of Sol-Gel Science and Technology, 2012, **61**(1): 1-7.
131. Shinde, D.R., Tambade, P. S., Chaskar, M. G., Gadave, K. M. *Photocatalytic degradation of dyes in water by analytical reagent grades ZnO, TiO_2 and SnO_2:*

A comparative study. Drinking Water Engineering and Science, 2017, **10**(2): 109-117.

132. Xue, Y., Luan, Q., Yang, D., Yao, X., Zhou, K. *Direct evidence for hydroxyl radical scavenging activity of cerium oxide nanoparticles.* Journal of Physical Chemistry C, 2011, **115**(11): 4433-4438.

133. Bogusz, K., Tehei, M., Lerch, M., Dou, S. X., Liu, H. K., Konstantinov, K. *$TiO_2/(BiO)_2CO_3$ nanocomposites for ultraviolet filtration with reduced photocatalytic activity.* Journal of Materials Chemistry C, 2018, **6**(21): 5639-5650.

134. Sanoop, P.K., Anas, S., Ananthakumar, S., Gunasekar, V., Saravanan, R., Ponnusami, V. *Synthesis of yttrium doped nanocrystalline ZnO and its photocatalytic activity in methylene blue degradation.* Arabian Journal of Chemistry, 2016, **9**: S1618-S1626.

135. Kim, S.H., Ngo, H. H., Shon, H. K., Vigneswaran, S. *Adsorption and photocatalysis kinetics of herbicide onto titanium oxide and powdered activated carbon.* Separation and Purification Technology, 2008, **58**(3): 335-342.

136. Boukamp, P.P., R. T.; Breitkreutz, D.; Hornung, J.; Markham, A. and Fusenig, N. E. *Normal keratinization in a spontaneously immortalized aneuploid human keratinocyte cell line.* Journal of Cell Biology, 1988, **106**(3): 761-771.

137. Bakand, S. *Development of in vitro methods for toxicity assessment of workplace air contaminants*, in *School of Safety Science*. 2006, UNSW.

138. Ong, K.J., MacCormack, T. J., Clark, R. J., Ede, J. D., Ortega, V. A., Felix, L. C., Dang, M. K. M., Ma, G., Fenniri, H., Veinot, J. G. C., Goss, G. G. *Widespread nanoparticle-assay interference: Implications for nanotoxicity testing.* PLoS ONE, 2014, **9**(3),e90650.

139. Rösslein, M., Elliott, J. T., Salit, M., Petersen, E. J., Hirsch, C., Krug, H. F., Wick, P. *Use of cause-and-effect analysis to design a high-quality nanocytotoxicology assay.* Chemical Research in Toxicology, 2015, **28**(1): 21-30.

140. Promega Corporation *CellTiter 96 AQueous One Solution Cell Proliferatin Assay*. 2012.

141. Stone, V., Johnston, H., Schins, R. P. F. *Development of in vitro systems for nanotoxicology: Methodological considerations in vitro methods for*

nanotoxicology Vicki Stone et al. Critical Reviews in Toxicology, 2009, **39**(7): 613-626.

142. Kent, C. *Basics of Toxicology*, ed. J.W. Sons. 1998. Editor^Editors
143. OSRAM. *More than just light: solutions in ultraviolet light*. 2006 [Accessed: 24/07/2019].
144. TEMIS. *Time series of UV data*. [Accessed: 10/08/2019]; Available from: http://www.temis.nl/uvradiation/UVarchive/stations_uv.html.
145. Yuangpho, N., Le, S. T. T., Treerujiraphapong, T., Khanitchaidecha, W., Nakaruk, A. *Enhanced photocatalytic performance of TiO_2 particles via effect of anatase-rutile ratio.* Physica E: Low-Dimensional Systems and Nanostructures, 2015, **67**: 18-22.
146. Melnikov, P., Nascimento, V. A., Consolo, L. Z. Z., Silva, A. F. *Mechanism of thermal decomposition of yttrium nitrate hexahydrate, $Y(NO_3)_3 \cdot 6H_2O$ and modeling of intermediate oxynitrates.* Journal of Thermal Analysis and Calorimetry, 2013, **111**(1): 115-119.
147. Wang, Y., Zhao, G. Y., Yuan, L. *Evolution of crystalline phase and morphology of the products formed during the hydrothermal synthesis of Y_2O_3 powders*, in *Advanced Materials Research*. 2011. p. 1275-1279.
148. Li, Z., Hou, B., Xu, Y., Wu, D., Sun, Y. *Hydrothermal synthesis, characterization, and photocatalytic performance of silica-modified titanium dioxide nanoparticles.* Journal of Colloid And Interface Science, 2005, **288**(1): 149-154.
149. Evonik Industries *AEROXIDE TiO2 P25*, in *Technical Informatin 1243*. 2015.
150. Xiong, S., Tang, Y., Ng, Huiyun S., Zhao, X., Jiang, Z., Chen, Z., Ng, K. W., Loo, S. C. J. *Specific surface area of titanium dioxide (TiO_2) particles influences cyto- and photo-toxicity.* Toxicology, 2013, **304**: 132-140.
151. Hartman, M., Trnka, O., Veselý, V. *Thermal dehydration of magnesium hydroxide and sintering of nascent magnesium oxide.* AIChE Journal, 1994, **40**(3): 536-542.
152. Irabien, A., Viguri, J. R., Cortabitarte, F., Ortiz, I. *Thermal Dehydration of Calcium Hydroxide. 2. Surface Area Evolution.* Industrial and Engineering Chemistry Research, 1990, **29**(8): 1606-1611.

153. Irabien, A., Viguri, J. R., Ortiz, I. *Thermal Dehydration of Calcium Hydroxide. 1. Kinetic Model and Parameters.* Industrial and Engineering Chemistry Research, 1990, **29**(8): 1599-1606.

154. Zou, M., Yang, F., Ma, J., Chen, Y., Cao, L., Liu, F. *The influences of nanoscale titanium dioxide particle size and crystal structure on light absorbance*. in *Nanotechnology 2010: Advanced Materials, CNTs, Particles, Films and Composites - Technical Proceedings of the 2010 NSTI Nanotechnology Conference and Expo, NSTI-Nanotech 2010*. 2010.

155. Yoon, H., Kim, D., Park, M., Kim, J., Kim, J., Srituravanich, W., Shin, B., Jung, Y., Jeon, S. *Extraordinary Enhancement of UV Absorption in TiO_2 Nanoparticles Enabled by Low-Oxidized Graphene Nanodots.* The Journal of Physical Chemistry C, 2018, **122**(22): 12114-12121.

156. Smijs, T.G., Pavel, S. *Titanium dioxide and zinc oxide nanoparticles in sunscreens: focus on their safety and effectiveness.* Nanotechnology, science and applications, 2011, **4**: 95-112.

157. Yu, Y., Chen, G., Zhou, Y., Han, Z. *Recent advances in rare-earth elements modification of inorganic semiconductor-based photocatalysts for efficient solar energy conversion: A review.* Journal of Rare Earths, 2015, **33**(5): 453-462.

158. Petoukhoff, C.E., O'Carroll, D. M. *Absorption-induced scattering and surface plasmon out-coupling from absorber-coated plasmonic metasurfaces.* Nature Communications, 2015, **6**(1): 7899-7911.

159. Xu, A.W., Gao, Y., Liu, H. Q. *The preparation, characterization, and their photocatalytic activities of rare-earth-doped TiO_2 nanoparticles.* Journal of Catalysis, 2002, **207**(2): 151-157.

160. Zhang, H., Tan, K., Zheng, H., Gu, Y., Zhang, W. F. *Preparation, characterization and photocatalytic activity of TiO_2 codoped with yttrium and nitrogen.* Materials Chemistry and Physics, 2011, **125**(1-2): 156-160.

161. Yang, J., Pan, L., Xue, X., Wang, M., Qiu, T. *Effect of Tb_2O_3 additive on structure of anatase and photocatalytic activity of TiO2/(O' +β')-Sialon multi-phase ceramics.* Journal of Rare Earths, 2009, **27**(2): 204-210.

162. Lin, L.-Y., Yeh, M-H., Chen, C-Y., Vittal, R., Wu, C-G., Ho, K-C. *Surface modification of TiO_2 nanotube arrays with Y_2O_3 barrier layer: controlling*

charge recombination dynamics in dye-sensitized solar cells. Journal of Materials Chemistry A, 2014, **2**(22): 8281-8287.

163. Liang, C.H., Li, F. B., Liu, C. S., Lü, J. L., Wang, X. G. *The enhancement of adsorption and photocatalytic activity of rare earth ions doped TiO_2 for the degradation of Orange I.* Dyes and Pigments, 2008, **76**(2): 477-484.

164. Jones, C.F., Grainger, D. W. *In vitro assessments of nanomaterial toxicity.* Advanced Drug Delivery Reviews, 2009, **61**(6): 438-456.

165. Genç, H., Barutca, B., Koparal, A. T., Özöğüt, U., Şahin, Y., Suvacı, E. *Biocompatibility of designed MicNo-ZnO particles: Cytotoxicity, genotoxicity and phototoxicity in human skin keratinocyte cells.* Toxicology in Vitro, 2018, **47**: 238-248.

166. Faria, M., Navas, J. M., Soares, A. M. V. M., Barata, C. *Oxidative stress effects of titanium dioxide nanoparticle aggregates in zebrafish embryos.* Science of the Total Environment, 2014, **470-471**: 379-389.

167. Hanot-Roy, M., Tubeuf, E., Guilbert, A., Bado-Nilles, A., Vigneron, P., Trouiller, B., Braun, A., Lacroix, G. *Oxidative stress pathways involved in cytotoxicity and genotoxicity of titanium dioxide (TiO_2) nanoparticles on cells constitutive of alveolo-capillary barrier in vitro.* Toxicology in Vitro, 2016, **33**: 125-135.

168. Kocbek, P., Teskač, K., Kreft Mateja, E., Kristl, J. *Toxicological Aspects of Long-Term Treatment of Keratinocytes with ZnO and TiO_2 Nanoparticles.* Small, 2010, **6**(17): 1908-1917.

169. Lopes, V.R., Loitto, V., Audinot, J. N., Bayat, N., Gutleb, A. C., Cristobal, S. *Dose-dependent autophagic effect of titanium dioxide nanoparticles in human HaCaT cells at non-cytotoxic levels.* Journal of Nanobiotechnology, 2016, **14**(1): 22-34,22.

170. Rizk, M.Z., Ali, S. A., Hamed, M. A., El-Rigal, N. S., Aly, H. F., Salah, H. H. *Toxicity of titanium dioxide nanoparticles: Effect of dose and time on biochemical disturbance, oxidative stress and gentoxicity in mice.* Biomedicine and Pharmacotherapy, 2017, **90**: 466-472.

171. Su, J.K., Byeong, M. K., Young, J. L., Hai, W. C. *Titanium dioxide nanoparticles trigger p53-mediated damage response in peripheral blood lymphocytes.* Environmental and Molecular Mutagenesis, 2008, **49**(5): 399-405.

172. Stern, S.T., Adiseshaiah, P. P., Crist, R. M. *Autophagy and lysosomal dysfunction as emerging mechanisms of nanomaterial toxicity.* Particle and Fibre Toxicology, 2012, **9**: 20,20.

173. Burello, E., Worth, A. P. *A theoretical framework for predicting the oxidative stress potential of oxide nanoparticles.* Nanotoxicology, 2011, **5**(2): 228-235.

174. Yu, K.N., Chang, S. H., Park, S. J., Lim, J., Lee, J., Yoon, T. J., Kim, J. S., Cho, M. H. *Titanium dioxide nanoparticles induce endoplasmic reticulum stress-mediated autophagic cell death via mitochondria-associated endoplasmic reticulum membrane disruption in normal lung cells.* PLoS ONE, 2015, **10**(6),e0131208.

175. Luo, R., Liao, Z., Song, Y., Yin, H., Zhan, S., Li, G., Ma, L., Lu, S., Wang, K., Li, S., Zhang, Y., Yang, C. *Berberine ameliorates oxidative stress-induced apoptosis by modulating ER stress and autophagy in human nucleus pulposus cells.* Life Sciences, 2019, **228**: 85-97.

176. Cai, Y., Arikkath, J., Yang, L., Guo, M. L., Periyasamy, P., Buch, S. *Interplay of endoplasmic reticulum stress and autophagy in neurodegenerative disorders.* Autophagy, 2016, **12**(2): 225-244.

177. Nakashima, A., Cheng, S.-B., Kusabiraki, T., Motomura, K., Aoki, A., Ushijima, A., Ono, Y., Tsuda, S., Shima, T., Yoshino, O., Sago, H., Matsumoto, K., Sharma, S., Saito, S. *Endoplasmic reticulum stress disrupts lysosomal homeostasis and induces blockade of autophagic flux in human trophoblasts.* Scientific Reports, 2019, **9**(1): 11466.

178. Zeeshan, H.M.A., Lee, G. H., Kim, H-R., Chae, H-J. *Endoplasmic Reticulum Stress and Associated ROS.* International Journal of Molecular Sciences, 2016, **17**(3): 327-327.

179. Zhao, Y., Howe, J. L. C., Yu, Z., Leong, D. T., Chu, J. J. H., Loo, J. S. C., Ng, K. W. *Exposure to titanium dioxide nanoparticles induces autophagy in primary human keratinocytes.* Small, 2013, **9**(3): 387-392.

180. Halamoda Kenzaoui, B., Chapuis Bernasconi, C., Guney-Ayra, S., Juillerat-Jeanneret, L. *Induction of oxidative stress, lysosome activation and autophagy by nanoparticles in human brain-derived endothelial cells.* Biochemical Journal, 2012, **441**(3): 813-821.

181. Ghaznavi, H., Najafi, R., Mehrzadi, S., Hosseini, A., Tekyemaroof, N., Shakeri-Zadeh, A., Rezayat, M., Sharifi, A. M. *Neuro-protective effects of cerium and yttrium oxide nanoparticles on high glucose-induced oxidative stress and apoptosis in undifferentiated PC12 cells.* Neurological Research, 2015, **37**(7): 624-632.

182. Sha, B., Gao, W., Han, Y., Wu, J., Xu, F., Lu, T. J. *Potential Application of Titanium Dioxide Nanoparticles in the Prevention of Osteosarcoma and Chondrosarcoma Recurrence.* Journal of Nanoscience and Nanotechnology, 2013, **13**(2): 1208-1211.

183. Farrukh, M.R., Nissar, U. A., Afnan, Q., Rafiq, R. A., Sharma, L., Amin, S., Kaiser, P., Sharma, P. R., Tasduq, S. A. *Oxidative stress mediated Ca^{2+} release manifests endoplasmic reticulum stress leading to unfolded protein response in UV-B irradiated human skin cells.* Journal of Dermatological Science, 2014, **75**(1): 24-35.

184. Mera, K., Kawahara, K. I., Tada, K. I., Kawai, K., Hashiguchi, T., Maruyama, I., Kanekura, T. *ER signaling is activated to protect human HaCaT keratinocytes from ER stress induced by environmental doses of UVB.* Biochemical and Biophysical Research Communications, 2010, **397**(2): 350-354.

185. Gao, M.Q., Guo, S. B., Chen, X. H., Du, W., Wang, C. B. *Molecular mechanisms of polypeptide from Chlamys farreri protecting HaCaT cells from apoptosis induced by UVA plus UVB.* Acta Pharmacologica Sinica, 2007, **28**(7): 1007-1014.

186. Henri, P., Beaumel, S., Guezennec, A., Poumès, C., Stoebner, P. E., Stasia, M. J., Guesnet, J., Martinez, J., Meunier, L. *MC1R expression in HaCaT keratinocytes inhibits UVA-induced ROS production via NADPH Oxidase- and cAMP-dependent mechanisms.* Journal of Cellular Physiology, 2012, **227**(6): 2578-2585.

187. Lawrence, K.P., Douki, T., Sarkany, R. P. E., Acker, S., Herzog, B., Young, A. R. *The UV/Visible Radiation Boundary Region (385–405 nm) Damages Skin Cells and Induces "dark" Cyclobutane Pyrimidine Dimers in Human Skin in vivo.* Scientific Reports, 2018, **8**(1): 12722-12733,12722.

188. Park, Y.K., Jang, B. C. *UVB-induced anti-survival and pro-apoptotic effects on HaCaT human keratinocytes via caspase- and PKC-dependent downregulation*

of PKB, HIAP-1, Mcl-1, XIAP and ER stress. International Journal of Molecular Medicine, 2014, **33**(3): 695-702.

189. Narayanapillai, S., Agarwal, C., Tilley, C., Agarwal, R. *Silibinin is a potent sensitizer of UVA radiation-induced oxidative stress and apoptosis in human keratinocyte HaCaT cells.* Photochemistry and Photobiology, 2012, **88**(5): 1135-1140.

190. Shin, D., Moon, H. W., Oh, Y., Kim, K., Kim, D. D., Lim, C. J. *Defensive properties of ginsenoside re against UV-B-induced oxidative stress through Up-regulating glutathione and superoxide dismutase in HaCaT keratinocytes.* Iranian Journal of Pharmaceutical Research, 2018, **17**(1): 249-260.

191. Palanki, R., Arora, S., Tyagi, N., Rusu, L., Singh, A. P., Palanki, S., Carter, J. E., Singh, S. *Size is an essential parameter in governing the UVB-protective efficacy of silver nanoparticles in human keratinocytes.* BMC Cancer, 2015, **15**(1): 636-642,636.

192. Park, H.O., Yu, M., Kang, S. K., Yang, S. I., Kim, Y. J. *Comparison of cellular effects of titanium dioxide nanoparticles with different photocatalytic potential in human keratinocyte, HaCaT cells.* Molecular and Cellular Toxicology, 2011, **7**(1): 67-75.

193. Jaeger, A., Weiss, D. G., Jonas, L., Kriehuber, R. *Oxidative stress-induced cytotoxic and genotoxic effects of nano-sized titanium dioxide particles in human HaCaT keratinocytes.* Toxicology, 2012, **296**(1-3): 27-36.

194. Fu, P.P., Xia, Q., Hwang, H-M., Ray, P. C., Yu, H. *Mechanisms of nanotoxicity: Generation of reactive oxygen species.* Journal of Food and Drug Analysis, 2014, **22**(1): 64-75.

195. Xie, J., Zhong, F., Han, Y., Gao, H., Wang, C., Peng, J. *Polypeptide from Chlamys farreri restores endoplasmic reticulum (ER) redox homeostasis, suppresses ER stress, and inhibits ER stress-induced apoptosis in ultraviolet B-irradiated HaCaT cells.* American Journal of Translational Research, 2015, **7**(5): 959-966.

196. Egerton, T.A. *Uv-absorption-the primary process in photocatalysis and some practical consequences.* Molecules, 2014, **19**(11): 18192-18214.

197. Sharaf, O.Z., Kyritsis, D. C., Abu-Nada, E. *Impact of nanofluids, radiation spectrum, and hydrodynamics on the performance of direct absorption solar collectors.* Energy Conversion and Management, 2018, **156**: 706-722.